Compact Stacked Metamaterial for Robust and Efficient Dual-band Wireless Power Transfer System

姜, 欣

https://hdl.handle.net/2324/7182558

出版情報：九州大学, 2023, 博士（工学）, 課程博士
バージョン：
権利関係：

Graduate School of Information Science and Electrical Engineering

Compact Stacked Metamaterial for Robust and Efficient Dual-band Wireless Power Transfer System

By

JIANG XIN

A Doctoral thesis

Submitted to the Graduate School of Information Science and Electrical Engineering in partial fulfillment of the requirements for the degree of Doctor of Philosophy

Department of Electrical and Electronics Engineering

Graduate School of Information Science and Electrical Engineering

Kyushu University, Fukuoka, Japan

2024

ABSTRACT

The rapid proliferation of portable devices has led to a paradigm shift from wired to wireless charging methods. Wireless power transfer (WPT) systems are expected to be compact and embedded within devices, providing not only power but also additional functionalities such as data exchange. Dual-band WPT systems have emerged as a preferred choice to address these requirements effectively. Recent research has focused on leveraging metamaterials to enhance power transfer efficiency (PTE) in near-field WPT systems.

This work addresses the challenges associated with metamaterials in dual-band WPT systems. Chapter 2 - 3 provides an overview of the background and challenges, highlighting the limitations of WPT and previous metamaterials. By exploiting near-zero permeability, metamaterials act as perfect lenses to focus electromagnetic waves in desired directions. However, conventional one-dimensional (1D) metamaterials only enhance the PTE of one band, necessitating the development of metamaterials that simultaneously improve the efficiency of both bands.

Motivated by this, Chapter 4 proposes a multi-mode stacked metamaterial composed of two stacked metamaterials effective for each band. The horizontally aligned metamaterials exhibit two self-resonant frequencies, aligning with the WPT working frequency. However, misalignment between the transmitter (Tx) and receiver (Rx) leads to inferior performance.

To address this, Chapter 5 introduces a hybrid split ring resonator (SRR)-based metamaterial with alternately stacked unit cells. This design allows for three near-zero permeability points within desired frequencies, significantly improving efficiency and lateral misalignment tolerance compared to previous approaches.

Chapter 6 presents a nonreciprocal metamaterial acting as an absorber in a dual-band simultaneous information and power transfer (SWIPT) system. A 10-mm-thick human body equivalent phantom is used for the SWIPT system's evaluation. Experimental results indicate that embedding this absorber between power and signal ports in both Tx and Rx of a SWIPT system results in a 3 dB improvement in isolation performance. Concurrently, with the assistance of the proposed absorber, the datarate improves by 3.6 Mb/s, allowing signals to be transmitted with 5 dBm weaker power than the original system.

In Chapter 7, a novel AI-based method is proposed to automatically optimize the DGS-based wireless power transfer (WPT) system within the desired working frequency. The method leverages a dual annealing algorithm to achieve fast system optimization.

Chapter 8-9 makes conclusion and plan of the future work.

ACKNOWLEDGEMENTS

I would like to express my heartfelt gratitude to my supervisor, Prof. Dr. Ramesh Kumar Pokharel, for providing me with the invaluable opportunity to work on this fascinating project on wireless power transfer systems and metamaterials. His guidance, expertise, and continuous support have been instrumental in shaping this research endeavor.

I am also deeply indebted to Prof. Dr. Kuniaki Yoshitomi for his generous assistance throughout the fabrication process. His expertise and insights have greatly contributed to the success of this project. I would also like to extend my gratitude to Dr. Adel Barakat for his valuable suggestions and assistance in the design phase.

I would like to acknowledge the unwavering support and assistance provided by Eng. Maoqiang Sun and Eng. Dong during the design and fabrication processes. His dedication and expertise have been invaluable in the realization of this project. Additionally, I would like to express my sincere appreciation to all the members of my laboratory for their collaboration and valuable input.

Furthermore, I would like to express my deep appreciation to my parents for their unwavering support and encouragement throughout this journey. Their love and belief in me have been a constant source of motivation and strength.

Lastly, I would like to thank all the individuals who have contributed in any way to this project, directly or indirectly. Your support has played a significant role in the successful completion of this research.

Thank you all for being a part of this incredible journey.

Contents

Figures

Tables

1 Introduction

1.1 Background

With the increasing popularity of portable devices such as smartphones, smartwatches, and healthcare monitoring devices [1]–[5], and so on, the demand for wireless charging technology has been growing in both industrial and academic research. Wireless power transfer (WPT) modules for portable devices need to be efficient to minimize charging time and compact enough to be embedded into the devices.

Moreover, WPT should offer more functionality to meet the diverse requirements of different devices. For instance, it should enable information exchange between the battery (e.g., battery status) and the devices themselves (e.g., health data). In single-band systems, power and data are commonly transferred alternately using backscattering technology [6], [7]. However, this interrupts the power transfer process, potentially degrading power transfer efficiency (PTE). Therefore, a more suitable choice for such applications is a multi-band system, specifically a dual-band system.

Nevertheless, research on multi-band WPT is still limited due to challenges such as size constraints and mutual interference. Most research in this area relies on the use of coils [6], which makes the overall system too bulky to be incorporated into devices. As an alternative, the defected ground structure (DGS) has been proposed and applied. DGS-based WPT systems have shown promising performance in terms of power transfer efficiency [8], [9], misalignment tolerance [10], and multi-band characteristics [11]–[13].

In addition, metamaterials (metasurfaces) have been employed to enhance WPT performance. These metamaterials act as electromagnetic lenses with adjustable dielectric characteristics (e.g., permeability). By optimizing the metamaterials, the wave can be focused on the desired destination, such as the receiver (RX), thereby increasing PTE.

However, the recently proposed near-field-oriented metamaterials are only effective for the single-band system [14]–[17]. When these metamaterials are used in a dual-band system, they only enhance the PTE of one band. In contrast, the improvement in the other band is not as significant. Hence, there is a need to develop a metamaterial that can effectively enhance power transfer in both bands for dual-band wireless power transfer [17].

1.2 Purpose of Research

In a recent study, researchers have proposed multi-band wireless power transfer (WPT) systems [11]–[13], [18]. These systems enable simultaneous power transfer on both bands or concurrent transmission of patient monitoring data and power. In order to enhance the performance of these systems, there is a need for an effective multi-band metamaterial. Additionally, a stacked metamaterial has been recently introduced [19], which demonstrates greater geometric possibilities in combining unit cells of metamaterials.

Based on these considerations, we propose a set of metamaterials to address three key aspects of improvement:

- **Wireless Power Transfer Efficiency**: The primary goal of a WPT system is to transfer power efficiently from the transmitter (Tx) to the receiver (Rx), thereby reducing charging time.

- **Tolerance of the Lateral Misalignment**: To ensure a robust WPT system, it is important to maintain consistent power transfer efficiency even when the Tx or the Rx is misaligned from the expected directions.

- **Mutual interference between Two Bands:** Assuming that power is input into the first band and signals are input into the second band, it is essential to minimize interference from the first band in order to ensure high-quality signal transmission.

By addressing these three aspects, our proposed metamaterials aim to enhance wireless power transfer efficiency, improve tolerance to lateral misalignment, and minimize mutual interference between the two bands for superior signal quality.

1.3 Structure of the Thesis

This work focuses on enhancing the performance of dual-band wireless power transfer (WPT) through the use of metamaterials. It is organized into several chapters, each addressing different aspects of the research.

In Chapters 2, 3, the authors provide a survey of conventional wireless power transfer systems, covering both near-field and far-field approaches. They discuss the limitations of these conventional systems, which sets the stage for proposing alternative solutions.

Chapter 4 provides an in-depth exploration of the principles and applications of simultaneous wireless information and power transfer (SWIPT) systems. It delves into the advancements and challenges in this field, highlighting the benefits of SWIPT such as improved energy harvesting capabilities, enhanced utilization, and its potential for powering various devices in the Internet of Things (IoT) and wearable technology domains. The chapter also discusses the use of frequency-shift keying (FSK) modulation in SWIPT systems and the associated challenges, including capacitor optimization, safety concerns in biomedical applications, and reduced power transfer efficiency. By addressing these challenges through innovative design strategies and alternative data transmission methods, the chapter emphasizes the potential for developing compact, efficient, and safe wireless charging systems for portable and wearable electronic devices.

Chapter 5 offers an overview of the background and challenges related to employing metamaterials for dual-band WPT. The authors analyze the dielectric characteristics of metamaterials and summarize the limitations and issues associated with previously proposed metamaterials.

To overcome these challenges, Chapter 6 introduces a multi-mode stacked metamaterial composed of two stacked metamaterials, each designed to be effective for one band of the dual-band WPT system. While this experiment significantly improves wireless power transfer efficiency, it fails to achieve the desired improvement in lateral misalignment due to the topology.

In response to this limitation, Chapter 7 presents a novel hybrid split ring resonator (SRR)-based metamaterial. This new metamaterial exhibits two near-zero permeability points that can be optimized within the desired frequency range, effectively addressing the misalignment issue discussed in the previous chapter.

Chapter 8 introduces a nonreciprocal metamaterial for a dual-band simultaneous information and power transfer (SWIPT) system. This metamaterial functions as an absorber, reducing interference between the signal and power bands when a signal is input into the signal port.

Finally, Chapter 9 summarizes the proposed metamaterials and identifies the challenges that need to be addressed in future work. The authors plan to utilize machine learning techniques to optimize the metamaterial and the dimensions of the WPT system based on defected ground structures (DGS). Meanwhile, self-resonant theory can be utilized to fix the Overcoupling problem when the Tx and Rx gets too close.

Overall, this work explores different types of metamaterials to enhance dual-band wireless power transfer in terms of power transfer efficiency, lateral misalignment tolerance, and mutual interference reduction. It provides insights into the design and optimization of metamaterials for improved WPT systems and suggests future research directions.

2 Conventional WPT System

The Wireless Power Transfer (WPT) system enables the transfer of power wirelessly from a transmitter to a receiver. The method of coupling employed in the system determines the transmission distance achievable. As a result, the WPT system can be categorized into two main types: near-field (nonradiative) WPT and far-field (radiative) WPT, based on the nature of the coupling mechanism.

In near-field WPT, the power transfer occurs through close proximity between the transmitter and receiver. This proximity allows for strong magnetic or electric coupling, enabling efficient power transfer over short distances. Near-field WPT is commonly utilized in applications such as wireless charging pads or mats, where the device being charged needs to be placed in close proximity to the charging base.

On the other hand, far-field WPT involves the transmission of power over longer distances using electromagnetic radiation. This type of WPT relies on the principles of electromagnetic waves, where the power is transmitted as a radiative field that propagates through space. Far-field WPT is commonly employed in applications such as wireless power transmission for electric vehicles or large-scale power transfer systems.

Both near-field and far-field WPT have their advantages and limitations. Near-field WPT offers efficient power transfer over short distances but requires close alignment and proximity between the transmitter and receiver. Far-field WPT, while enabling power transfer over longer distances, requires careful consideration of power loss and alignment issues.

Understanding the different categories of coupling in the WPT system allows for the selection of the appropriate approach based on the specific requirements of the application at hand. By choosing the suitable coupling method, efficient and reliable wireless power transfer can be achieved in various scenarios, contributing to the advancement of wireless charging and power transmission technologies.

2.1 Near Field (Nonradiative) WPT System

Indeed, the near-field WPT system is primarily employed for short-distance power transmission due to its limitations on coupling. Within the near-field category, the coupling mechanism can further be classified into two main types: inductive coupling and capacitive coupling.

2.1.1 Inductive Coupling

Inductive coupling is one of the most commonly used methods in near-field WPT systems, as shown in Fig. 1. It relies on the principle of magnetic fields to transfer power between the transmitter and receiver. The transmitter coil generates a magnetic field, which induces a voltage in the receiver coil when they are in close proximity. This induced voltage can then be used to power the receiving device or charge its battery. Inductive coupling is widely applied in applications such as wireless charging pads for smartphones, where the charging pad and the device need to be placed in direct contact or very close proximity.

The K factor is a parameter used to characterize the coupling between two coils in a wireless power transfer (WPT) system. It quantifies the degree of magnetic coupling between the transmitting and receiving coils, indicating how effectively power is transferred from the transmitter to the receiver.

The K factor is calculated as the ratio of the mutual inductance (M) between the two coils to the geometric mean of their self-inductances ($L_{1,2}$):

$$K = \frac{M}{\sqrt{L_1 L_2}} \tag{2.1}$$

A K factor of 1 represents ideal coupling, where all the magnetic flux generated by the transmitter coil is captured by the receiver coil, resulting in efficient power transfer. On the other hand, a K factor close to 0 indicates weak coupling and low power transfer efficiency.

In addition to the K factor, the Q factor is another important parameter used to assess the performance of a WPT system. The Q factor represents the quality factor of a resonant circuit, which is determined by the energy losses in the system. It reflects the balance between the stored energy and the dissipated energy.

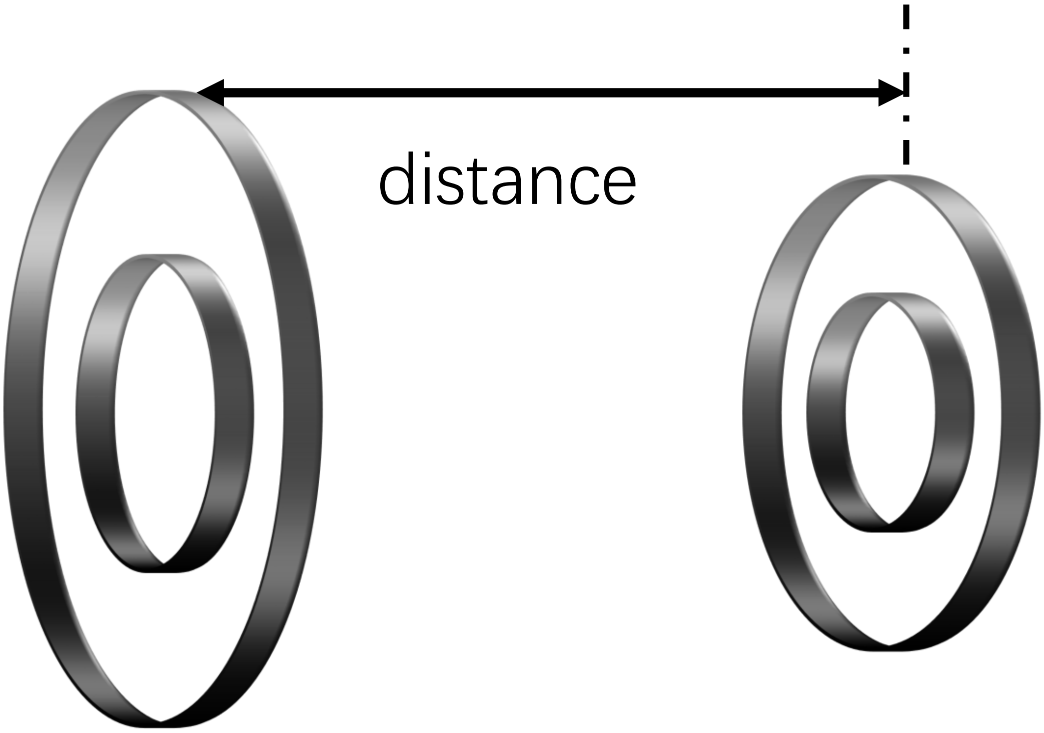

(a)

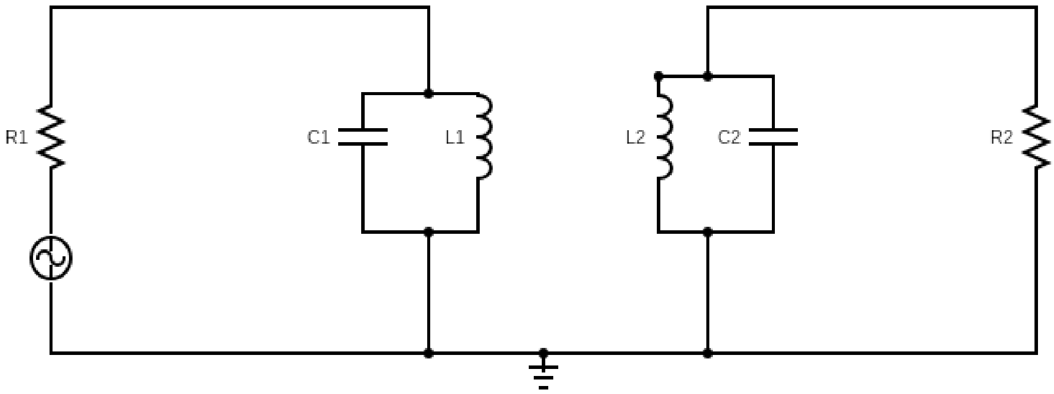

(b)

Fig. 1 (a)Conventional inductive system using coils. (b)A simple equivalent circuit of the inductive coupling.

A higher Q factor indicates lower energy losses and higher efficiency in the WPT system. It is calculated as the ratio of the energy stored in the resonant circuit to the energy dissipated per cycle:

$$Q = \frac{2\pi f L}{R} \tag{2.2}$$

where f is the operating frequency, L is the self-inductance of the coil, and R is the equivalent resistance of the system.

Both the K factor and Q factor are crucial in evaluating the performance of a WPT system. The K factor determines the level of coupling between the transmitter and receiver, while the Q factor indicates the efficiency and energy losses in the system. By optimizing these factors, the overall performance and efficiency of the WPT system can be improved:

$$\eta_{max} = \left[\frac{KQ}{1 + \sqrt{1 + (KQ)^2}}\right]^2 \tag{2.3}$$

The trade-off between the K factor and the Q factor arises because increasing the coupling to improve the K factor often leads to increased energy losses and lower Q factor, and vice versa. This trade-off poses a challenge in optimizing the efficiency of a WPT system.

2.1.2 Capacitive Coupling

Both inductive coupling and capacitive coupling have their advantages and limitations. Inductive coupling offers high efficiency and is suitable for applications where physical alignment between the transmitter and receiver is feasible. On the other hand, capacitive coupling allows for more flexibility in terms of spatial positioning, but it typically has lower efficiency compared to inductive coupling.

Capacitive coupling is a fundamental concept in electrical engineering and has various applications in different fields. It involves the transfer of electrical energy between two conductive objects or circuits through an electric field established between them as shown in Fig. 2.

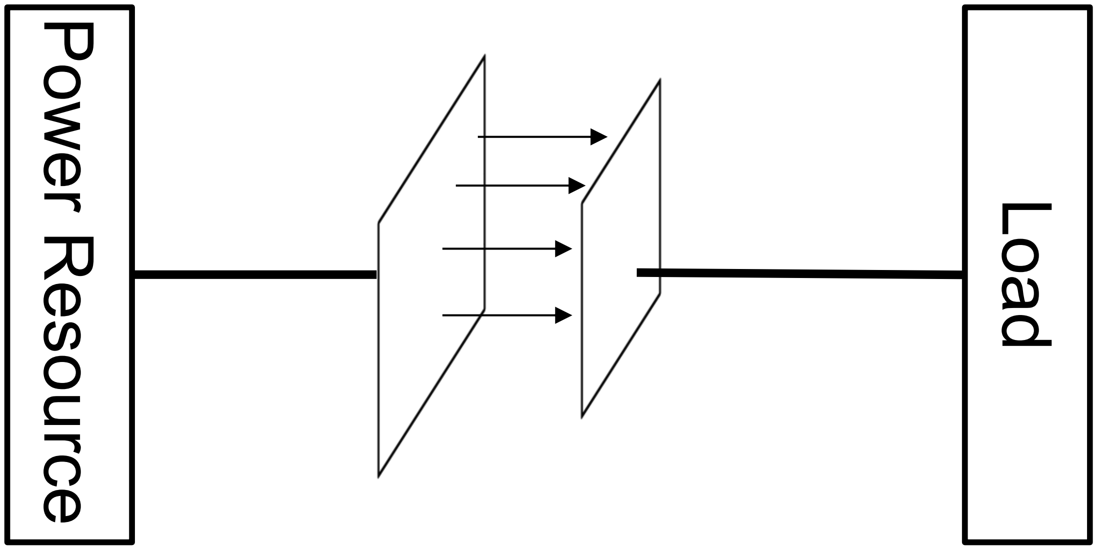

Fig. 2 A simple capacitive coupling.

2.2 DGS

The introduction of defected ground structures (DGS) is indeed a promising approach to overcome the KQ trade-off limitation in wireless power transfer (WPT) systems. DGS technology offers more flexibility in adjusting the layout of the system by enabling independent control of the K factor and the Q factor.

A conventional defected ground structure, as shown in Fig. 3, introduces specific patterns or features in the ground plane of the WPT system. These patterns are strategically designed to manipulate the electromagnetic field distribution and alter the characteristics of the system.

By utilizing a defected ground structure, the K and Q factors can be adapted independently, breaking the traditional trade-off relationship between them. This means that it is possible to achieve high coupling (high K factor) while maintaining low energy losses (high Q factor), or vice versa.

The ability to independently control the K and Q factors offers greater flexibility in optimizing the performance of the WPT system. Designers can adjust the layout of the system, including the geometry and placement of the coils, to achieve the desired coupling and energy transfer efficiency without sacrificing one for the other.

By incorporating DGS technology into WPT systems, researchers and engineers can explore new possibilities in enhancing the power transfer efficiency and overcoming the limitations imposed by the KQ trade-off. The independent control of the K and Q factors opens up avenues for innovative designs and improved performance in wireless power transfer applications.

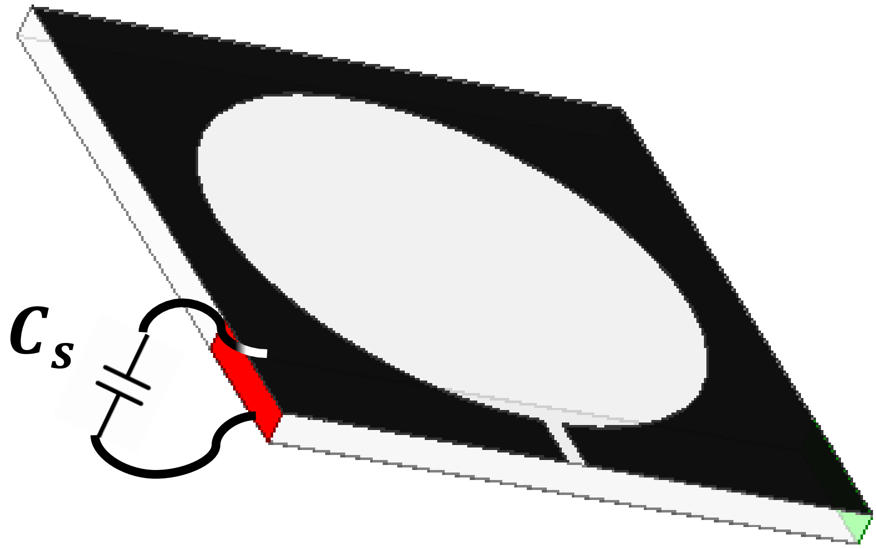

Fig. 3 A simple defected ground structure.

2.3 An Example of a DGS-based WPT System

To illustrate the technique of using defected ground structures (DGS) in wireless power transfer (WPT) systems, let's consider an example of a DGS-based single-band WPT system and explore how to optimize its power transfer performance.

To optimize the power transfer performance, several design parameters can be considered. Firstly, the geometry and dimensions of the DGS patterns play a crucial role. By adjusting the size, shape, and spacing of the patterns, the coupling and energy transfer efficiency can be modified. This allows for customization according to the specific requirements of the WPT system.

Therefore, Fig. 4 indicates a simple proposed DGS-based WPT system. The DGS is printed on the bottom of the Tx (top of the Rx), and the microstrip stub is printed on the top of the Tx (bottom of the Rx). Based on the layout, an equivalent circuit is derived in Fig. 5, where L_p is the inductance derived from the printed copper of DGS shown in

Fig. (b). As a result, the resonance frequency of the proposed WPT system is:

$$\omega_{critical} = \frac{1}{\sqrt{L'_p C'_p}} \tag{2.4}$$

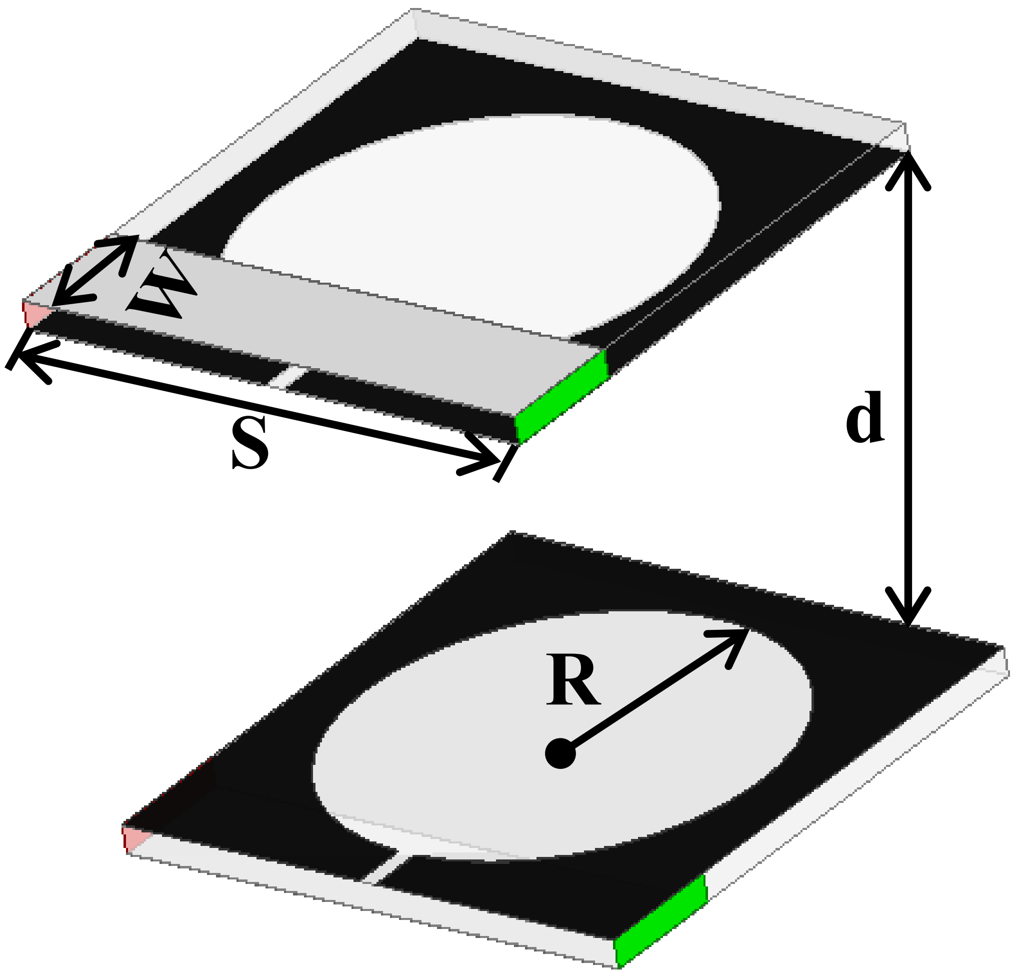

Fig. 4 Proposed DGS-based symmetric single band WPT system.

J-inverter is conventionally utilized to optimize the PTE performance based on the circuits [10], [20], as shown in Fig. 6.

For a symmetric WPT system, the impedance of the load equals the load of the signal source (R_s). Thus, according to the Kuroda identities, the input admittance can be figured out [10], [20]:

$$Y_3 = \frac{J_1^2}{Y_2} = \frac{J_1^2}{\frac{J_2^2}{Y_1}} = \frac{J_1^2}{\frac{J_2^2}{\frac{J_3^2}{\frac{1}{R_s}}}} = \frac{J_1^2 J_2^2 R_s}{J_m^2} \tag{2.5}$$

So that for the perfect match, the input admittance is supposed to equal the load admittance (R_S^{-1}):

$$J_1 J_3 R_s = J_2 \tag{2.6}$$

Based on (3.3), each value of the lumped capacitors and inductors can be determined by mapping the ABCD matrix of the J-inverters [10], [20].

Then the inductance of the DGS and the mutual inductance (**M**) between the Tx and the Rx can be estimated from the impedance (Z-) matrix, respectively, by using a high-frequency structure simulator (HFSS):

$$L_p = \frac{Im(Z_{Tx\,(Rx),Tx\,(Rx)})}{\omega} \tag{2.7}$$

$$M = \frac{Im(Z_{Tx,Rx})}{\omega} \tag{2.8}$$

Because of the parasite inductance and capacitance, the physical dimensions of Tx (Rx) should be further optimized using a high-frequency structure simulator (HFSS).

To optimized the performance of DGS, Fig. 7 shows the equivalent circuit of each J-inverter [20].

2.3.1 Optimization Steps

In this subsection, we present the fundamental steps involved in the optimization of the defected ground structure (DGS). These steps provide a systematic approach to achieving the desired performance and characteristics of the DGS-based system.

By cascading the whole equivalent components on the self-inductances $L_1 L_2$ and mutual-inductance L_m in the Fig.(equivalent circuit), the transmission matrix can be calculated as **Error! Reference source not found.**. Also, the transmission matrix can also be calculated as [20]:

$$T_m = \begin{bmatrix} \dfrac{L_1}{L_m} & j\omega_0 \dfrac{L_1 L_2 - L_m^2}{L_m} \\ \dfrac{1}{j\omega_0 L_m} & \dfrac{L_2}{L_m} \end{bmatrix} \tag{2.9}$$

$$\begin{aligned} T_m &= \begin{bmatrix} 1 & 0 \\ \dfrac{1}{j\omega_0 L_1^{'}} & 1 \end{bmatrix} \begin{bmatrix} 0 & -\dfrac{1}{jJ_2} \\ jJ_2 & 0 \end{bmatrix} \begin{bmatrix} 1 & 0 \\ \dfrac{1}{j\omega_0 L_2^{'}} & 1 \end{bmatrix} \\ &= \begin{bmatrix} \dfrac{1}{\omega_0 L_2^{'} J_2} & -\dfrac{1}{jJ_2} \\ jJ_m + \dfrac{1}{j\omega_0^2 L_1^{'} L_2^{'} J_2} & \dfrac{1}{\omega_0 L_1^{'} J_2} \end{bmatrix} \end{aligned} \tag{2.10}$$

Thus, the comparison of the **Error! Reference source not found.** and **Error! Reference source not found.** makes it possible to figure out the L_1, L_2, L_m as:

$$\begin{aligned} L_1 &= \frac{L_1^{'}}{1 - \omega_0^2 L_1^{'} L_2^{'} J_2^2} \\ L_2 &= \frac{L_2^{'}}{1 - \omega_0^2 L_1^{'} L_2^{'} J_2^2} \\ L_m &= \frac{\omega_0 L_1^{'} L_2^{'} J_2}{1 - \omega_0^2 L_1^{'} L_2^{'} J_2^2} \end{aligned} \tag{2.11}$$

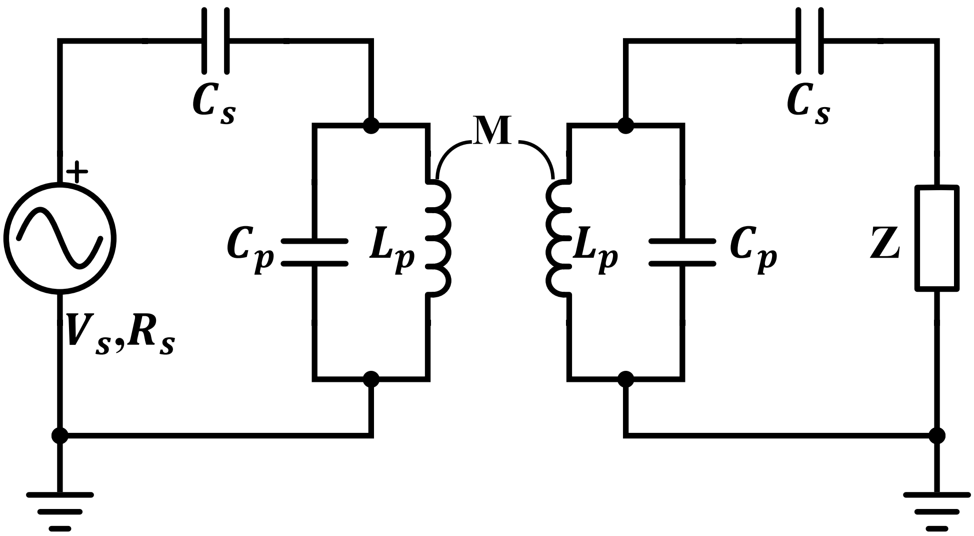

Fig. 5 Equivalent circuits of the proposed WPT. L_p is the inductance derived from the printed copper.

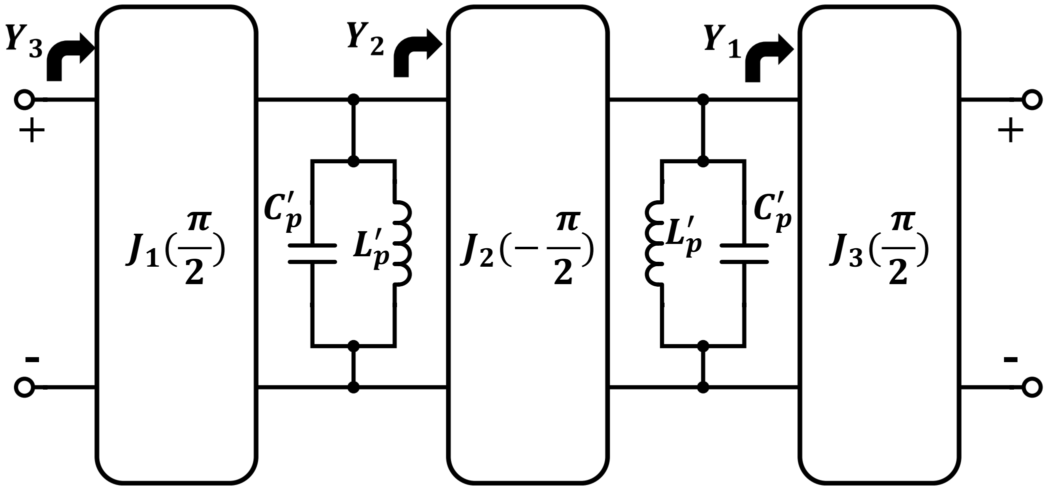

Fig. 6 Equivalent circuits using J-inverter for impedance matching.

Also, the J_2 can be figured out by **Error! Reference source not found.**

$$J_2 = \frac{1}{\omega_0\left(\frac{L_1L_2 - L_m^2}{L_m}\right)} \tag{2.12}$$

Also, the equivalent admittances Y_{s1} , and Y_{s2} are also computed by **Error! Reference source not found.**

$$\begin{aligned} Y_{s2} &= \frac{J_{s2}^2}{\frac{1}{R}} = J_{s2}^2R \\ Y_m &= \frac{J_m^2}{Y_{s2}} = \frac{J_m^2}{J_{s2}^2R} \\ Y_{s1} &= \frac{J_{s1}^2}{Y_m} = \frac{J_{s1}^2J_{s2}^2R}{J_m^2} \end{aligned} \tag{2.13}$$

Therefore, the **Error! Reference source not found.** can be used to determine the J_{s1} and J_{S2} .

$$J_1J_3R = J_2 \tag{2.14}$$

Furthermore, the complete circuit, including the J-inverter, and the circuit excluding the J-inverter, can be calculated separately. By comparing these two equations, the values of the inductor and capacitor in the section of the circuit with the J-inverter can be determined. The equations below for the inductor and capacitor can be found in [20]:

$$
\begin{aligned}
C_{s1} &= \frac{J_1}{\omega_0\sqrt{1-(J_1R)^2}} \\
C_{s1e} &= \frac{C_{s1}}{1+(\omega_0 C_{s1}R)^2}
\end{aligned}
\tag{2.15}
$$

Also,

$$
\begin{aligned}
C_{s2} &= \frac{J_2}{\omega_0\sqrt{1-(J_2R)^2}} \\
C_{s2e} &= \frac{C_{s2}}{1+(\omega_0 C_{s2}R)^2}
\end{aligned}
\tag{2.16}
$$

Therefore, the paralleled capacitors can be figured out by **Error! Reference source not found.**.

$$
\begin{aligned}
C_{p1} = C_1^{'} - C_{s1e} \\
C_{p2} = C_2^{'} - C_{s2e}
\end{aligned}
\tag{2.17}
$$

To design a wireless power transfer (WPT) system using defected ground structure (DGS), several key steps need to be followed. Firstly, it is necessary to determine the resonance frequency and the inductance values of each device involved in the system, including the transmitter and receiver. Additionally, the mutual inductance between the transmitter and receiver must be determined as it plays a crucial role in the power transfer process.

Once these parameters are known, the value of J_2, which represents the coupling between the transmitter and receiver coils, can be determined using (3.9). Furthermore, (3.11) can be utilized to calculate the values of $J_{1,3}$, which provide important insights into the coupling coefficients.

Finally, (3.11) is employed to calculate the specific values of capacitors or inductors required for the system. This step is crucial for optimizing the performance and efficiency of the WPT system.

A visual representation of these design steps can be found in Figure 9, providing a clear and concise overview of the entire design process using DGS for wireless power transfer applications.

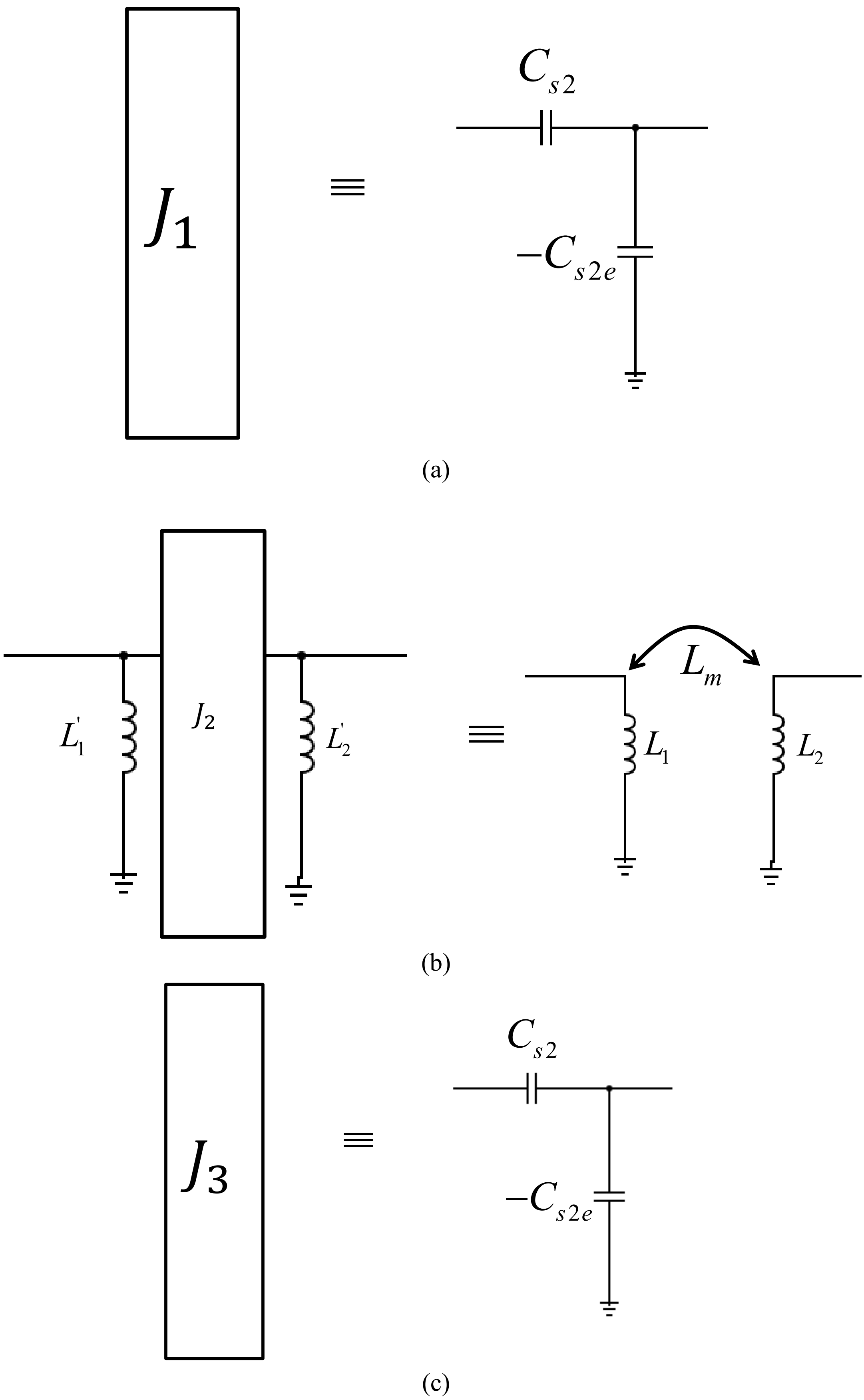

Fig. 7 Equivalent circuits of each J-inverter.

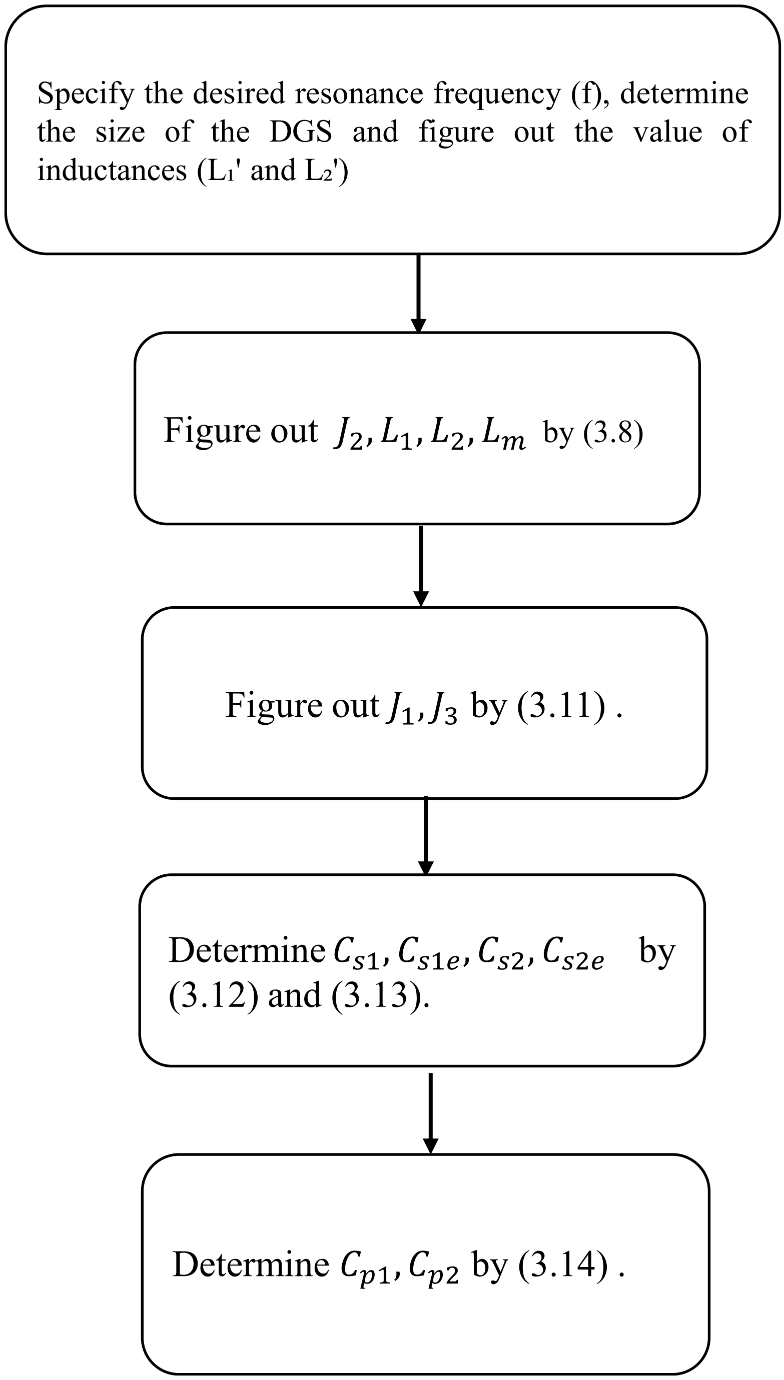

Fig. 8 Flowchart of DGS optimization.

2.4 An Overview of SWIPT

The advancement of portable and wearable electronic devices has created a demand for compact and efficient wireless charging systems. Simultaneous wireless information and power transfer (SWIPT) systems have emerged as a promising solution, offering improved energy harvesting [21], [22], utilization [22] capabilities, and enabling innovative applications in areas such as the Internet of Things (IoT) [23]–[25], wearable devices [6], [26], and so on [27].

In the pursuit of miniaturization, the SWIPT system utilizing frequency-shift keying (FSK) modulation was proposed by previous works [6], [28]. However, these systems faced challenges related to the optimization of capacitors in over-coupled resonators to achieve optimal power and signal transfer performance. For biomedical applications, the use of capacitive or resistive switching inside implanted devices necessitated the inclusion of an additional direct current source, which introduced potential risks to the human body [29]. Furthermore, the data transmission method employed in these systems resulted in a significant decrease in power transfer efficiency (PTE), leading to instability and prolonged battery charging times.

Addressing these challenges is crucial for the development of efficient SWIPT systems. By optimizing the design and configuration of resonators and addressing potential safety concerns related to implanted devices, we can enhance power and signal transfer performance while ensuring the well-being of users. Additionally, exploring alternative data transmission methods that minimize the impact on PTE is essential to achieve stable and efficient charging processes.

In summary, previous works have proposed SWIPT systems utilizing FSK modulation, but challenges regarding capacitor optimization, safety in biomedical applications, and power transfer efficiency reduction have been identified. Overcoming these challenges through innovative design strategies and alternative data transmission methods will contribute to the development of compact, efficient, and safe wireless charging systems for portable and wearable electronic devices.

2.5 Better Solution: DGS-Based Dual-band WPT System

To address the limitations of a single-band wireless power transfer (WPT) system, as depicted in Fig. 9, the adoption of a dual-band WPT system proves to be a more advantageous solution. In a dual-band system, two separate frequency bands are utilized to serve distinct purposes, enabling simultaneous power transfer and uninterrupted information transmission.

The primary band of the dual-band WPT system is dedicated to power transfer, ensuring efficient and reliable wireless charging capabilities. This band is optimized to maximize power transfer efficiency and deliver sufficient energy to the receiving device or load. By focusing solely on power transfer in this band, the system can provide a robust and reliable charging mechanism.

The second band of the dual-band WPT system is specifically allocated for information transmission. This band operates independently from the power transfer band, ensuring uninterrupted communication without interfering with the charging process. By segregating power and information transmission, the system can achieve efficient data transfer rates while maintaining optimal power transfer performance.

In summary, adopting a dual-band WPT system overcomes the drawbacks associated with single-band systems by utilizing separate frequency bands for power transfer and information transmission. This enables efficient and uninterrupted charging while maintaining reliable communication capabilities. The dual-band approach is a preferred choice for applications that require both power transfer and data connectivity, offering enhanced performance and versatility.

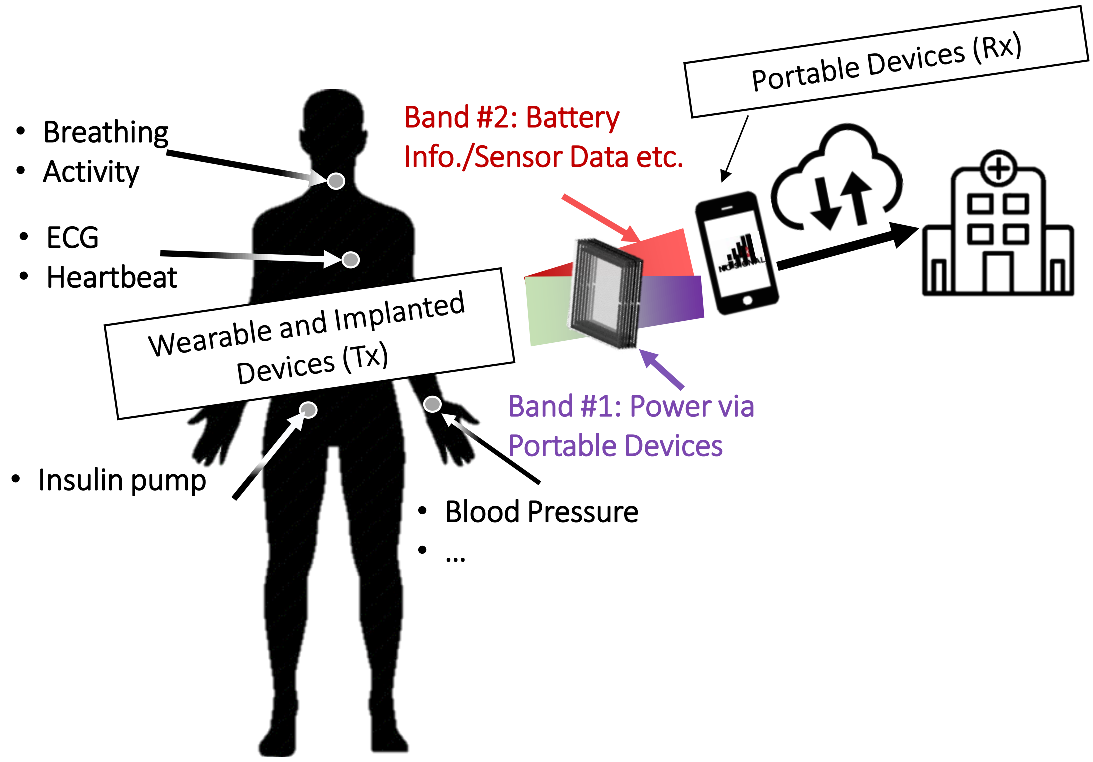

Fig. 9 A configuration of SWIPT using dual-band WPT system.

2.6 Problems to be Solved of a Dual-band WPT

When proposing a dual-band wireless power transfer (WPT) system, several technical problems are targeted for resolution:

- **Power Transfer Efficiency Optimization:** One of the primary objectives is to enhance the power transfer efficiency of the WPT system. By utilizing multiple frequency bands, the system can be optimized to efficiently transfer power from the transmitter to the receiver. This involves minimizing losses, impedance matching, and maximizing energy transfer within each band.

- **Interference Mitigation:** The dual-band system aims to address the issue of interference between power transfer and information transmission. It targets the reduction of mutual interference between the two bands to ensure uninterrupted data communication while maintaining optimal power transfer performance. This requires careful design and allocation of frequency bands to minimize cross-band interference.

- **Lateral Misalignment Tolerance:** Another challenge to overcome is the reduction of sensitivity to lateral misalignment between the transmitter and receiver coils. Lateral misalignment can significantly impact the power transfer efficiency in a WPT system. By utilizing dual-band operation, the system can incorporate design features that mitigate the effects of misalignment, thereby improving overall performance and charging reliability.

- **Signal Quality Improvement:** In a dual-band WPT system, the information transmission band aims to provide high-quality signal transmission without compromising the power transfer performance. This requires optimizing the system's design parameters, such as resonant frequencies, bandwidth, and impedance matching, to ensure reliable and efficient data communication.

- **Dimension Optimization:** Achieving optimal system dimensions is crucial for the dual-band WPT system's performance. The system must be designed to efficiently utilize the available space while accommodating both power transfer and information transmission functionalities. Dimension optimization includes determining the appropriate sizes and arrangements of the coils, resonators, and other components to achieve the desired performance in both frequency bands.

By addressing these technical challenges, a dual-band WPT system can improve power transfer efficiency, mitigate interference, enhance misalignment tolerance, and achieve high-quality signal transmission. These advancements enable the system to meet the requirements of various applications, such as wireless charging for portable devices, IoT devices, and other wireless energy transfer applications.

3 Metamaterial for Efficient and Robust Dual-band Wireless Power Transfer

The demand for compact and efficient wireless power transfer (WPT) systems for portable devices is increasing. Compared to coil-based systems, defected ground structure (DGS)-based multi-band WPT systems have demonstrated better performance in terms of the figure of merit (FOM) [8], [12], [13], [18].

Fig. 10 the configuration of a proposed dual-band wireless power transfer (WPT) system is depicted. This system incorporates a defected ground structure (DGS) that exhibits band stop filter (BSF) characteristics as its dominant mode. By properly loading the DGS with capacitance, it can effectively function as an inductor. This unique combination of DGS inductance and loading capacitance offers increased flexibility in adjusting the system's geometry to optimize its performance.

The dimension optimization process for this dual-band WPT system has been carried out using the admittance inverter method. This method allows for the adjustment of parameters based on the desired system characteristics and performance requirements. The optimized dimensions of the system, determined through the admittance inverter method, are presented in

TABLE 1.

Furthermore, two DGS resonators are overlapped to achieve further layout compactness. The resulting system exhibits dual-band characteristics, as depicted in Fig. 11 when the transmitter (Tx) and receiver (Rx) are positioned face-to-face. The wireless power transfer efficiency (η) can be described by:

$$\eta = |S_{21}|^2 \times 100\% \tag{3.1}$$

It should be noted that a discrepancy can be observed in the higher band within the distance range of 12 mm to 15 mm. This is due to losses in the soldered capacitors during the fabrication process. However, as shown in Fig. 12, beyond a distance of 16 mm, the power transfer efficiency (PTE) sharply drops and becomes less than 20% for both bands when the WPT distance reaches 20 mm. Therefore, recent works have proposed the use of metamaterials [14]–[16], [19], [30]–[32] to further enhance power transfer efficiency.

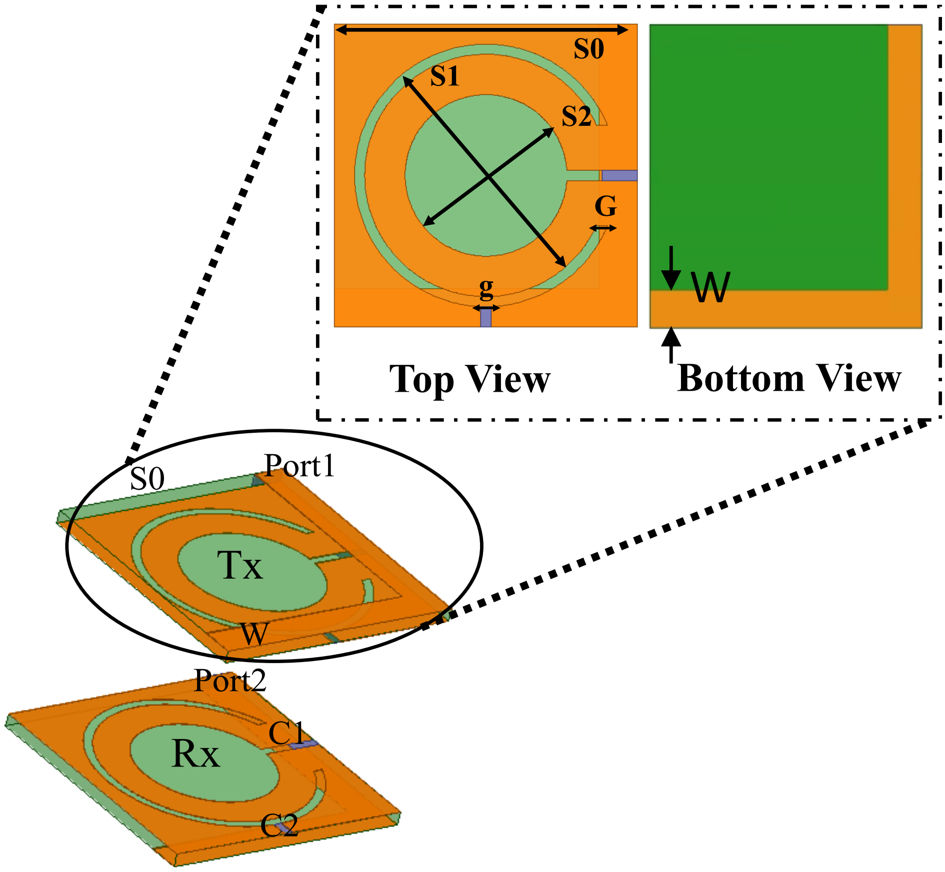

Fig. 10 Configuration of the proposed DGS-based dual-band WPT system.

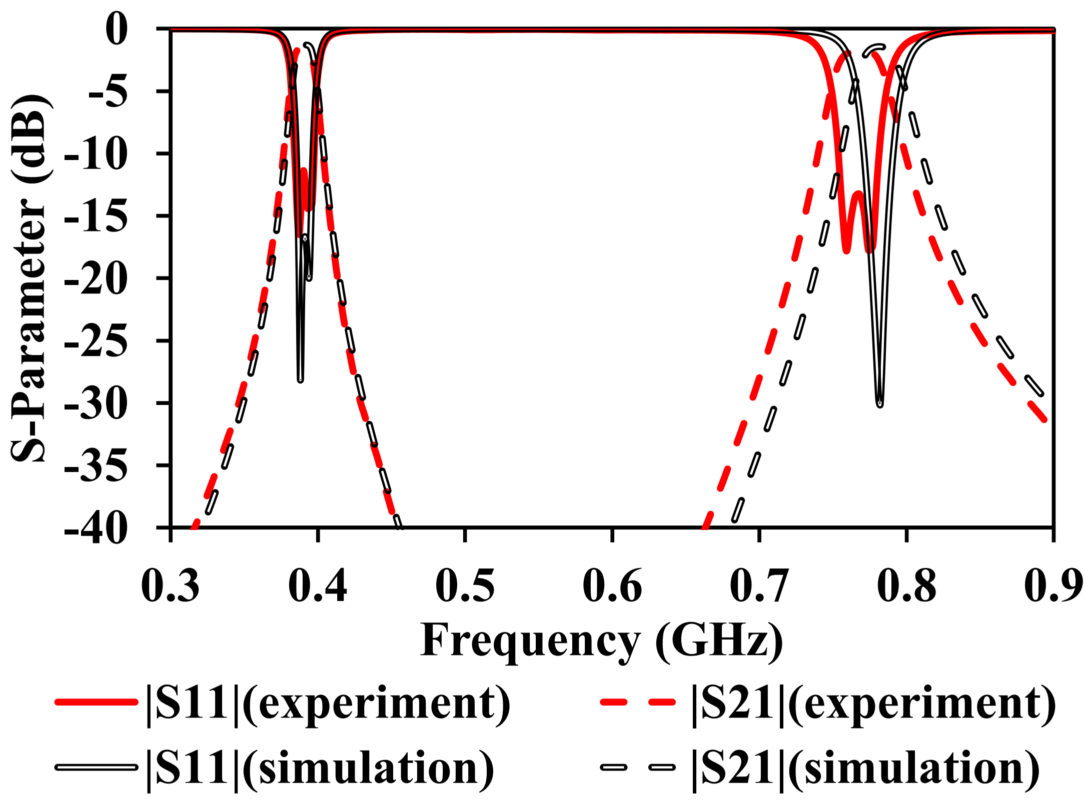

Fig. 11 Simulated and measured S-parameter of the proposed dual-band WPT system. The whole system exhibits dual-band characteristics when the Tx and Rx are placed face-to-face.

TABLE 1 Dimension of the proposed dual-band WPT system

Notation	Description	Value(mm)
S0	Overall size of Tx and Rx	15
S1	Radius of the outer circle	6
S2	Radius of the inner circle	4
g	Gap for the capacitor on chip	0.5
G	Gap	0.51
W	Fed line width on receiver	1.9
C1	Chip capacitor	10pF
C2	Chip capacitor	2pF
	Copper thickness	0.017
	Substrate thickness	0.762
	Relative permittivity	3
	Loss tangent	0.0013

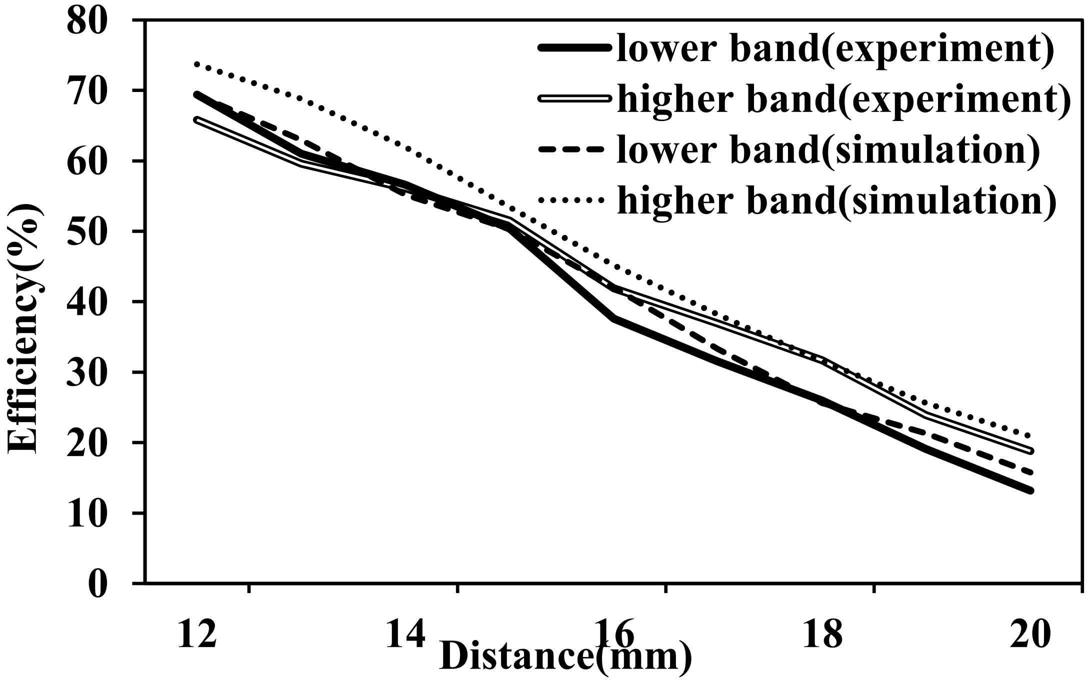

Fig. 12 Simulated and measured efficiencies when the WPT distance varies from 12 to 20 mm.

3.1 Artificial Perfect Electromagnetic Lens – Metamaterial

Fig. 13 illustrates the fundamental pattern of a conventional metamaterial, which is constructed by arranging unit cells in a periodic manner. In recent times, the utilization of metamaterials in near-field wireless power transfer (especially when the WPT distance d $> 0.02\lambda$ [33]) has been increasingly prevalent. These metamaterials find applications in various domains, such as wireless charger modules for workstations [17], medical applications [34], and so on [32]. When compared to conventional magnetic relays like aluminum and ferrite, metamaterials exhibit substantially enhanced performance in facilitating the efficiency of evanescent waves [17], [32], [33]. This improved performance can be attributed to a focusing effect that arises from the unique properties of the Metamaterial. Furthermore, in [32], this specific type of Metamaterial is characterized as a relay-enhanced metamaterial. To achieve the desired focusing effect, the proposed Metamaterial should possess a permeability that is close to zero in both the real and imaginary parts [35]. In the subsequent section, the underlying mechanism of this Metamaterial will be elucidated.

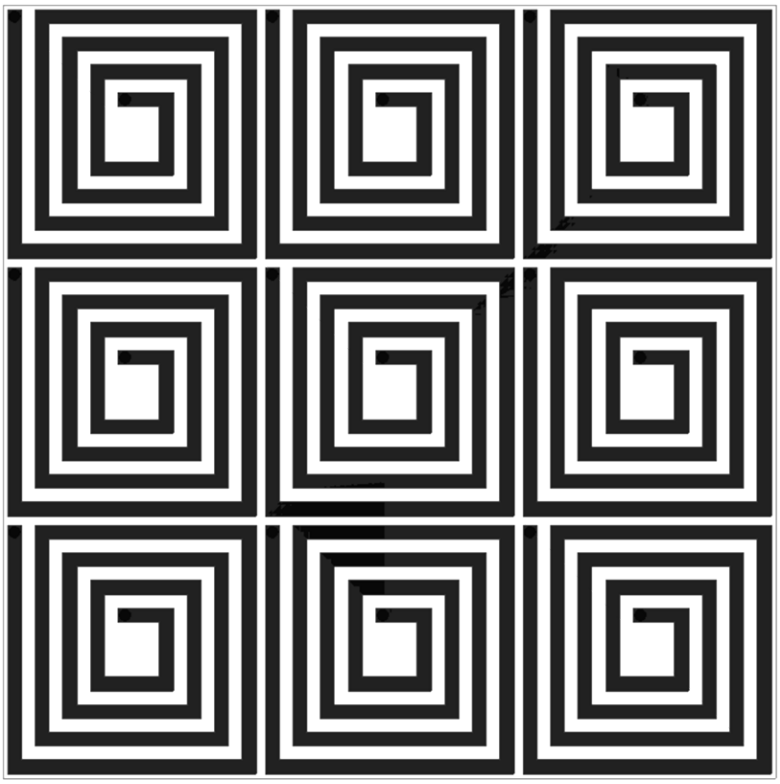

Fig. 13 Pattern of a conventional metamaterial.

3.2 Dielectric Characteristic: Permeability

To delve into the concept of achieving negative or near-zero permeability in a metamaterial, this subsection introduces an approach. Fig. 4 showcases the fundamental configuration, which comprises an array of infinite cylinders. It is important to note that each cylinder possesses an infinite length, allowing the magnetic field along each cylinder to be considered parallel to the cylinder itself. [35].

Then to balance the total electromotive force (emf) around the circumference of a cylinder, the current *j* can be determined by [35]:

$$j = \frac{-H_0}{\left[1 - \frac{\pi r^2}{a^2}\right] + i\frac{2r\sigma}{\omega r^2 \mu_0}} \tag{3.2}$$

Also, the B-field of the unit cell is

$$B_{ave} = \mu_0 H_0 \tag{3.3}$$

And the average H-field over a line outside the cylinder is [35] :

$$H_{ave} = H_0 - \frac{\pi r^2}{a^2} j \tag{3.4}$$

Here a stands for the size of a cylinder-inclusive cube. The cubic is viewed as a unit cell for the periodic array's analysis. So that the effective permeability of this infinite conducting cylinder array is [35]:

$$\mu_{eff} = \frac{B_{ave}}{\mu_o H_{ave}} = 1 - \frac{\pi r^2}{a^2}\left[1 + i\frac{2\sigma}{\omega r \mu_0}\right]^{-1} \tag{3.5}$$

To minimize the purely electrical effects, in [35], the cylinder is furtherly sliced into infinite rings. Noticed that the distance between each sliced ring (l) is supposed to be less than the radius of the rings ($l < r$). So that the effective permeability of the sliced structure is [36]:

$$\mu_{eff}(\omega) = 1 - \frac{F\omega_0^2}{\omega^2 - \omega_0^2 - i\omega\Gamma} \tag{3.6}$$

Here ω_0 is the resonance frequency at which μ_{eff} diverges[35]. F, Γ are constants that have to do with the artificial medium's geometry and materials.

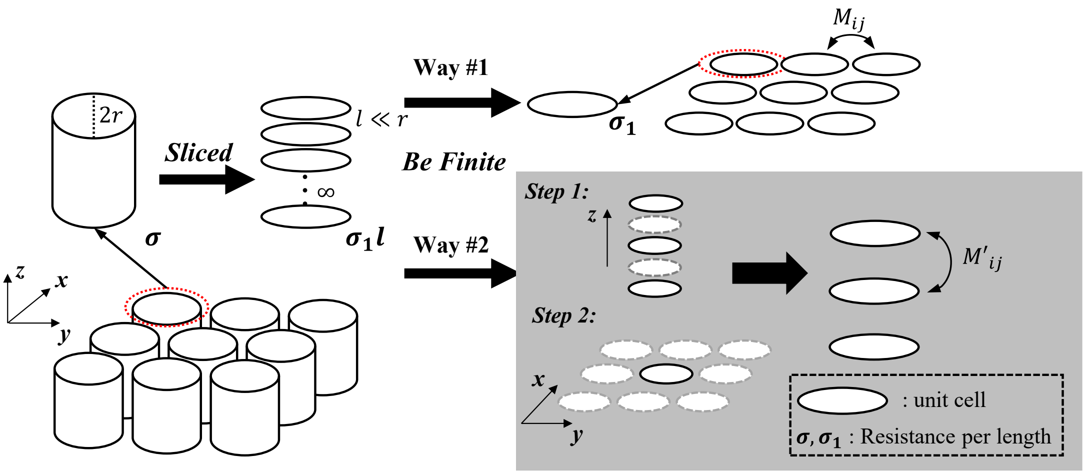

Fig. 14 Different ways to make the finite Metamaterial. l stands for the distance between the rings in the

z-direction, which is supposed to be far smaller than the radius r to ensure that the current flows are essentially the same as those in a continuous cylinder.

3.3 Conventional 1-dimensional (1D) Metamaterial

3.3.1 Limitation of Conventional Metamaterial

To enhance the magnetic coupling between the transmitter (Tx) and the receiver (Rx), several relay-enhanced metamaterials with near-zero permeability have been proposed [11], [13]–[24]. These metamaterials have been found to improve the performance of wireless power transfer (WPT) by minimizing power transfer efficiency (PTE) reduction caused by lateral misalignment [20] and the WPT distance [23].

However, conventional 1D metamaterials exhibit limited performance when placed in the middle of a dual-band system within the near-field region. Fig. 15 compares the WPT system without and with a conventional 1D metamaterial proposed in [37]. Although the proposed Metamaterial shows improvement in the higher band, there is only a modest 4% enhancement in PTE observed in the lower band.

On the other hand, recent studies have explored the use of the second mode of resonators or broadside resonance [17] to enhance the PTE for the dual-band WPT. However, in [17], the improvement in the higher band is considerably lower compared to the other band. This can be attributed to the fact that, according to (4.7), the resonant enhancement of the Metamaterial strongly depends on the resistance per length ($Q_e \propto \sigma^{-2}$) generated from the material itself. Consequently, similar to [17], the second mode of the split ring resonator (SRR) exhibits higher resistivity compared to the first mode, resulting in minimal enhancements in the other band.

$$Q_e = \left| \frac{\pi \omega^2 r^3 \mu_0}{4 l \sigma d c_0} \right|^2 \tag{3.7}$$

Furthermore, [33] highlights the significant correlation between the equivalent surface impedance (Z_s) and the coupling amplitude (L_{21}). [33] illustrates that when the Z_s comes to $j25\,\Omega$, the mutual inductance amplitude is maximized. This finding emphasizes the importance of carefully tuning the surface impedance to optimize the coupling efficiency in the WPT system.

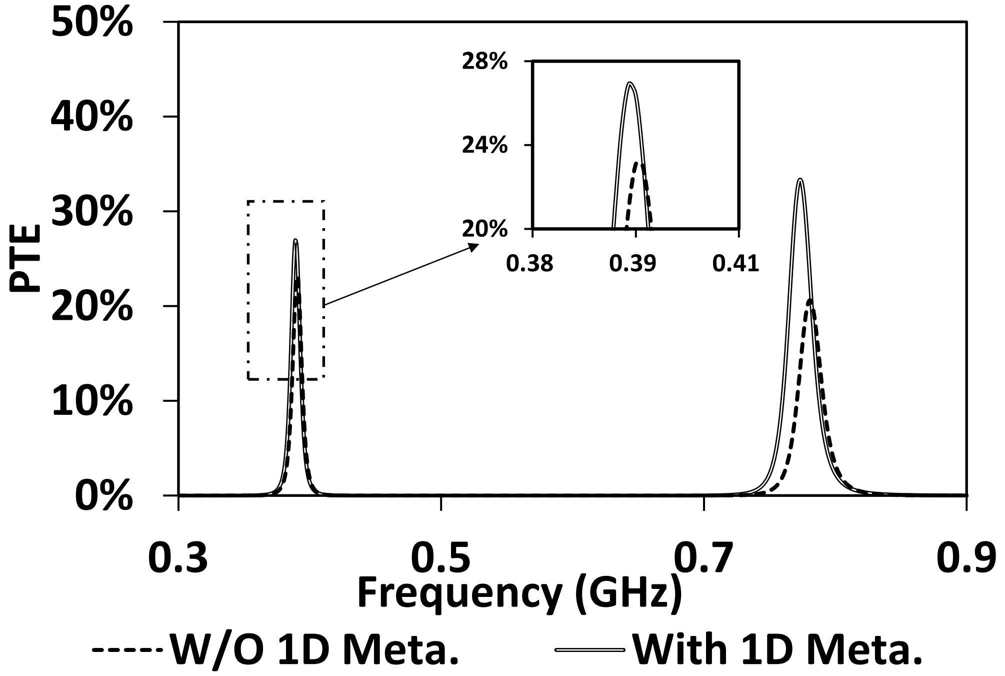

Fig. 15 PTE results of the proposed WPT system without (W/O 1D Meta.) and with (With 1D Meta.) the Metamaterial proposed in [37].

3.3.2 Requirement of Wideband

In order to minimize the mutual-interference of the proposed dual-band WPT, the frequencies of both bands is supposed to be carefully considered

A model of the proposed dual-band wireless power transfer (WPT) system utilizing the defected ground structure (DGS) is illustrated in Fig. 16. The DGS is designed to operate at two distinct frequencies, represented by the inner and outer circles in the figure. The objective is to achieve efficient power transfer at both of these frequencies.

Additionally, it is crucial to minimize the mutual inductance (M) between the transmitter and receiver coils. By reducing the mutual inductance, the system can enhance the overall performance and reliability of the WPT system. Minimizing mutual inductance helps to mitigate interference and improve the power transfer efficiency between the coils, ensuring optimal operation of the proposed dual-band WPT system.

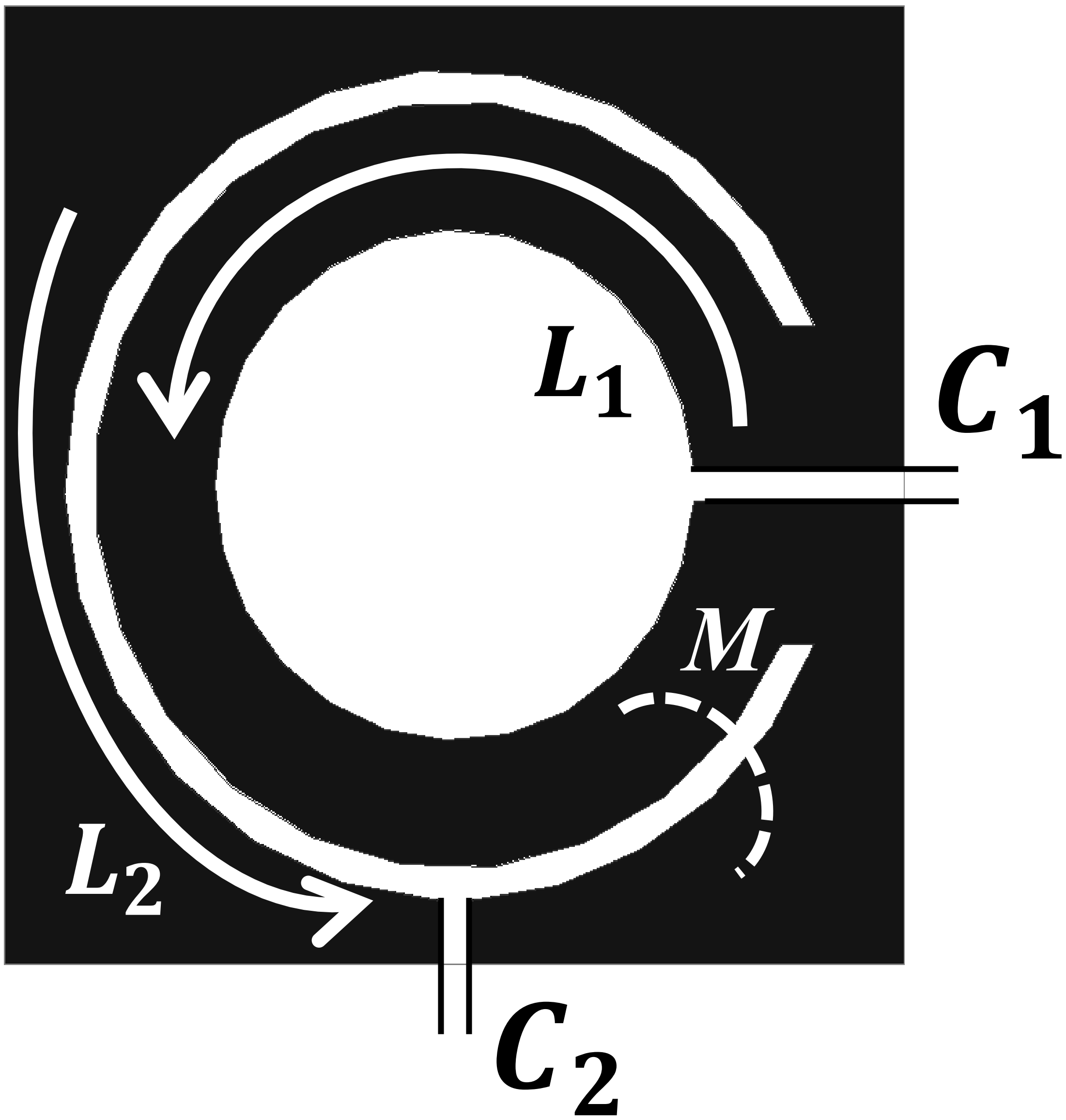

Fig. 16 Layoput modeling of the proposed DGS for the dual-band WPT.

Fig. 17 presents the equivalent circuit of the transmitter (Tx) and receiver (Rx) depicted in Fig. 17. With this circuit configuration, we can calculate the voltage difference between the two specified points shown in Fig. 17. By applying appropriate circuit analysis techniques, such as Kirchhoff's laws or voltage division, the voltage difference can be determined. This calculation allows for a deeper understanding of the electrical behavior and characteristics of the transmitter and receiver circuits in the wireless power transfer system.

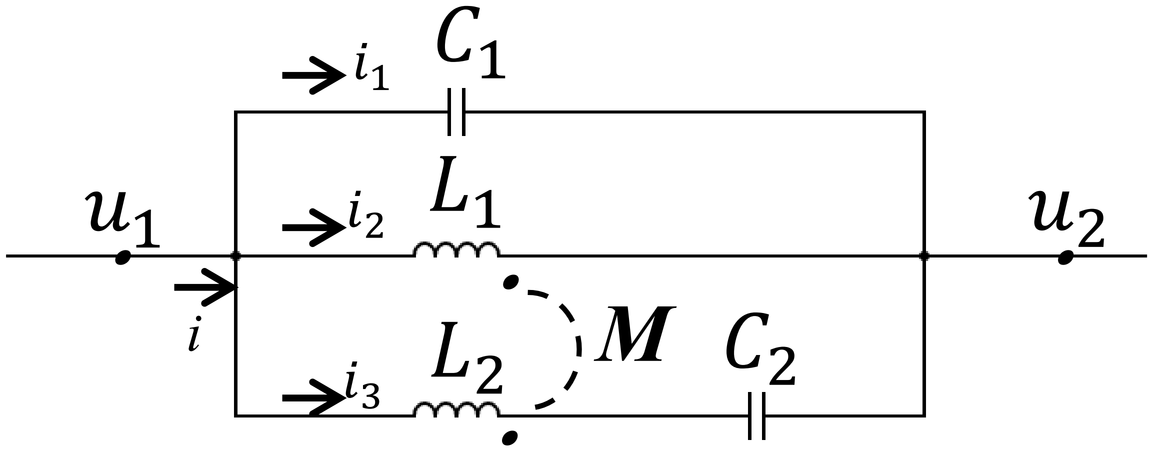

Fig. 17 its equivalent circuits. $u_{1,2}$ is the electric potential (voltage) of each point. $\boldsymbol{M}$ is the mutual inductance between two loops

The voltage difference between the two points can be calculated as:

$$\begin{aligned} u_2 - u_1 &= i_1 \cdot \frac{1}{j\omega C_1} \\ &= i_2 \cdot j\omega L_1 + i_3 \cdot j\omega M \\ &= i_3 \cdot \left(j\omega L_2 + \frac{1}{j\omega C_2} \right) + i_2 \cdot j\omega M \end{aligned} \tag{3.8}$$

Therefore the admittance for the whole system $\boldsymbol{Y}$ can be donated as :

$$\boldsymbol{Y} = \frac{\sum_{p=1}^{3} i_p}{u_2 - u_1} = \frac{\boldsymbol{A}}{\boldsymbol{B}} \tag{3.9}$$

When $\boldsymbol{A}$ = 0, the whole system can be seen as an open circuit, resulting in the characteristics of band stop. The resonant frequency ω can be calculated as:

$$\omega = \left(\frac{\xi \pm \sqrt{\xi^2 - 2\eta}}{\eta} \right)^{\frac{1}{2}} \tag{3.10}$$

Here, we denote a couple of notations to make the solution easier to understand, as listed in (5.11).

$$\begin{aligned} &\eta = 2C_1(L_1\beta + MF^{-1}) \\ &\xi = F^{-1} + \beta + C_1L_1 \\ &\beta = {}^{E}\!/_{F} \\ &E = {}^{(L_2 - M)}\!\big/_{(L_1 - M)} \\ &F = \mathrm{C}_2^{-1}(L_1 - M)^{-1} \end{aligned} \tag{3.11}$$

Hence, when the system exhibited two resonance frequencies, two conditions below are supposed to be satisfied:

$$\omega = \left(\frac{\xi \pm \sqrt{\xi^2 - 2\eta}}{\eta}\right)^{\frac{1}{2}} > 0 \tag{3.12}$$

$$\xi^2 - 2\eta > 0 \tag{3.13}$$

Apparently, since ξ, η are positive and real numbers, $\xi-\sqrt{\xi^2-2\eta}>0$, which meets (3.12).

On the other side, to meet (A.7), the following inequality is supposed to be satisfied:

$$\begin{aligned} &[C_2(L_1 - M) + C_2(L_2 - M) + C_1L_1]^2 \\ &\qquad -4C_1[L_1C_2(L_2 - M) + MF^{-1}] > 0 \end{aligned} \tag{3.13}$$

Based on the topology of the proposed DGS, we can assume that: $L_1 \approx L_2$ Therefore the mutual inductance (M) can be calculated as:

$$M = k \times \sqrt{L_1L_2} \approx k \times L_1 \tag{3.14}$$

Also, we can assume that the value of $C_1 = \rho C_2$. So that the inequality can be simplified as:

$$C_2^2L_1^2\{\rho^2 + 2[k(k-2)]\rho + [2(1-k)^2]\} > 0 \tag{3.15}$$

Where we assume that

$$h(k) = \rho^2 + 2[k(k-2)]\rho + [2(1-k)^2] \quad (3.16)$$

Therefore, we can get that when $k = 1$, $h(k)$ is minimum, which can be written as:

$$\text{argmin}\{h(k)\} = h(1) = \rho^2 - 2\rho > 0 \ (\rho > 0) \quad (3.17)$$

The formula above means that for any value of k, the $h(k)$ is supposed to be bigger than ρ^2-2ρ.

Consequently, when the value of capacitor C1 is twice as large as that of capacitor C2 ($\rho > 2$), the entire transmitter (Tx) or receiver (Rx) system exhibits dual-band bandstop characteristics. In our proposed dual-band WPT system, the capacitor values are set as C1 = 10 pF and C2 = 2 pF, respectively, leading to the occurrence of dual-band bandstop characteristics.

However, when the Tx and Rx are placed back-to-back, as demonstrated in previous works [9], [10], [38], the system exhibits bandpass characteristics instead. This configuration allows for selective transmission and reception of signals in the desired frequency bands, enabling efficient dual-band wireless power transfer while maintaining communication capabilities.

3.3.3 Simulation Validation

As per equation (3.17), it is essential for the capacitance of C_1 to be twice as large as C_2 ($C_1 > 2C_2$). Failure to meet this condition, as depicted in Fig. 18, would result in a degradation of the dual-band characteristics. Therefore, in order to enhance the performance of the system, it is necessary to propose a wider band of metamaterial. By expanding the bandwidth of the metamaterial, the dual-band WPT system can achieve improved performance and maintain the desired dual-band characteristics.

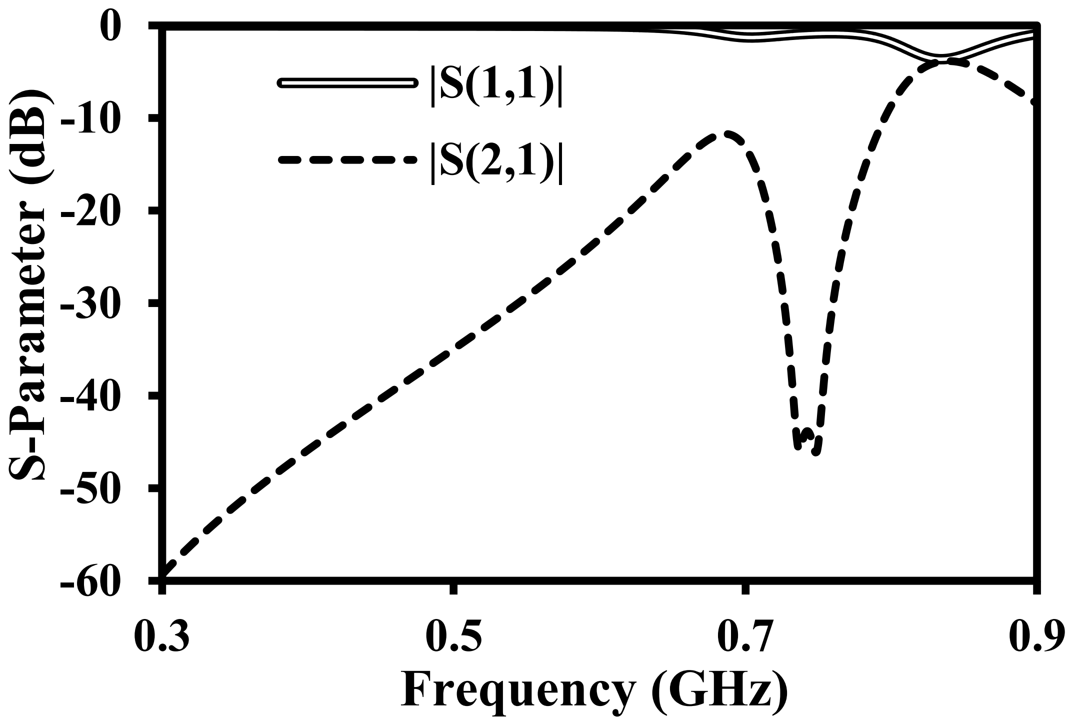

Fig. 18 . Proposed dual band WPT's simulated performance when $C_1<2C_2$.

3.4 Conclusion

In this section, we have introduced conventional metamaterials that are commonly positioned within the proposed wireless power transfer (WPT) system, between the transmitter (Tx) and the receiver (Rx), for near-field studies. The optimization of these metamaterials is crucial to achieve improved efficiency performance, requiring their permeability to approach zero in both the real and imaginary parts within the desired frequency range.

However, conventional metamaterials are limited to being effective in only one band for dual-band WPT systems. Although attempts can be made to enhance performance in the other band by utilizing the second resonance frequency of conventional metamaterials, the improvements are often restricted. To overcome these limitations, we propose the use of stacked metamaterials that meet the following requirements:

- The stacked metamaterial should be capable of improving efficiency in both bands simultaneously and equally. This enables balanced performance enhancement across the entire dual-band spectrum.

- Wide band characteristics should be considered in the design of the stacked metamaterial to avoid mutual interference. By incorporating wider band properties, the stacked metamaterial can effectively manage and mitigate potential interference issues within the dual-band WPT system.

By fulfilling these requirements, the proposed stacked metamaterials offer a promising solution for optimizing the efficiency and performance of dual-band WPT systems, ensuring effective and reliable power transfer in both frequency bands.

4 Multimode Metamaterial

In this chapter, we present a novel multi-mode metamaterial designed specifically for dual-band wireless power transfer (WPT) systems. The proposed Metamaterial offers enhanced capabilities to operate efficiently and effectively in dual-band.

4.1 Stacked Metamaterial

[19] first proposed a novel stacked Metamaterial for compact and efficient wireless power transfer through biological tissues. Similar to 1-D topology metamaterial, the stacked Metamaterial behaves as a “perfect lens” because of the near-zero or negative permeability [19]. Given that the whole system includes a pair of inductive loops and stacked Metamaterial, the magnetic dispersion in the cylindrical system can be figured out by [19]:

$$\frac{k_\rho^2}{\mu_z}+\frac{k_z^2}{\mu_\rho}=\frac{\omega^2}{c^2}\varepsilon_\varphi \tag{4.1}$$

In the proposed multi-mode Metamaterial for dual-band WPT systems, the wavenumbers and permeabilities in the ρ- and z-directions, denoted as $k_{\rho,z}, \mu_{\rho,z}$, respectively, play a crucial role. The operating frequency is represented by ω, while c represents the speed of light in free space. Additionally, ε_φ represents the permittivity in the φ-direction.

One of the key advantages of the stacked Metamaterial is its near-zero permeability. This property enables the Metamaterial to manipulate the propagation of waves in the ρ-direction. As a result, the wave is effectively redirected into the z-direction, leading to a stronger coupling between the transmitter and receiver loops, as shown in Fig. 19. This enhanced coupling contributes to an overall improvement in wireless power transfer (WPT) efficiency. By utilizing the near-zero-permeability property of the stacked Metamaterial, we can optimize the WPT system's performance and achieve higher efficiency levels.

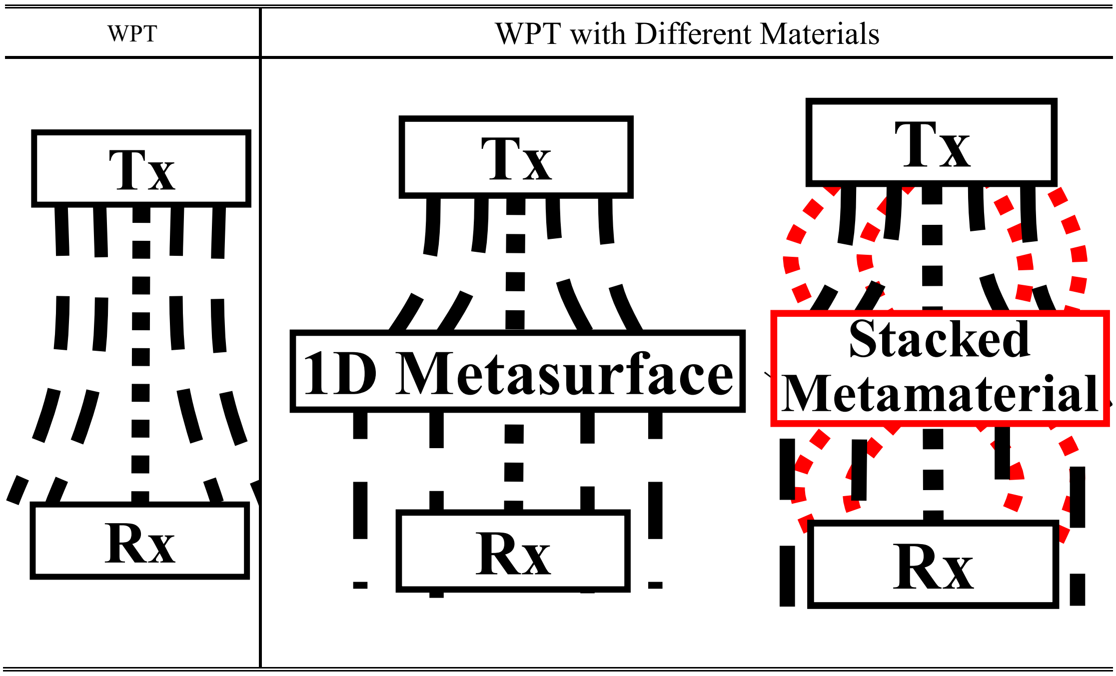

Fig. 19 WPT system (a) without material in the middle, (b) with conventional 1D-topology metasurface, and (b) with proposed stacked metamaterial. The dotted line stands for the magnetic wave empowered by the paralleled resonance derived from the stacked metamaterial, respectively

4.2 Permeability and Polarization Analysis

4.2.1 Permeability Analysis

Based on the previously mentioned stacked metasurface configuration, we propose two types of metasurfaces that are effective at either the lower or higher band, utilizing rotational split-ring resonators (SRRs). In order to achieve the desired enhancement effect in the near-field WPT system, these metasurfaces must satisfy two important conditions [19].

The first condition is that the real part of the permeability in the z-direction, denoted as $\mathrm{Re}(\mu_z)$, should be less than 1. This ensures that the magnetic field is enforced towards the Rx. Simultaneously, the imaginary part of the permeability should be near zero to minimize any loss caused by the Metamaterial itself. Additionally, the entire WPT system, including the Tx, metasurface, and Rx, should be impedance matched at the same resonance frequency for optimal performance.

The self-resonance frequency on an individual split-ring resonator (SRR) of each metasurface can be reasonably estimated using the following [39]:

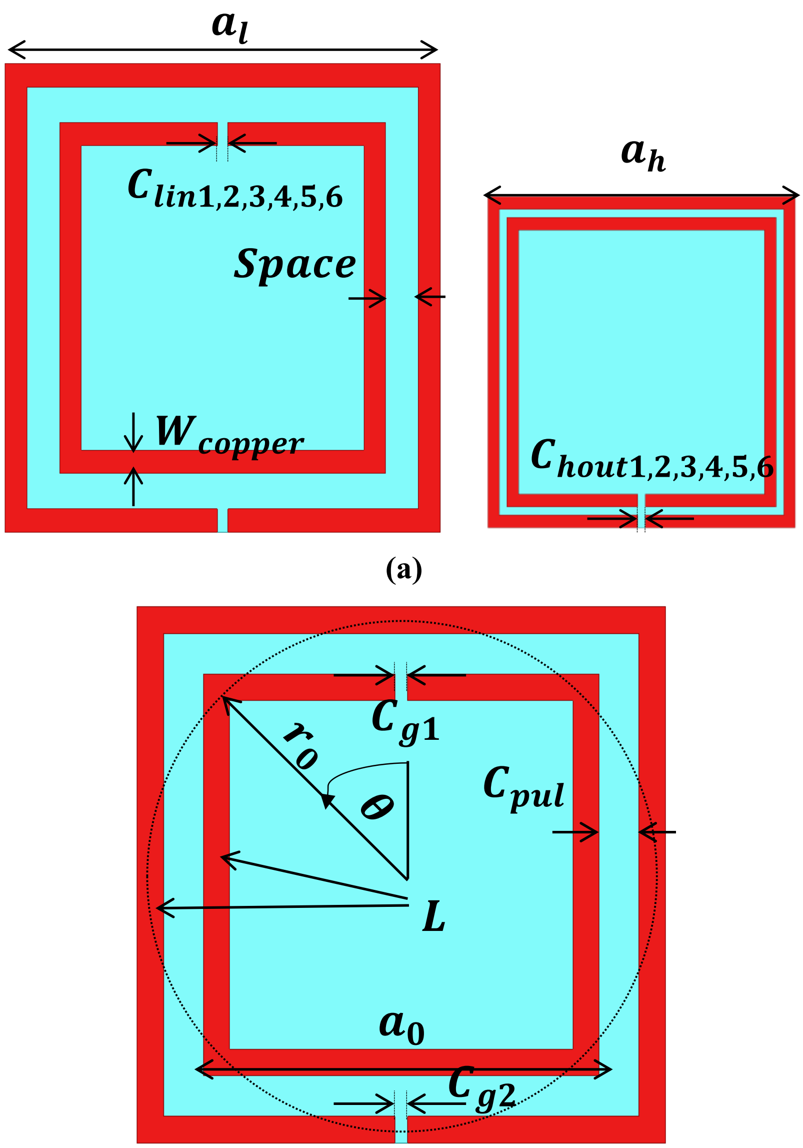

(b)

Fig. 20 (a) Structure of the square SRR and (b) its approximation to a circular ring shown in the dashed line.

$$f_0 = \frac{1}{2\pi\sqrt{2r_0L\frac{(\pi+k)^2-\theta^2}{2(\pi+k)}C_{pul}}} \tag{4.2}$$

Here, L represents the total inductance of the SRR, C_{pul} is the per unit length capacitance, and θ is the rotation angle. The parameter k is defined as $\frac{C_g}{r_0C_{pul}}$, where C_g represents the gap capacitances, and r_0 is the average radius of the inner rings. The dimensions is also depicted in Fig. 20.

To estimate the magnetic loss inside the metasurface, we apply the complex Poynting vector, which can be described as:

$$\boldsymbol{S} = \frac{1}{2} Re[\boldsymbol{E} \times \boldsymbol{H}^*] \tag{4.3}$$

Therefore, the observed energy (E) in the closed region around metasurface (V) can be depicted as [40]:

$$\begin{aligned} W &= -\frac{1}{2}\iint_S Re[\boldsymbol{E} \times \boldsymbol{H}^*] \cdot d\boldsymbol{s} = -\frac{1}{2} Re \iiint_V div\,(E \times H^*)\,dv \\ &= \frac{1}{2}\iiint_V (\omega\varepsilon''\boldsymbol{E}\cdot\boldsymbol{E}^* + \omega\mu''\boldsymbol{H}\cdot\boldsymbol{H}^* + \sigma\boldsymbol{E}\cdot\boldsymbol{E}^*)dv \end{aligned} \tag{4.4}$$

Here, ε'' and μ'' stands for the imaginary part of permittivity and permeability, respectively. Therefore, when the imaginary part of the permeability is almost zero, the magnetic wave beam can go through the 4.674-mm-thick metasurface over then more with merely low loss,

By analyzing these factors and utilizing (4.4), the self-resonance frequency of each metasurface's SRR can be reasonably estimated, enabling the design and optimization of the dual-band WPT system.

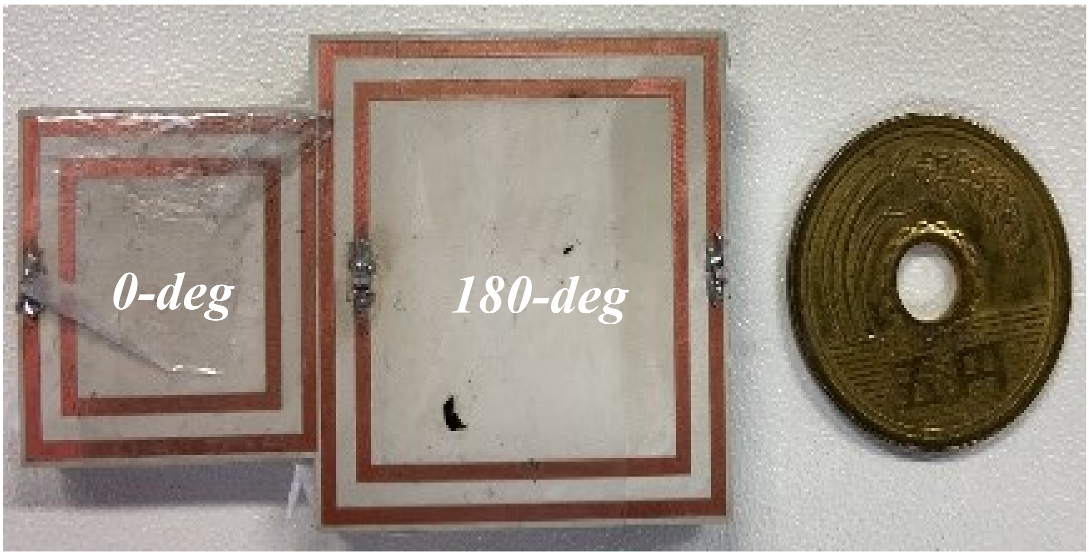

Fig. 21 Proposed metasurface. “0-deg” stands for the 0-degree Metamaterial, and “180-deg” stands for the 180-degree Metamaterial.

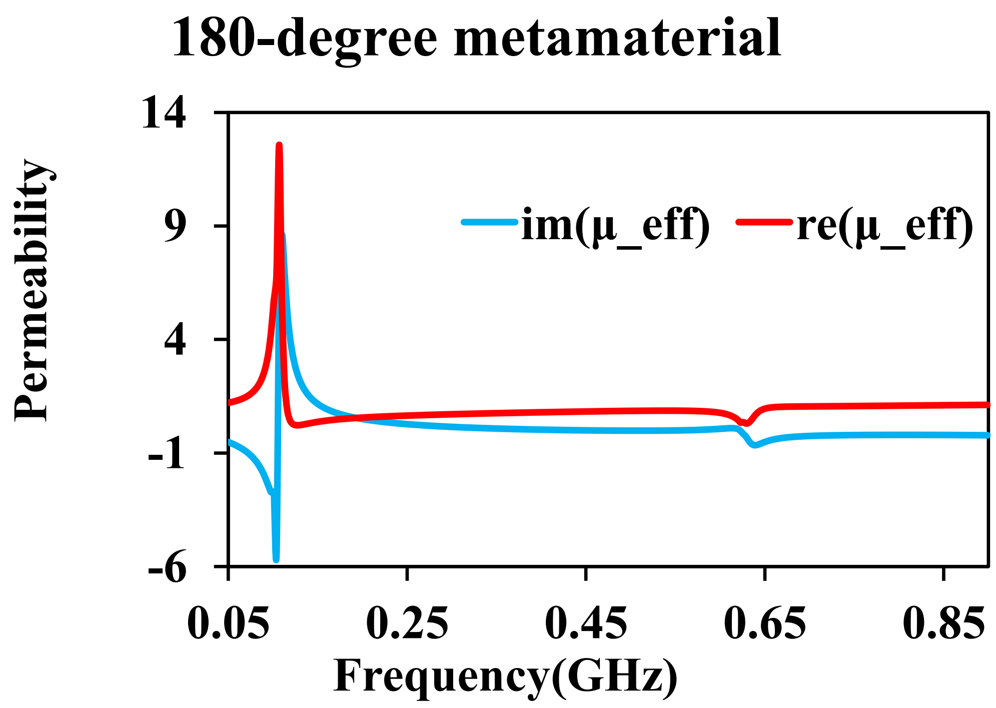

(a)

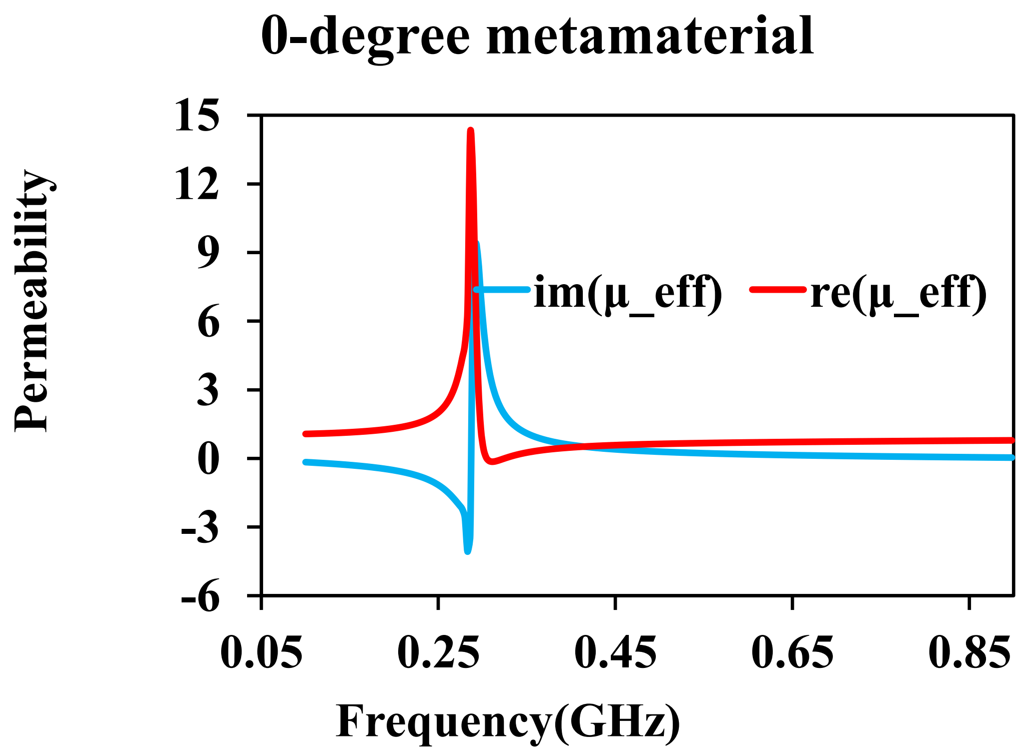

(b)

Fig. 22 Permeability of the proposed 180- and 0- degree Metamaterial.

4.2.2 Polarization Analysis

The metasurface shown in Fig. 21 is constructed by combining the 180-degree and 0-degree metasurface on each side. However, when these two types of metasurface are arranged together, cross-polarization occurs, resulting from the strong interference between these two metasurfaces [41]. As a result, a massive reduction in efficiency occurs. As a solution, the polarization of the field through each SSR can be easily changed by modifying the position of each SSR [42].

4.2.3 Simulation Results and Analysis

The high-frequency simulation software (HFSS) was employed for the simulation. The permeabilities of these two metasurfaces are estimated the same way as the former work [19] in Fig. 22 to satisfy the two conditions on each band.

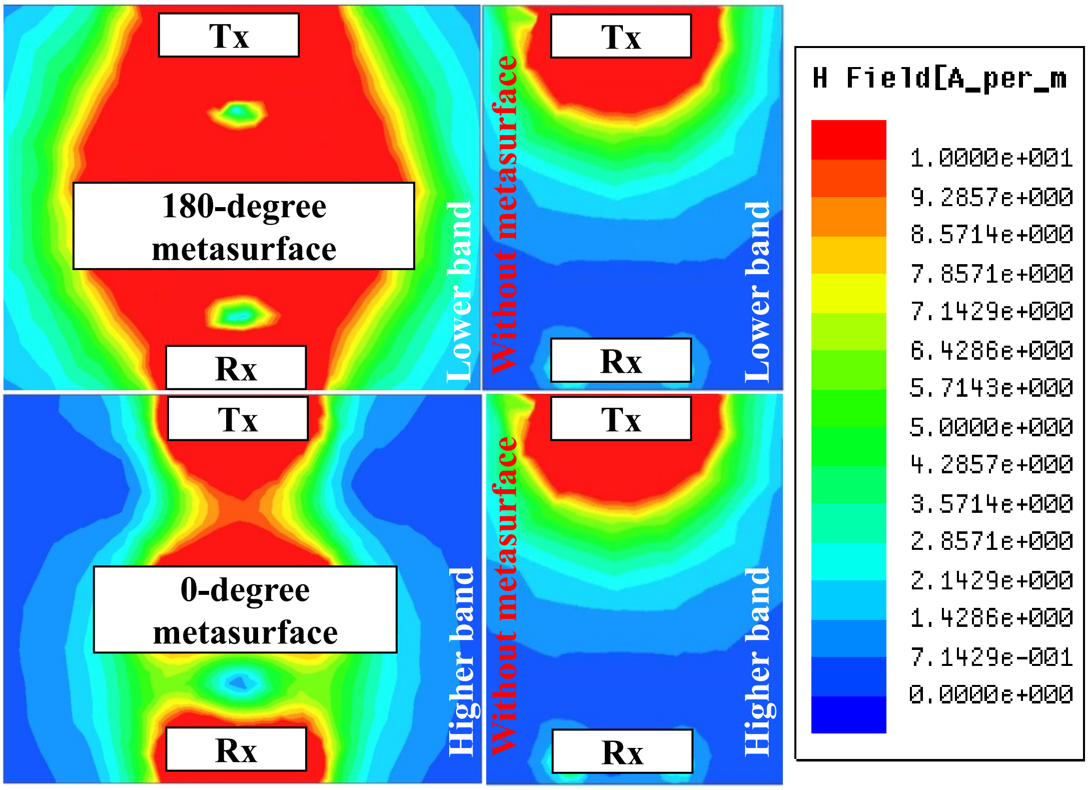

Fig. 23 Comparision between EM simulation of the system with/without Metamaterial at a WPT distance of 40 mm, which was chosen because the power transfer efficiency is almost zero at this point in the case of without a metamaterial.

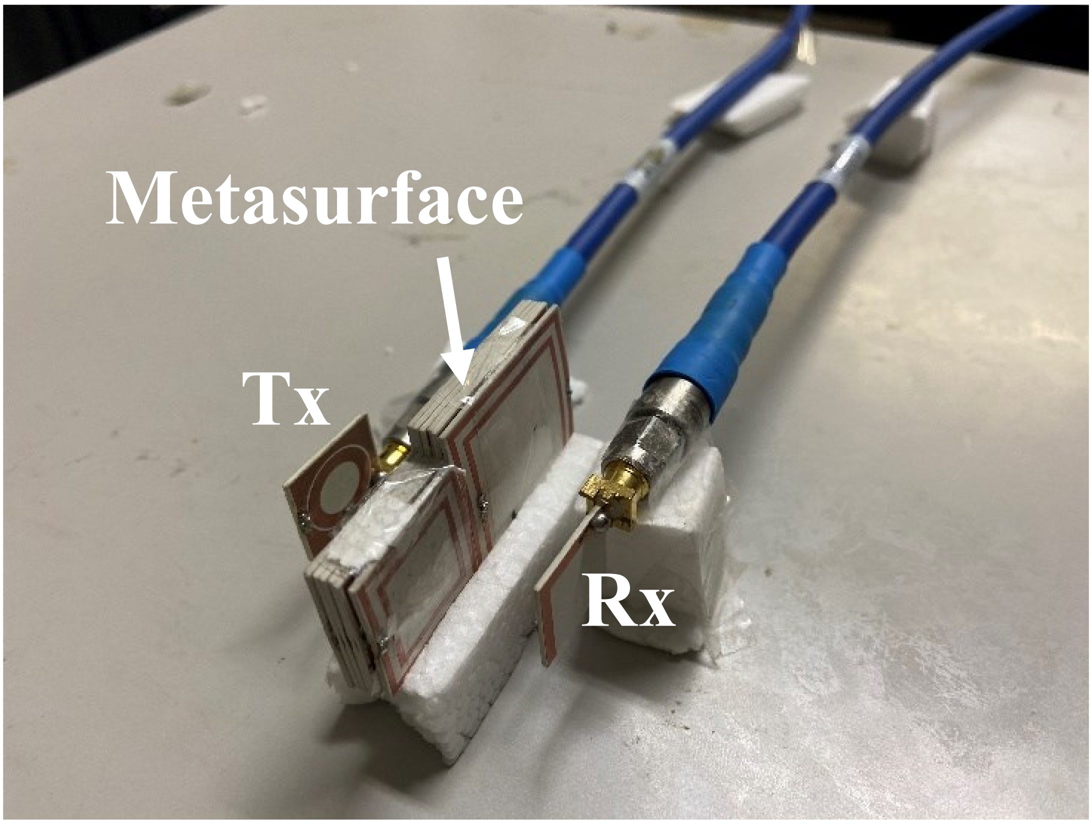

(a)

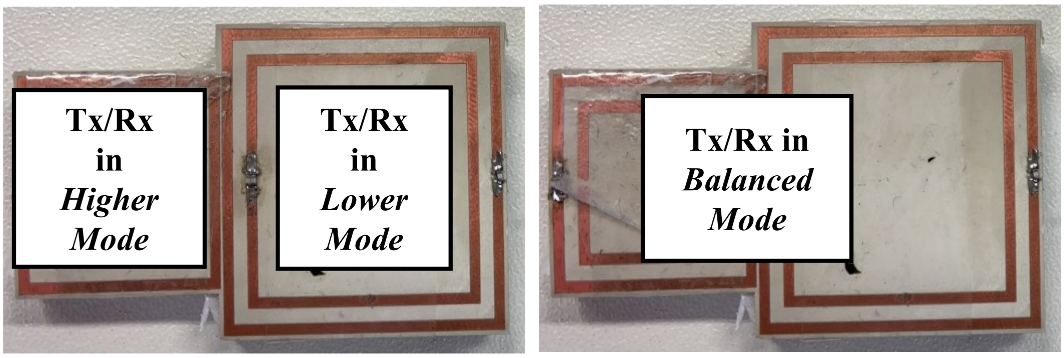

(b)

Fig. 24 (a) Measurement setup. (b) Definition of three mode. The white boxes stand for the location of the Tx (Rx). When Tx/Rx put toward the 0-degree metasurface, the whole system will be in lower mode and verse sersa.

Both the transmitter (Tx) and the receiver (Rx) have dimensions of 15 mm × 15 mm. The inner circle diameter of the Tx (Rx) (S_2) is 8 mm, while the outer circle diameter (S_2) is 12 mm. The metasurfaces have sizes of 28.8 mm × 28.8 mm for the 180-degree metasurface and 20 mm × 20 mm for the 0-degree metasurface. Rogers 3003 substrate material is used for both metasurfaces. The width of the copper traces (W_{copper}) on the metasurfaces is 1 mm. There is a spacing of 1.5 mm between two rings on the metasurfaces. The gaps for etching capacitors on all devices have a width of 0.5 mm.

On the 180-degree metasurface shown in Fig. 20, the capacitors ($C_{lin1,2,3,4,5,6}$) with values of 0.3 pF, 0.3 pF, 0.3 pF, 0.3 pF, 0.2 pF, and 0.2 pF are etched on the inner rings of the SRR. Conversely, on the 0-degree metasurface shown in Fig. 2b, the capacitors ($C_{hout1,2,3,4,5,6}$) with values of 0.2 pF, 0.2 pF, 0.2 pF, 0.1 pF, 0.1 pF, and 0.1 pF are etched on the outer rings of the SRR.

Therefore, the electromagnetic (EM) simulation results presented in Fig. 23 and

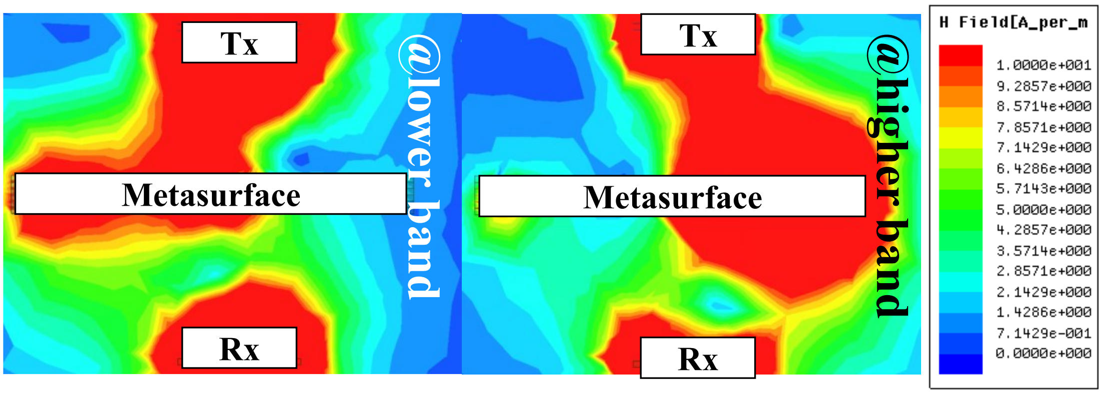

Fig. 25 confirm our theory, demonstrating a substantial enhancement in the magnetic field directed towards the z-direction for both bands. This concurrent and separate enforcement of the magnetic field in the z-direction leads to a significant improvement in performance on both bands, providing strong validation for our theoretical claims.

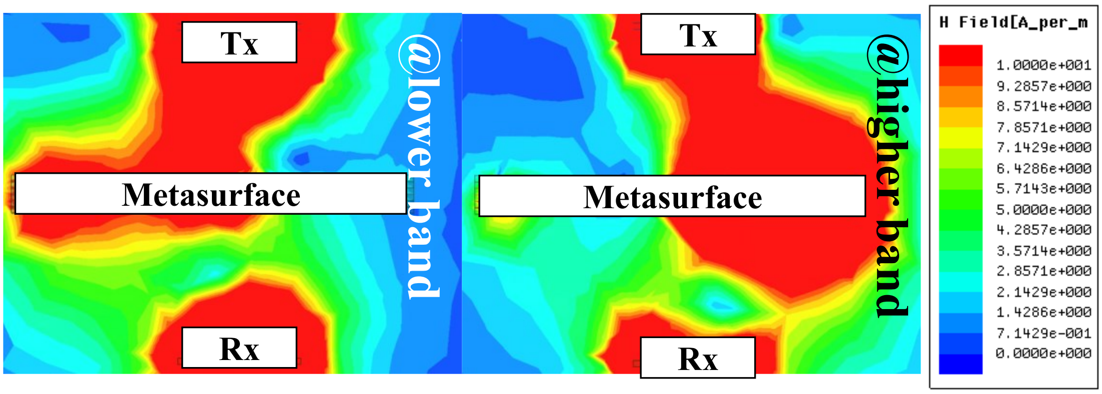

Fig. 25 EM simulation at lower and higher band, respectively, when WPT distance = 40 mm.

4.3 Experiment and Analysis

4.3.1 Measurement Setup

Fig. 24 (a) depicts the experimental setup of the dual-band WPT system incorporating the proposed metasurface. The unique topology of the metasurface gives rise to three distinct working modes, as illustrated in Fig. 24 (b), based on the intersection area. When the 180-degree metasurface covers a larger portion between the Tx and Rx, it leads to an increase in efficiency at the higher band, referred to as the higher mode. Conversely, when the metasurface is positioned at the center of the WPT system, the enhancement effect is evenly distributed on both bands, resulting in a balanced mode.

Furthermore, in order to provide more robust and convincing measurements of the power transfer efficiency, we have employed two different methods, which are detailed in the subsequent subsections.

4.3.2 Experiment Setup – using A PNA Network Analyzer

The measurement of the proposed WPT system's S-parameter was conducted using a network analyzer (PNA series: part #N5222A by Keysight Technologies). Foams and tapes were used solely for the purpose of securing the entire system, with minimal impact on its overall performance. Additionally, in order to address any errors that may have occurred during the manufacturing and soldering processes of the capacitors, the effective frequency of the metasurface was not precisely aligned with the resonance frequency of the entire system. Air gaps were intentionally left and filled with foams between each cell of the metasurface. This was done to account for variations in the mutual impedance of each element due to the size of the gaps, which can result in changes to the matrix Z in :

$$\boldsymbol{Z} = \begin{bmatrix} \boldsymbol{Z_{Tx}} & \boldsymbol{M_{Tx,p}} & \boldsymbol{M_{Tx,Rx}} \\ \boldsymbol{M_{Tx,p}^{\mathrm{T}}} & \boldsymbol{Z_p} & \boldsymbol{M_{p,Rx}} \\ \boldsymbol{M_{Tx,Rx}^{\mathrm{T}}} & \boldsymbol{M_{p,Rx}^{\mathrm{T}}} & \boldsymbol{Z_{Rx}} \end{bmatrix} \tag{4.5}$$

4.3.3 Experiment Setup – using a Signal Generator and Analyzer

In order to analyze the proposed WPT system, we conducted experiments using a signal generator and a signal analyzer, as depicted in Fig. 8. The signal generator was connected to the Tx, while the signal analyzer was connected to the Rx. A constant input power of 0 dBm was applied during the measurements. Specifically, we measured the WPT efficiencies of the lower band in the lower mode and the higher band in the higher mode at a WPT distance of 32 mm.

The power received at the Rx was measured as -3.82 dBm at 400 MHz (lower mode) and -4.28 dBm at 754 MHz (higher mode) for a WPT distance of 32 mm. Considering the losses in the cable, which were measured as -1.02 dBm at 400 MHz and -1.12 dBm at 754 MHz, the actual power transferred by the proposed WPT system was calculated as -2.80 dBm at 400 MHz in the lower mode and -3.16 dBm at 754 MHz in the higher mode. This corresponds to WPT efficiencies of 52% and 48%, respectively.

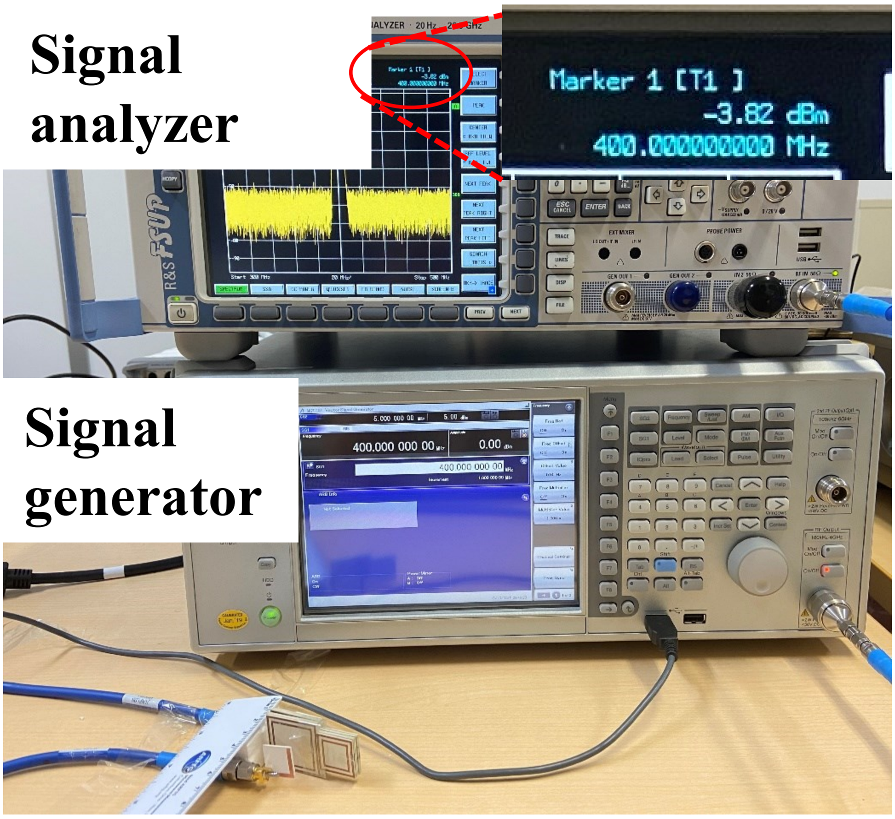

(a)

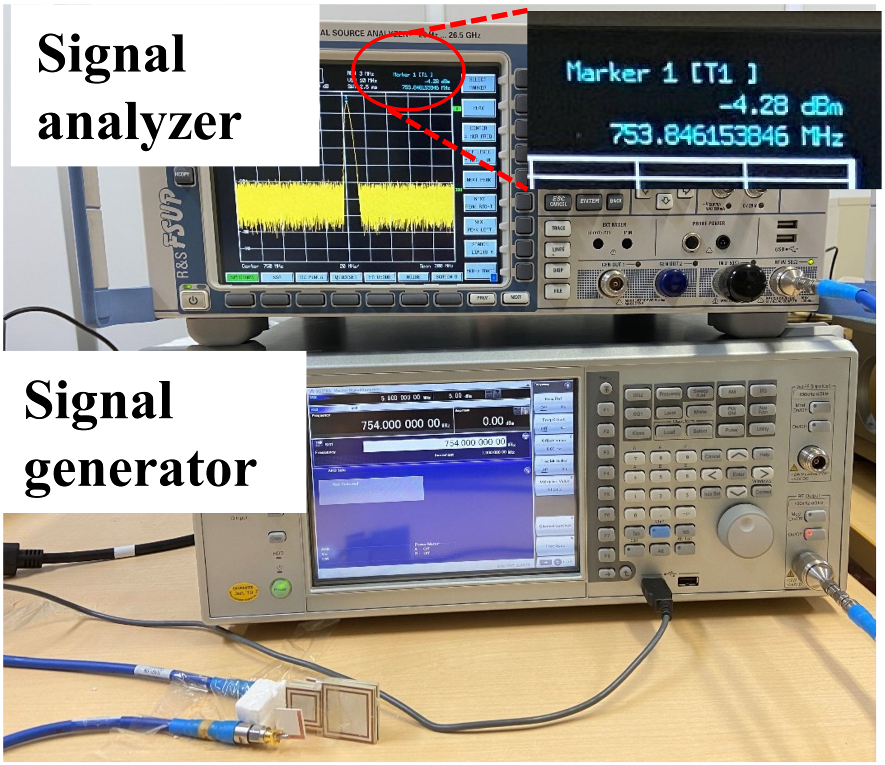

(b)

Fig. 26 Experiment setup using a signal generator and analyzer, and the results of WPT efficiencies (a) in the lower band and (b) in the higher band in the WPT distance of 32 mm

It is worth noting that these measured WPT efficiencies are slightly lower compared to the ones obtained using the PNA Network Analyzer, which were measured as 54% at 398 MHz and 50.2% at 767 MHz. This difference can be attributed to the peak frequency shift and losses caused by the SMA connectors. It is important to mention that the PNA Network Analyzer is capable of compensating for these losses through calibration prior to the measurement setup.

4.3.4 Measured Results

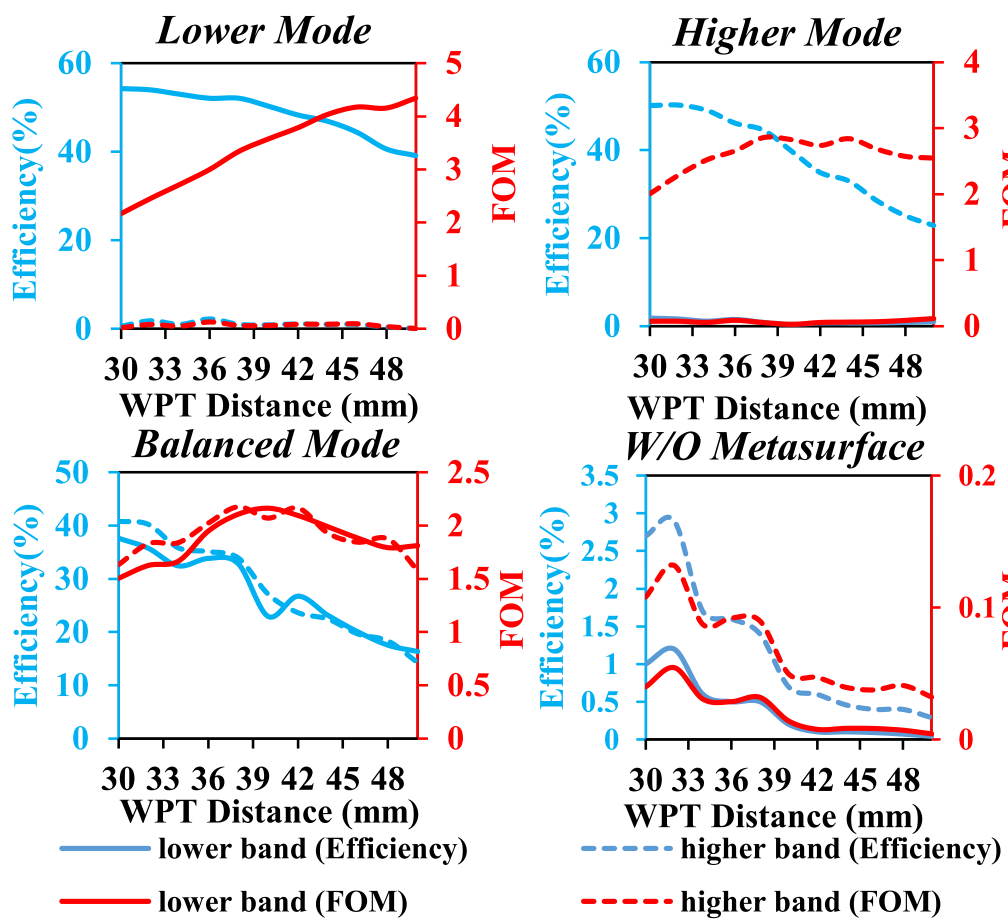

Fig. 27 WPT efficiency (blue line) and FOM (red line) at lower band (solid line) and higher band (dash line) in different modes and without metasurface (W/O Metasurface).

Fig. 27 illustrates the experimental and simulation results of the WPT efficiency. In the lower mode, the WPT efficiency reaches 39.1% at the lower band for a distance of 50 mm. In the higher mode, the WPT efficiency is 33.0% at the higher band for a distance of 44 mm. In the balanced mode, the WPT efficiencies are 26.7% at the lower band and 27.6% at the higher band for a WPT distance of 42 mm.

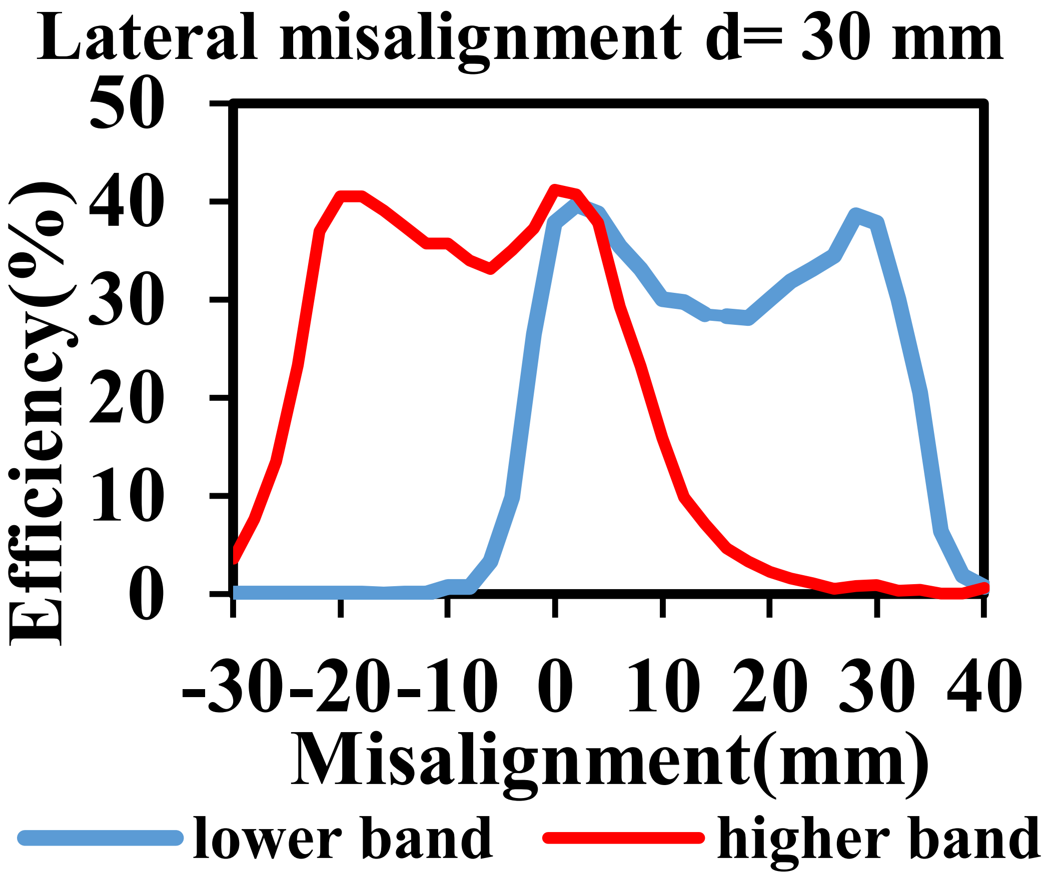

Fig. 28 Lateral misalignment from -30 mm to 40 mm at the WPT distance of 30 mm.

Furthermore, the lateral misalignment performance at a distance of 30 mm is shown in Fig. 28. Due to the impedance mismatching problem [31] that occurs when the Tx is horizontally moved, the efficiency on both bands initially decreases, then increases, and finally decreases again. These measured results highlight the need for further improvements in impedance matching in the metasurface, which will be investigated using machine learning techniques in the near future. Moreover, the performance of this WPT system using metasurface can be evaluated using a figure of merit (FoM) [2], as described by:

$$FOM = \frac{\eta_{peak} \times d^2}{A_{Rx}{}^{\frac{2}{3}} A_{Tx}{}^{\frac{1}{3}}} \tag{4.6}$$

Here, d represents the WPT distance, and A_Tx and A_Rx denote the areas of the Tx and Rx, respectively. Based on the FoM, TABLE 2 indicates a significant improvement on both bands in the balanced mode compared to previous state-of-the-art approaches. Additionally, in the lower mode, the WPT performance at the lower band surpasses that of previous works [17].

TABLE 2 Performance Comparison with State-of-art Designs

WPT	Area of Tx/Rx (mm²)	Operation	Metasurface	Distance (mm)(Maximum performance)	η	FoM
[15]	150×150	Single band	without	200	10.7%	0.190
			with		54.9%	0.976
[17]	390×390/130×130	Dual band	without	200	26.9%/16.8%	0.213/0.133
			with		42.38%/24.5%	0.336/0.194
[43]	290×290×π	Single band	without	875	69.40%	2.01
This work	15×15	Dual band	without	15	50.4%/51.5%	0.504/0.515
			balanced mode	42	26.7%/27.6%	2.09/2.16
			lower mode	50	39.1%/0.09%	4.34/0.01
			higher mode	44	0.7%/33.0%	0.06/2.83

4.4 Conclusion

To enhance the performance of the proposed dual-band WPT system, a novel multi-mode self-resonance-enhanced wideband metasurface has been developed. This metasurface is designed to be compact and suitable for use in compact devices like IMDs by overlapping DGS resonators to prevent interference between bands. For each band, two types of metasurfaces are proposed: 180-degree and 0-degree metasurfaces. These metasurfaces have self-resonance at their respective bands in the WPT system. By combining these two metasurfaces, a multi-mode metasurface is formed. To address the cross-polarization issue that arises from the combination of the metasurfaces, the directions of each metasurface are readjusted.

The proposed metasurface has shown significant improvements in the WPT efficiency. In the best-case scenario, the WPT efficiency is enhanced up to 39.2%, a remarkable improvement compared to the mere 0.04% efficiency without the metasurface. The balanced mode metasurface effectively improves the WPT efficiency on both bands simultaneously.

Additionally, the proposed metasurfaces demonstrate equal effectiveness in improving lateral misalignment, following a similar trend. These impressive performances result in a figure of merit (FoM) above 2 for the proposed WPT system in all cases, surpassing the performance of state-of-the-art systems, as illustrated in TABLE 2.

5 Hybrid SRRs-based Metamaterial

The lateral misalignment performance of the proposed WPT system is affected by its horizontal topology [44]. This alignment issue results in unstable performance, making it challenging to maintain optimal performance on both bands [44]. In order to address this misalignment problem, we have introduced modifications to the stacked metamaterial [19], [44]–[46] and enhanced its tolerance to lateral misalignment.

5.1 Better Miniaturization: Hybrid SRRs

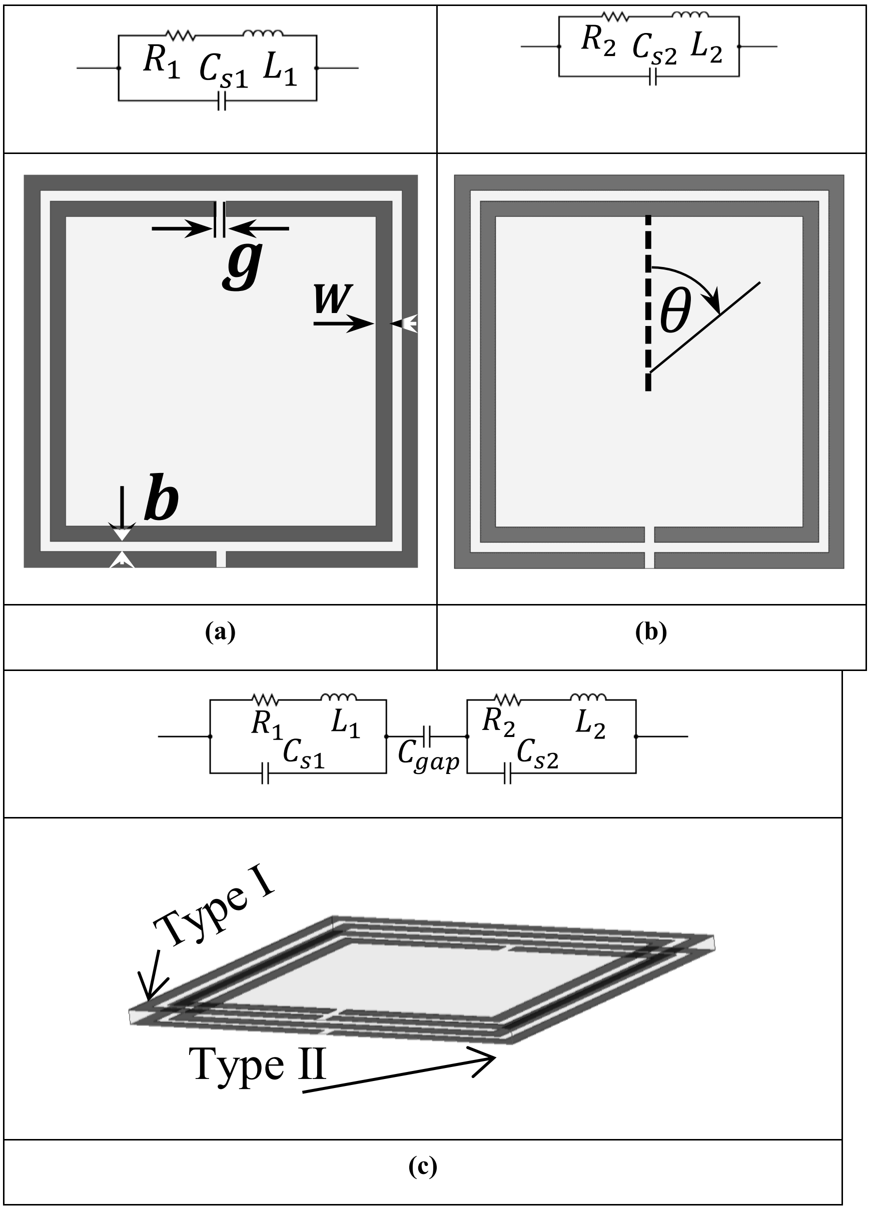

Fig. 29 Structure and equivalent circuits for hybrid SRR: (a) Type I, (b) Type II, and (c) Type I and Type II.

TABLE 3 Dimension (in mm) of Proposed Metamaterial

Notation	Description	Value
a	Length and width of metamaterial	20
$\boldsymbol{b}$	Distance between two rings	0.5
$\boldsymbol{C_{s1}}$	Capacitor on Type I	0.2pF
$\boldsymbol{C_{s2}}$	Capacitor on Type II	0.1pF
$\boldsymbol{g}$	Gap length	0.5
$\boldsymbol{W}$	Height of copper	0.75

In this section, we propose a wideband metamaterial using a hybrid split-ring resonator (SRR), as shown in Fig. 29. The optimized dimension are listed in TABLE 3. Two types of SRRs are employed for each band, respectively. To determine the resonance frequencies of the entire structure, we start by selecting the frequencies of interest. For each individual SRR, the resonance frequency can be estimated using the following equations[39], [47]:

$$\omega_{1,2} = \frac{1}{2\pi\sqrt{2a_{ave}L_{1,2}\frac{(\pi+k)^2-\theta_{1,2}^2}{2(\pi+k)}C_{pul}}} \tag{5.1}$$

Here,

$$\begin{aligned} a_{ave} &= a - \frac{g}{8} \\ k &= \frac{C_{s1,s2}}{a_{ave}C_{pul}} \\ C_{pul} &= \frac{C_o + C_e}{2} \end{aligned} \tag{5.2}$$

Where a is the length and width of SRRs, g is the gap length. C_0, C_e are the odd and even mode of the average capacitance per length, respectively. The resonance frequency ($\omega_{1,2}$) of Type I ($\theta_1 = 0$) and Type II ($\theta_2 = \pi$) SRRs varies due to the different positions of the gaps for the etched capacitors. These resonance frequencies can be estimated using equations (5.1) and (5.2) [39], [47].

5.2 Polarization Analysis

When considering the stacking of these two types of unit cells alternately, it is crucial to take into account the polarizability of the resulting structure. Due to the distinct resonance frequencies exhibited by each unit cell, the magnetic polarizabilities, denoted as α_{zz}^{mm} , also exhibit variation. This distinction in polarizabilities arises from the different resonant behavior and the response of the unit cells at their respective frequencies. The magnetic polarizabilities α_{zz}^{mm} can be mathematically described by (5.3) [48], providing a quantitative understanding of the polarizability differences between the two unit cells when stacked in this alternating configuration.

$$\alpha_{zz}^{mm} = \alpha_0 \left(\frac{\omega_0^2}{\omega^2} - 1 \right)^{-1}, \alpha_0 = \frac{d^2}{L_{1,2}} \tag{5.3}$$

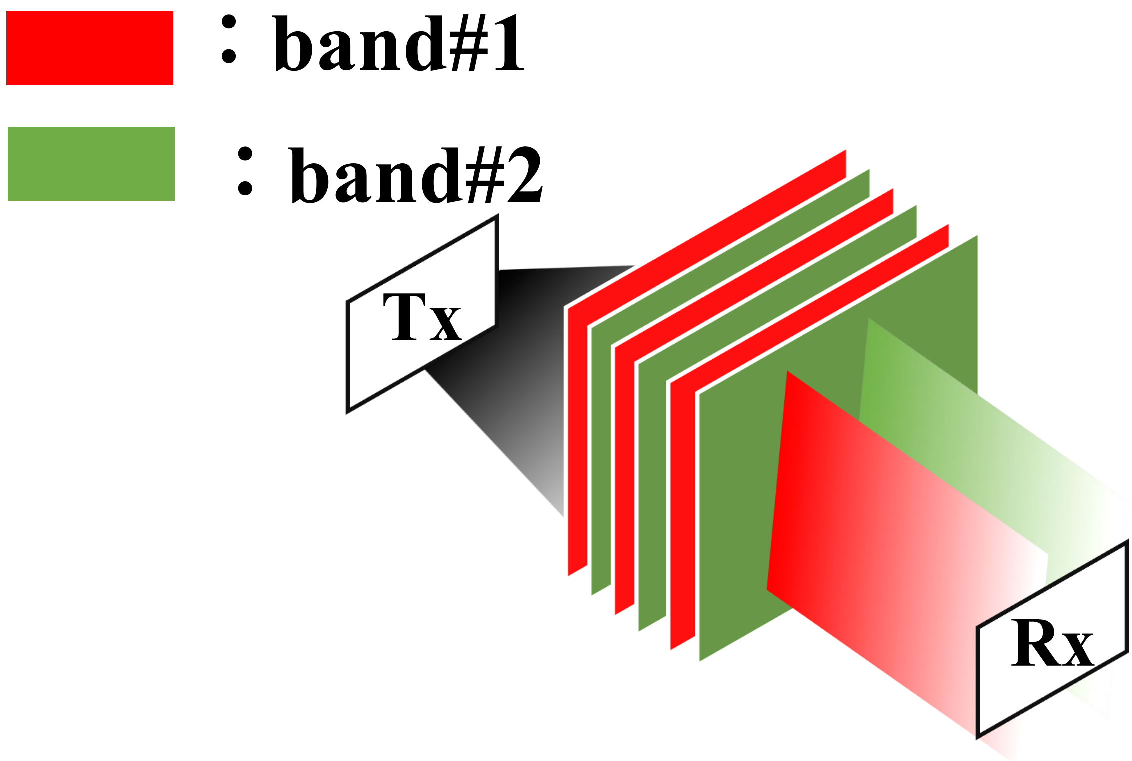

Fig. 30 Illustration of the polarizability differences between two-unit cells in different frequencies.

5.3 Simulation Results

The simulation was carried out using the ANSYS High-Frequency Structure Simulator (HFSS). The simulation setup is depicted in Fig. 31, illustrating the configuration used for the metamaterial analysis. By analyzing the S-parameter of the unit cell (Type I + II), it is observed that the proposed metamaterial exhibits three distinct resonance frequencies. Additionally, the permeability of the metamaterial is estimated through S-parameter extraction techniques [19], as depicted in Fig. 32. The permeability plot demonstrates three parallel resonance frequencies.

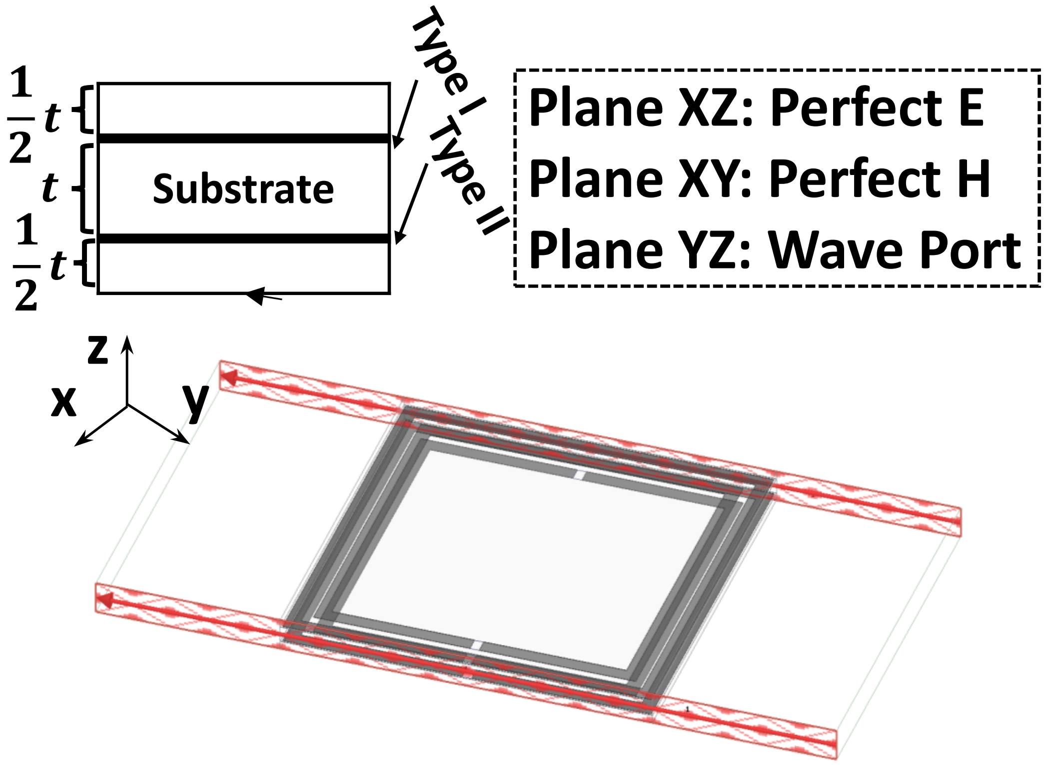

Fig. 31 Configuration of the unit cell for the simulation. t is the thickness of the substrate.

It is important to note that the frequency bands, specifically the first and second parallel resonance frequencies, intersect the line of zero permeability. Consequently, the optimized design of the metamaterial places the lower frequency band of the proposed WPT system between the first parallel resonance and the series resonance (where negative permeability is present). On the other hand, the higher passband frequency of the WPT system is positioned within the region of near-zero permeability. Therefore, an electromagnetic simulation is conducted to validate the theoretical findings and further investigate the performance of the proposed metamaterial.

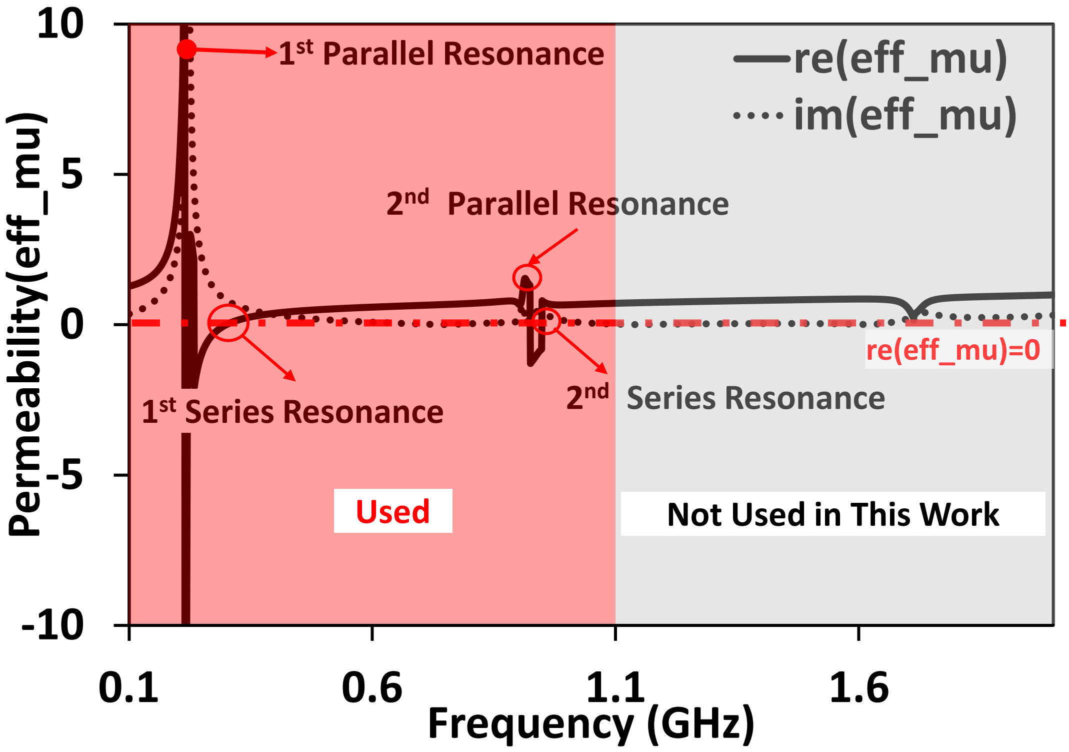

Fig. 32 Simulated effective permeability of proposed metamaterial. Region in red is utilized in this work.

Fig. 33 presents the simulated magnetic vector plot of the proposed WPT system. Specifically, Fig. 33 (a) and (c) illustrate the magnetic vector distribution without the implementation of the metamaterial at both bands, respectively. Conversely, Fig. 33 (b) and (d) demonstrate the magnetic vector distribution with the presence of the proposed metamaterial. In the absence of the metamaterial, the magnetic wave beams become dispersed as they propagate toward the Rx, resulting in a decrease in power transfer efficiencies (PTEs). This can be observed in Fig. 33 (a) and (c).

However, when the proposed metamaterial is employed, as shown in Fig. 33 (b) and (d), the magnetic wave beams are effectively directed towards the Rx at specific resonant frequencies. At the resonant frequency of 391 MHz (with a phase of approximately 110 degrees) and the resonant frequency of 750 MHz (with a phase of approximately 20 degrees), the magnetic wave beams are focused toward the Rx. This focusing effect, which occurs at different resonant frequencies and phases, aligns with the multi-mode theory and the polarization theory, respectively. The simulation results provide further evidence of the effectiveness of the proposed metamaterial in enhancing the power transfer efficiency of the WPT system.

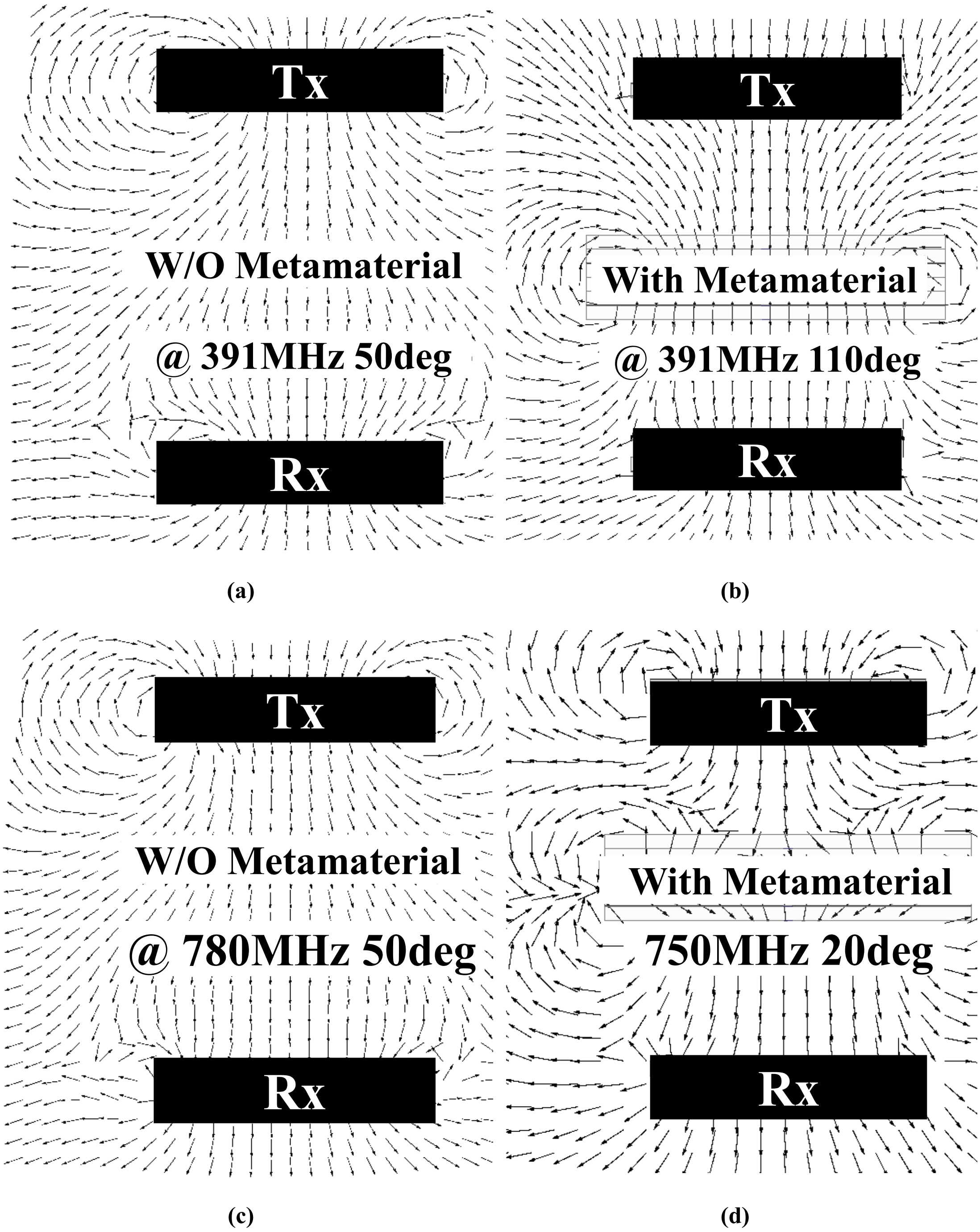

Fig. 33 Simulated magnetic vector plot of the proposed WPT system without (left side) and with (right side) the proposed metamaterial at (a), (b) the lower band, and (c), (d) the higher band.

5.4 Experiment and Analysis

5.4.1 Experiment Setup

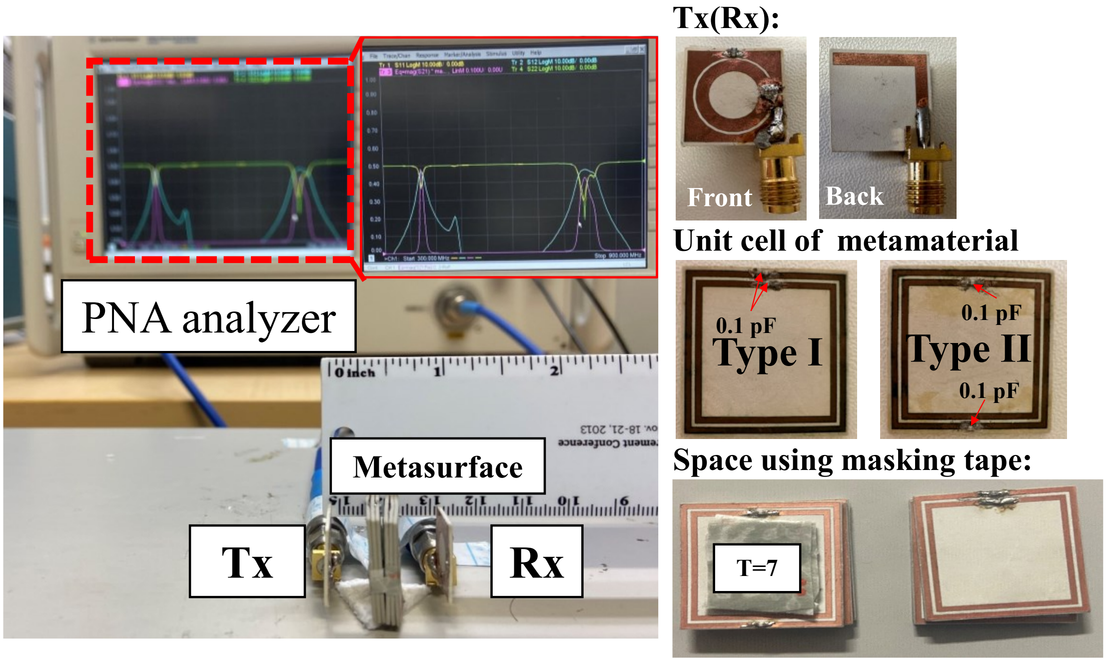

Fig. 34 Experiment setup and details of each component. We used masking tape to control the gap between each cell.

In the experimental setup, a network analyzer (PNA series: part #N5222A by Keysight Technologies) was used for the measurement of the proposed system. The fabricated system utilized a Rogers 3003 substrate with a thickness of 0.762 mm and a dielectric constant of 3 (with a loss tangent of 0.001). The substrate was coated with a 17-um thick layer of copper.

Fig. 12 illustrates the experimental setup, where both the Tx and Rx sizes were 15 mm × 15 mm. During the experiment, some differences and uncertainties were encountered compared to the simulation configuration. Firstly, it was challenging to precisely eliminate the space between each layer (represented as th_{gap} in the equation). Secondly, the loss of the capacitors used in the experiment contributed to the self-resonant frequency of the proposed metamaterial. These uncertainties made it more difficult to achieve accurate and optimal results.

To address these challenges, a solution was implemented by using masking tape with different layer numbers (T) to control the distance between each cell. Consequently, the thickness of the gap (th_{gap}) could be estimated as the product of the tape thickness (th_{tape}) and the layer number (T), as indicated in :

$$th_{gap} = th_{tape} \times T = 0.98\, mm \tag{5.4}$$

By quantitatively controlling the mutual inductance between each split-ring resonator (SRR) through the adjustment of $\boldsymbol{T}$, optimization of the system performance could be achieved [31], [44]. This approach helped to mitigate the uncertainties arising from the fabrication process and enhance the repeatability and reliability of the experimental results.

5.4.2 Measurement Results – Power Transfer Efficiency

Fig. 35 illustrates the power transfer efficiency (PTE) at different WPT distances for various scenarios. In addition to the proposed hybrid metamaterial, separate experiments were conducted with metamaterials consisting of only Type I and only Type II unit cells for comparison purposes.

The results demonstrate that the PTEs for both bands are improved with the inclusion of the proposed hybrid metamaterial. This confirms the effectiveness of the hybrid design in enhancing power transfer efficiency.

Furthermore, an interesting observation is made when the WPT distance is below 20 mm. In this range, the PTE at the lower band increases as the distance between the metamaterial and the Tx extends. This phenomenon is attributed to the occurrence of over-coupling. When the metamaterial is positioned too close to the Tx (or Rx), an excessive coupling effect takes place, leading to decreased efficiency. However, as the distance between the metamaterial and the Tx increases, the level of over-coupling diminishes, resulting in an improvement in PTE.

This anomalous behavior highlights the importance of properly managing the coupling between the metamaterial and the transmitter/receiver to optimize power transfer efficiency. The findings emphasize the need to carefully design the system parameters and ensure appropriate spacing between components to achieve the desired performance.

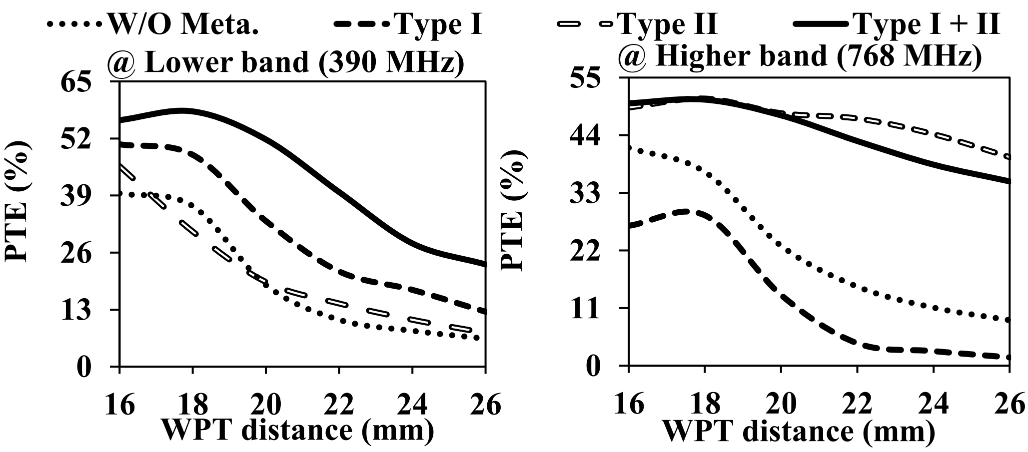

Fig. 35 PTE of the system in the cases: Without metamaterial (W/O Meta.), With metamaterial that only uses Type I (Type I), With metamaterial that only uses Type II (Type II), and With metamaterial that uses Type I and Type II (Type I + II).

On the other hand, it was observed that at the higher band, the power transfer efficiency (PTE) using Type II metamaterial alone was higher than that achieved with the hybrid metamaterial. This can be attributed to the fact that the metamaterial consisting of only Type II unit cells has a smaller number of layers (3-unit cells) compared to the six-layer stacked hybrid metamaterial. As a result, the substrate loss in the Type II metamaterial configuration is lower.

Furthermore, it was noticed that the higher band is more sensitive to the gap distance (th_gap) between the metamaterial cells compared to the lower band. This sensitivity arises from the strong relationship between the coupling factor (k') and the resonant frequency itself.

These observations indicate that the performance of the WPT system is influenced by various factors, such as the number of unit cells, substrate loss, and gap distance. Careful consideration and optimization of these parameters are necessary to achieve the desired power transfer efficiency on both bands.

5.4.3 Measurement Results – Lateral Misalignment

In the additional experiment conducted to evaluate the lateral misalignment performance, the Rx was moved vertically while maintaining the same WPT distance of 23 mm. This experiment aimed to investigate the effect of lateral misalignment on the performance of the WPT system, considering the presence or absence of the metamaterial.

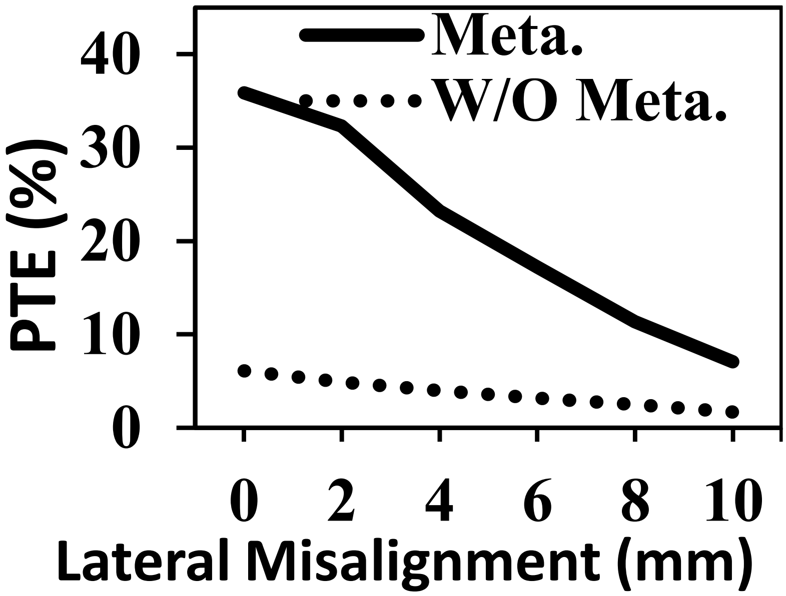

(a)

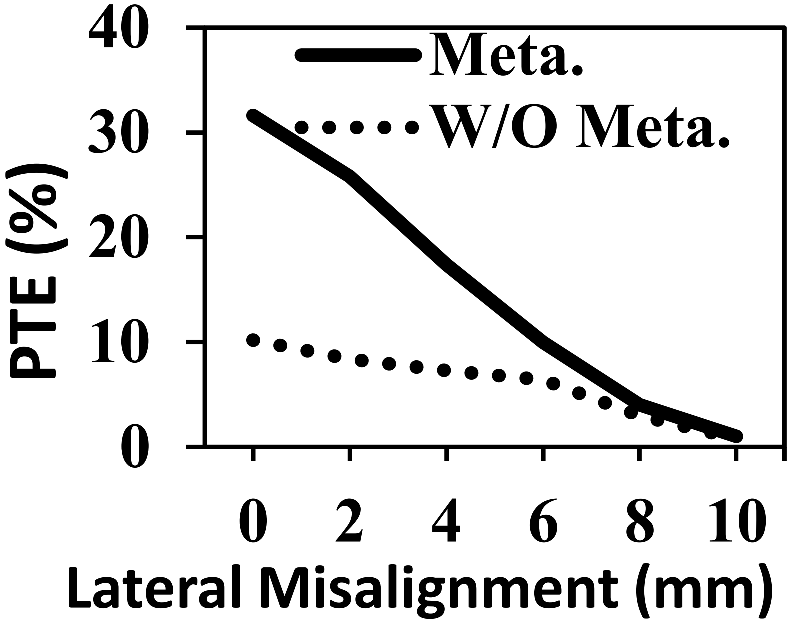

(b)

Fig. 36 Comparison of PTE at various lateral misalignment distances with and without the proposed metamaterial (W/O Meta.). (a) at the lower band at 390 MHz, and (b) at the higher band at 768 MHz. The WPT distance is 23 mm.

TABLE 4 Performance Comparison with State-of-art Designs

WPT	Area of Tx/Rx mm²	Operation	Metamaterial Without/With	Distance (mm)	η	FOM (Lower band/ Higher band)	Misalignment PTE ($\widehat{d_x} = 0.13$)	Misalignment Improvement Rate** ($\widehat{d_x} = 0.13$)
[15]	150×150	Single Band	With	200	54.90%	0.97		
[17]*	Coils on Tx: 86×86×π Coils on Rx: 48×48×π	Dual Band	Without	200	26.9%/16.8%	≤1.0/0.62	26.2%/16.5%	1.03/0.56
			With		42.38%/24.5%	≤ 1.58/0.93	53.2%/25.7%	
[37]	21×21	Single Band	With	30	66.5%	1.36		
[49]	250×250×π	Single Band	With	600	68.5%	1.25		
[50]	Tx: 140×140 Rx: 170×170	Dual Band	Without	150	67.07%/64.53%	0.59/0.57		
This work	15×15	Dual Band	Without	20	18.6%/22.9%	0.33/0.41	6.1%/8.4%	4.30/2.07
			With		51.8%/47.8%	0.92/0.85	32.3%/25.8%	

* [17] didn't mention the actual size of the Tx and Rx, so we used the size of the coils etched on Tx and Rx, respectively instead and they are supposed to be much smaller than the actual sizes (Tx and Rx).

**Misalignment Improvement rate = $(\eta_{with}-\eta_{wo})/\eta_{wo}$. $\eta_{with,wo}$ is the PTE with and without the help of the proposed metamaterial.

Fig. 36 presents the comparison results between the cases with metamaterial (Meta.) and without metamaterial (W/O Meta.). It can be observed that the inclusion of the metamaterial significantly improves the lateral misalignment performance. The metamaterial helps to mitigate the adverse effects of lateral misalignment, resulting in enhanced power transfer efficiency even when the Rx is not perfectly aligned with the Tx.

These findings demonstrate the effectiveness of the proposed metamaterial in improving not only the overall WPT efficiency but also the system's tolerance to lateral misalignment, which is crucial for practical applications where precise alignment may not always be achievable.

TABLE 4 indicates the performance comparison with the state-of-the-art. To fairly compare the lateral misalignment (d_x) performance with the help of different metamaterials in the former works, a normalized lateral misalignment distance is used [10], [38], [51]:

$$\widehat{d_x} = \frac{d_x}{\sqrt[4]{A_{Rx}A_{Tx}}} \tag{6.5}$$

5.5 Conclusion

The proposed wideband stacked metamaterial, utilizing a hybrid split-ring resonator (SRR) configuration, has been introduced to enhance the performance of the dual-band WPT system. By incorporating non-uniform capacitors within each unit cell, the system achieves improved performance within the frequency range of interest.

The analysis begins by examining two types of metamaterials, Type I and Type II, which are shown to individually enhance power transfer efficiencies (PTEs) at their respective bands. These metamaterials exploit the different permeabilities associated with each type, resulting in improved performance within specific frequency ranges. Subsequently, the Type I and Type II metamaterials are combined by stacking them alternately, creating a hybrid SRR metamaterial structure.

Simulation results based on the S-parameter and permeability demonstrate that the hybrid SRR metamaterial exhibits three resonant modes. Additionally, due to the different polarizations associated with each resonance frequency, the metamaterial effectively reduces cross-polarization at each band. Consequently, enhancement is achieved at each targeted frequency of interest.

To validate the theory and simulation, the complete system, including the metamaterial, is fabricated, and experiments are conducted. The measured efficiencies show significant improvements, with the PTE increasing from 18.6% to 51.8% at the lower band and from 22.9% to 47.8% at the higher band, specifically at a distance of 20 mm. This substantial enhancement translates to an improved Figure of Merit (FOM) as well, increasing from 0.33 to 0.92 at the lower band and from 0.41 to 0.85 at the higher band.

Furthermore, the proposed metamaterial also demonstrates enhanced performance in terms of lateral misalignment. It improves lateral misalignment tolerance equally well at both bands, outperforming a previous approach [44]. This increased robustness and improved performance highlight the effectiveness of the proposed wideband stacked metamaterial for dual-band WPT systems.

6 Metamaterial-Inspired Absorber for Dual-band SWIPT System

6.1 Simultaneous Wireless Information and Power Transfer

In the pursuit of miniaturization, [6], [28] introduced a SWIPT system that incorporates frequency-shift keying (FSK) modulation. However, these systems require careful optimization of the capacitors in over-coupled resonators to achieve optimal power and signal transfer performance. In the case of biomedical applications, [6] suggests the use of capacitive switching, while [28] proposes resistive switching within implanted devices. Both approaches require an additional direct current (DC) source, which introduces potential risks to the human body [29]. Moreover, the data transmission method employed in [6], [28] leads to a significant reduction in power transfer efficiency (PTE), causing instability and significantly lengthening the battery charging time.

In contrast, [11] presents a novel MIMO dual-band SWIPT system utilizing co-existing defected ground structure (DGS) resonators. Apart from evaluating PTE, [11] also focuses on assessing the isolation performance between the power and signal channels. The power band demonstrates satisfactory isolation, effectively segregating the power and signal channels to minimize interference. However, the signal transmission in the signal band, especially for low-power signals, experiences degradation due to interference from offset frequencies.

While [11] addresses the challenges related to isolation performance, it is important to note that the studies by [6], [28] highlight concerns regarding system miniaturization, capacitor optimization, the inclusion of additional DC sources, potential risks to the human body, decreased PTE, instability, and prolonged battery charging time. Further research and development are required to overcome these limitations and enhance the overall performance and efficiency of SWIPT systems in biomedical applications.

6.2 Absorber for Isolation Performance

Metamaterial-based structures have gained significant attention in the field of far-field applications, such as MIMO antennas [52], meta-antennas [53], and so on [54], [55]. However, there is limited research on metamaterial-based absorbers specifically designed for inductive-coupling (near-field) systems. This section introduces a novel approach to develop a metamaterial-inspired absorber for inductive-coupling SWIPT systems.

The proposed approach is based on the theory of composite right/left-handed transmission lines (CRLH-TL). By leveraging this theory, a physical model is established to design the metamaterial-based absorber. The model is then validated through electromagnetic (EM) simulations, ensuring its accuracy and feasibility.

This innovative concept opens up new possibilities for enhancing the performance and efficiency of inductive-coupling SWIPT systems. By incorporating metamaterial-inspired absorbers, it is anticipated that the isolation between the power and signal channels can be effectively improved, thereby minimizing interference and optimizing system performance.

Further research and experimentation are required to fully explore the potential of this metamaterial-inspired absorber in the inductive-coupling SWIPT system. The development of such absorbers has the potential to contribute significantly to the advancement of near-field wireless power transfer technologies.

6.3 Metamaterial-inspired Absorber

6.3.1 Configuration of the Absorber

In order to address the need for improved isolation performance in the higher frequency band of a MIMO WPT system using inductive coupling, a novel approach is proposed in this study. Drawing inspiration from the periodic structure of metamaterials, the design incorporates SRRs in a symmetrical configuration between two ports, as illustrated in Fig. 37.

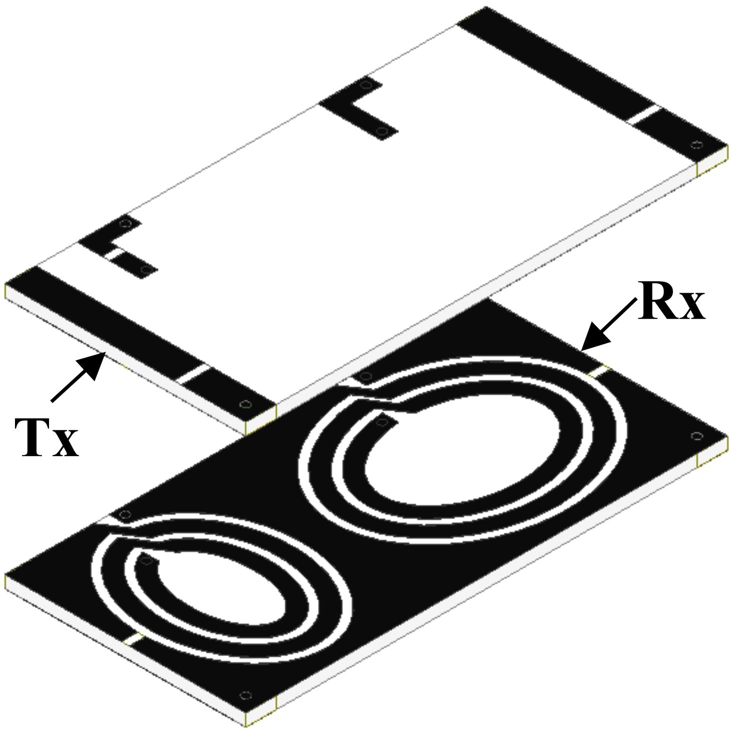

(a)

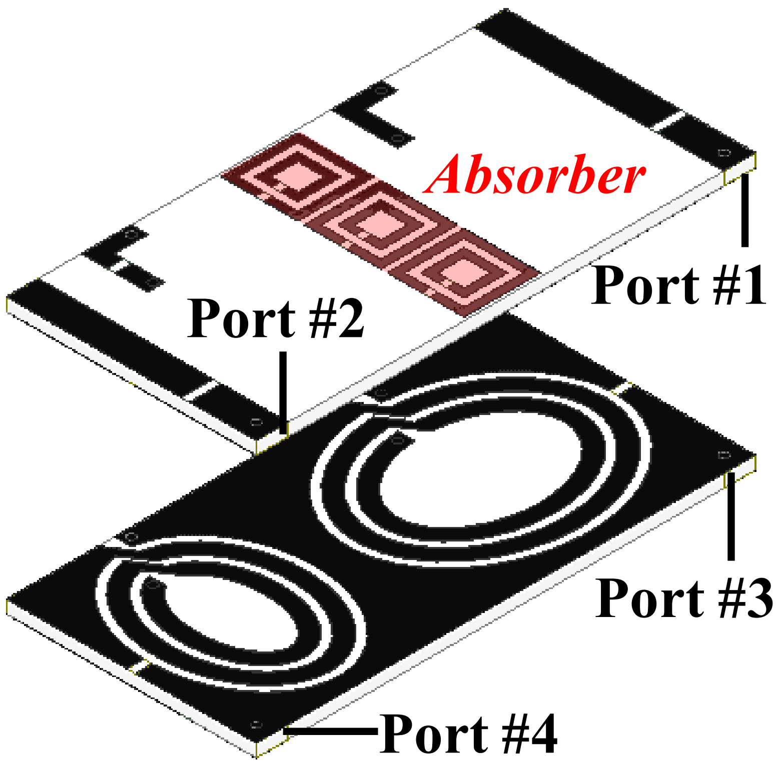

(b)

Fig. 37 . Layout of MIMO WPT system. (a) Conventional one in [11], (b) Using SRRs-based absorber. The dimensions of both (Tx) and (Rx) are consistent in both cases. Ports 1 and 3 are designated for power transfer at the lower band, while the remaining ports are used for data transmission at the higher band.

The incorporation of SRRs in this symmetrical arrangement aims to enhance the isolation between the ports in the higher frequency band. The periodic nature of the metamaterial structure allows for effective control and manipulation of the electromagnetic waves, enabling improved isolation performance.

By strategically positioning the SRRs and optimizing their parameters, the proposed configuration aims to mitigate interference and crosstalk between the ports, resulting in enhanced isolation in the higher frequency band. This is crucial for ensuring reliable and efficient signal transmission, particularly for signals with higher frequencies.

Further analysis, simulation, and experimental validation will be conducted to assess the performance and feasibility of the proposed metamaterial-based configuration. The goal is to achieve the desired isolation levels in the higher frequency band, thereby advancing the capabilities of MIMO WPT systems using inductive coupling [11].

6.4 Absorption Performance

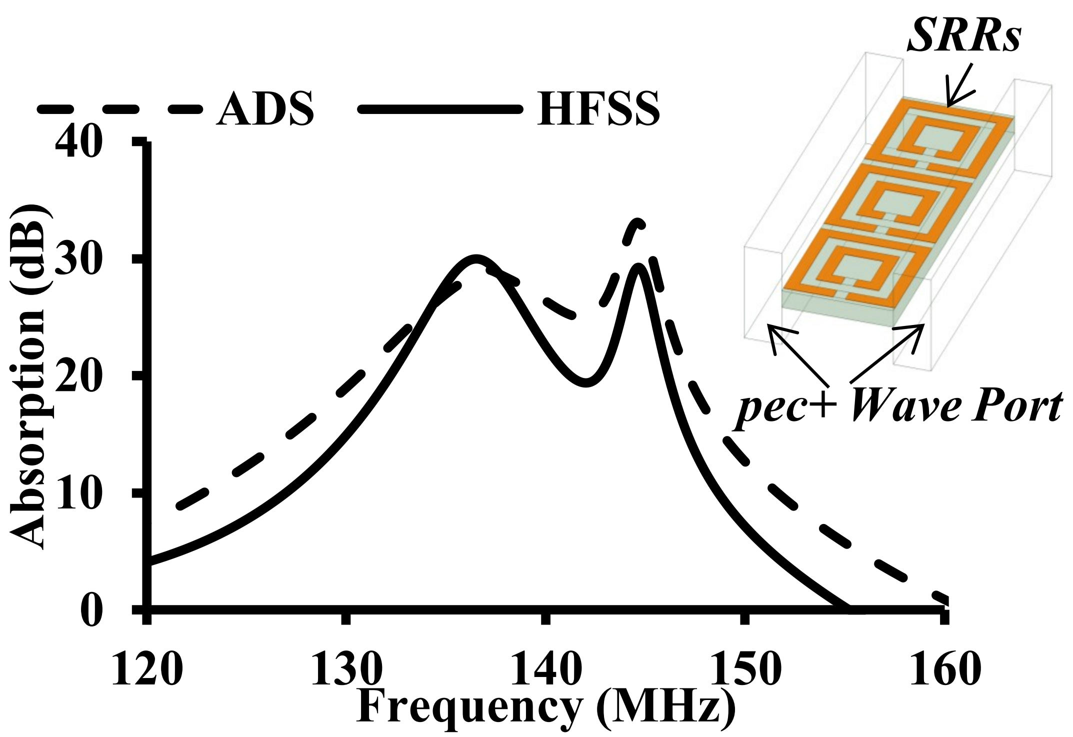

Fig. 38. HFSS configuration and simulated absorption performance using ADS and HFSS, respectively.

Fig. 38 depicts the estimated absorption performance ($A=1-|S_{11}|^2-|S_{21}|^2$) utilizing both Advanced Design System (ADS) and High-Frequency Simulation Software (HFSS).

Also, the HFSS simulation configuration is outlined, incorporating wave ports and perfect electrical conductors (pec) to match the surroundings.

6.5 Dielectric Characteristics

6.5.1 CRLH-TL-Based Model

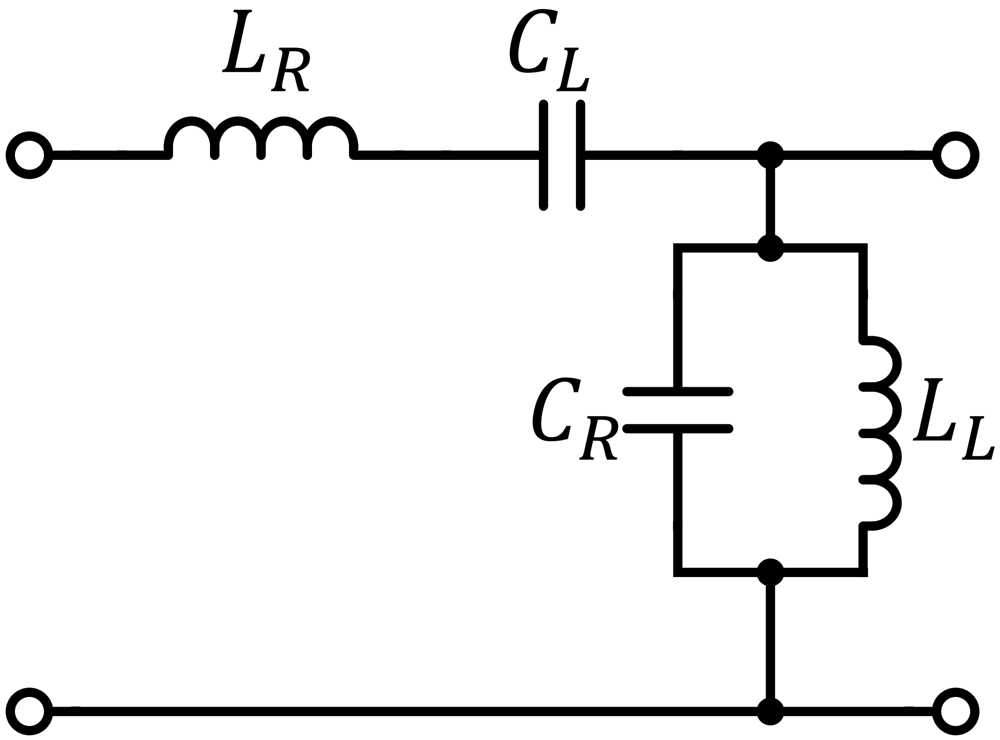

Fig. 39 Equivalent circuit (per length) of the metamaterial's unit cell.

In the context of nonreciprocal metamaterials, which are used to regulate antenna polarization and mitigate interference in MIMO antennas, the characteristics of the proposed metamaterial are influenced by various factors such as capacitance, inductance, parasite capacitance, and mutual inductance between each cell. Due to these factors, it is not physically possible to realize a pure left-hand transmission line (LH TL). [56].

As depicted in Fig. 39, the characteristics of the proposed metamaterial are influenced by the capacitance (C_L) and inductance of the line (L_L), as well as the contributions of parasite capacitance (C_R) and mutual inductance (L_R).

Thus, the nonreciprocal metamaterial demonstrates two resonance frequencies, specifically the series resonance frequency (ω_{se}) and shunt resonance frequency (ω_{sh}), and its characteristic impedance can be determined [56], [57]:

$$Z_c = \sqrt{\frac{L'_L}{C'_L}} \times \sqrt{\frac{\left(\frac{\omega}{\omega_{se}}\right)^2 - 1}{\left(\frac{\omega}{\omega_{sh}}\right)^2 - 1}} \tag{6.1}$$

Consequently, as $\omega_{se}\rightarrow\infty$ and $\omega_{sh}\rightarrow 0$, the entire circuit is coming open, thereby preventing the propagation of waves from Port 2 to Port 1. Consequently, the wave's energy is consumed and stored within the SRRs, resulting in a reduction of PTE to the Rx. Until the circuit is open, no magnetic wave exists in the Tx, which precludes propagation from the Tx to the Rx. Thus, a trade-off between isolation and PTE should be carefully considered.

Alternatively, the permeability of the metamaterial ($\mu(\omega)$) can be determined by mapping Maxwell's equations and telegrapher's equations [56]:

$$\mu(\omega) = L'_R - \frac{1}{\omega^2 C'_L} \tag{6.2}$$

Given the trade-off between isolation and PTE, the resonance frequency of the proposed wireless power transfer system (ω_0) is anticipated to be greater than the frequency at which the permeability's real part is minimized. Conversely, when the real part of permeability equals zero, the SRRs become shorted, facilitating the smooth propagation of waves from Port 2 to Port 1.

Therefore, the real part of permeability at ω_0 is expected to be non-zero, ensuring that the SRRs do not become shorted and maintaining the desired isolation and PTE.

6.5.2 Permeability Estimation and Analysis

The layout of the proposed metamaterial is shown in Fig. 39. The dimensions used for the metamaterial are specified in **Error! Reference source not found.**. The m etamaterial components, including the Tx and Rx, are fabricated by printing 17-μm-thick copper on a RO3003 substrate. The RO3003 substrate has a dielectric constant of 3, a loss tangent of 0.001, and a thickness of 0.762 mm.

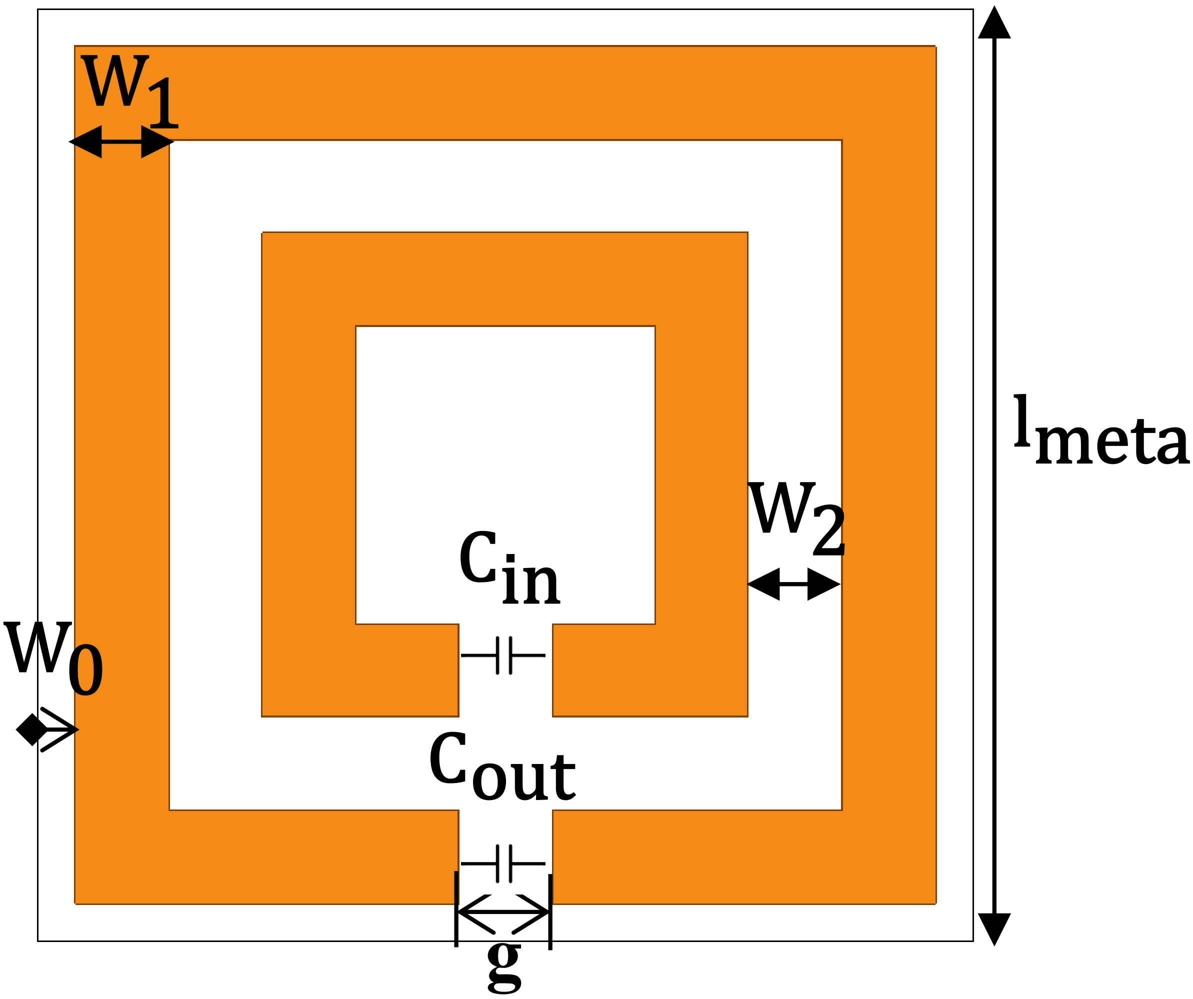

Fig. 40 Layout of the unit cell . $C_{in,\ out}$ stand for the capacitors etched on each gap.

TABLE 5 Dimension (in MM) of Unit Cells of Proposed Metamaterial

C_{in}	C_{out}	g	l_{meta}	W_0	W_1	W_2
150 pF	180 pF	0.5	5	0.2	0.5	0.5

Based on the analysis presented in Section IIA, specifically equations (2) and (3), Fig. 41 provides a visual representation of the feasible region where the effective permeability (μ_{eff}) of the proposed metamaterial lies within an acceptable range. This region serves as a guideline for optimizing the design of the SRRs in order to achieve efficient power transfer at the desired WPT frequency of the higher band. By ensuring that the effective permeability falls within this region, losses due to improper permeability values can be minimized, resulting in improved overall system performance.

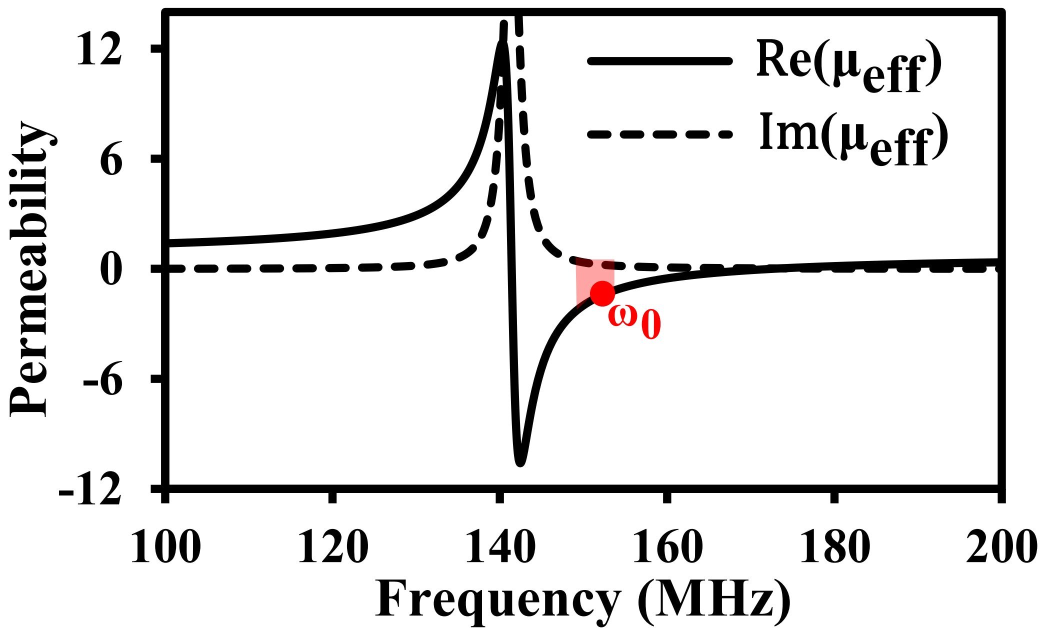

Fig. 41 Estimated effective permeability (μ_{eff}) of the proposed metamaterial. WPT frequency of the higher band (ω_0) is 152 MHz, which is located within the feasible region shaded in red based on the analysis in Section IIA (2) and (3).

6.5.3 EM Simulation

Fig. 42 presents a comparison of the H-field in two scenarios: the original system (without the absorber) and the system with the optimized absorber. The frequencies of 151 MHz and 152 MHz are depicted for the original and absorber-embedded systems, respectively. As a result, the proposed absorber contributes to reduced H-field leakage from P2 to P1, leading to an improvement in isolation performance. As a result, because of the less leakage from P2 to P1, in the frequency of 152 MHz, less wave from P1 could reach P4. Consequently, the isolation performance ($|S_{1,4}|$) improves.

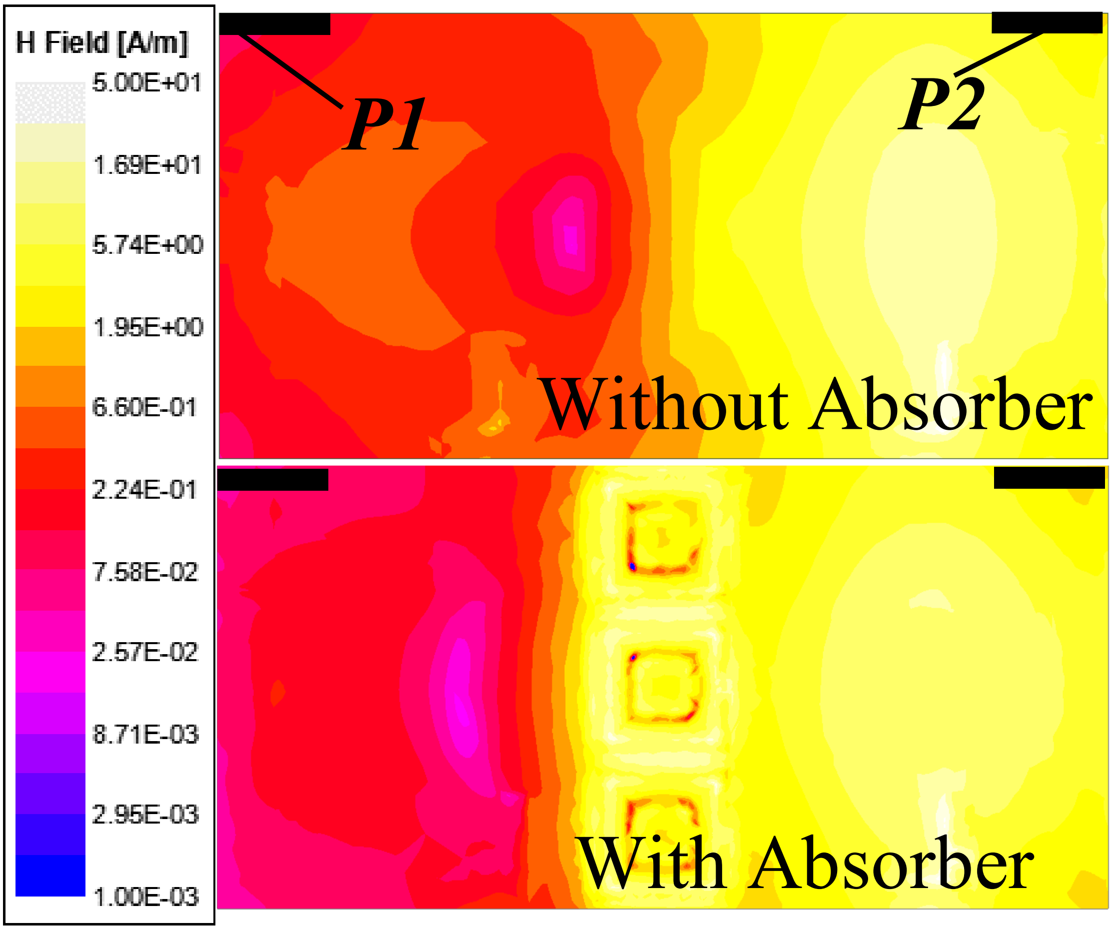

Fig. 42. H-field distribution of (a) original system and (b) system with absorber.

6.6 Results and Analysis

6.6.1 Experiment Setup: S-Parameter Measurement

Fig. 43 depicts the physical implementation of the fabricated MIMO WPT system, both without and with the inclusion of the nonreciprocal metamaterial-inspired absorber. To ensure a good impedance matching, a 50Ω terminator is connected to the disconnected port, as shown in Fig. 43 (b) and (c). The power transfer efficiency (S(1,3) and S(2,4)) as well as the isolation performance (S(1,4)) are measured using a PNA analyzer with the series number #N5222A.

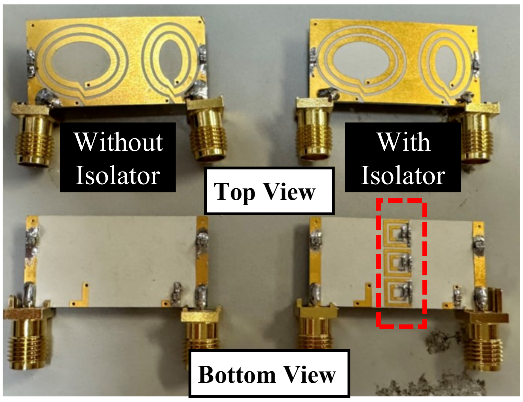

(a)

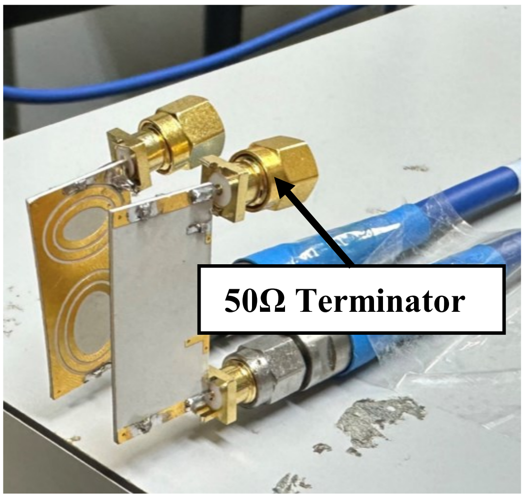

(b)

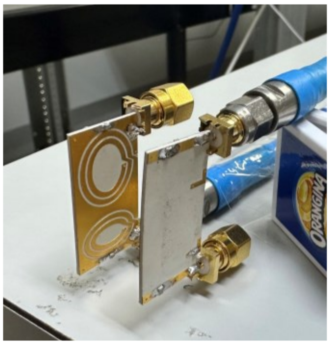

(c)

Fig. 43 Fabricated components and experiment setup for the S-parameter measurement in WPT distance of 15mm. (a) Fabricated Tx(Rx) without(with) absorber in top and bottom view, respectively. (b) PTE measurement setup. (c) Isolation performance measurement setup.

6.6.2 Results: S-Parameter

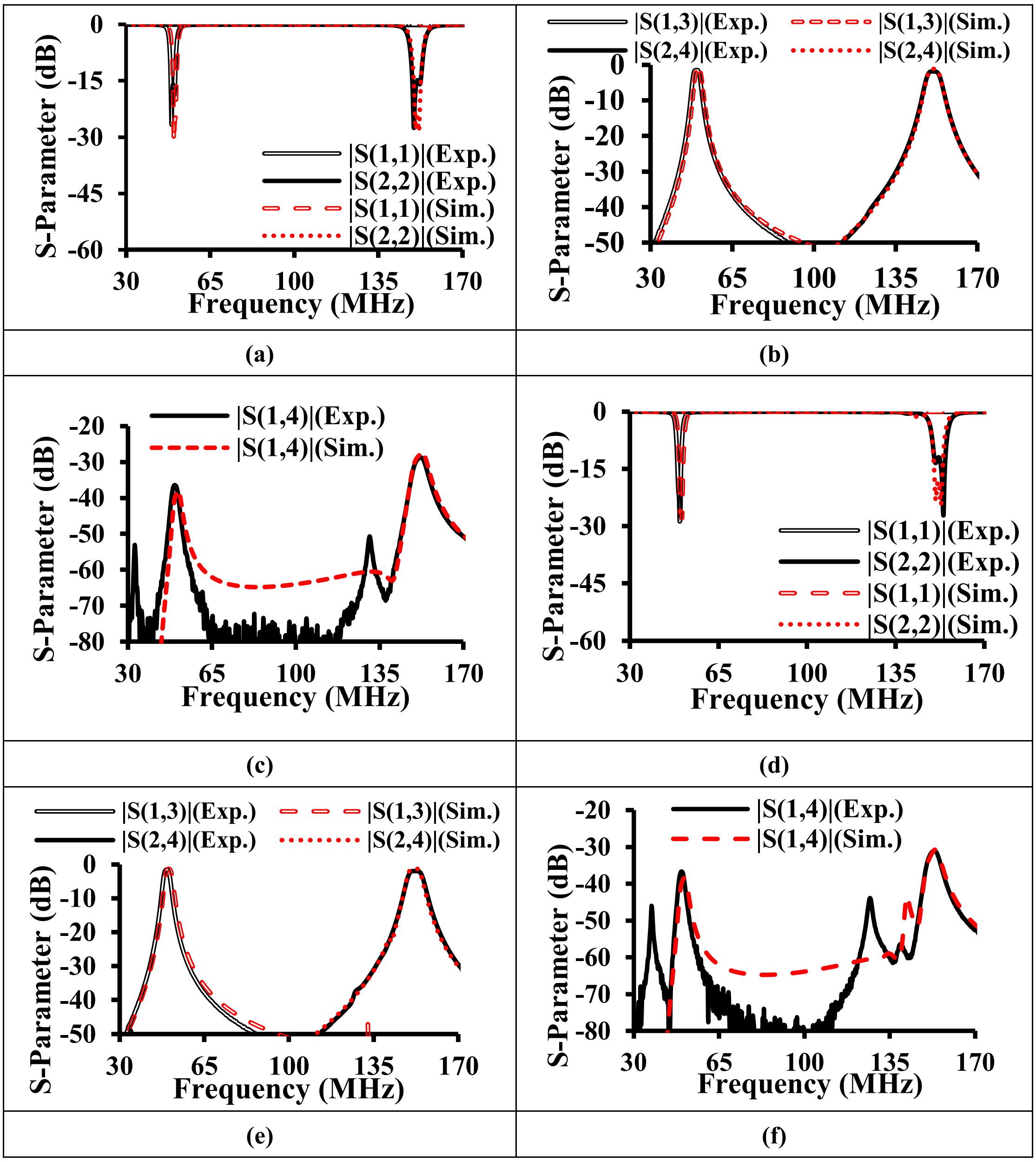

Fig. 44 .(a)-(c) are S-parameter of the system without metamaterial. (d)-(f) are S-parameter of the system with metamaterial.

The measured results, depicted in Fig. 44 (a)-(f), exhibit a strong agreement with the simulated results. Notably, the resonant frequency in the signal band experiences a slight shift (from 151 MHz to 152 MHz) when compared to the system without the metamaterial. This frequency shifting is attributed to the additional impedance introduced by the mutual inductance of the SRRs [20], [58]. The presence of the metamaterial induces changes in the system's impedance characteristics, resulting in the observed frequency shift.

6.6.3 Results: PTE and Isolation Performance

1) PTE Performance:

Based on the S-parameter ($S_{13,24}$) shown in Fig. 44 (b) and (e), the system's PTE η can be figured out by [19], [44], [59]:

$$\eta_{13,24} = \left|S_{13,24}\right|^2 \times 100\% \tag{6.3}$$

Here, $\eta_{12,34}$ presents the PTE in the power band (Port 1 and 3) and signal band (Port 2 and 4), respectively.

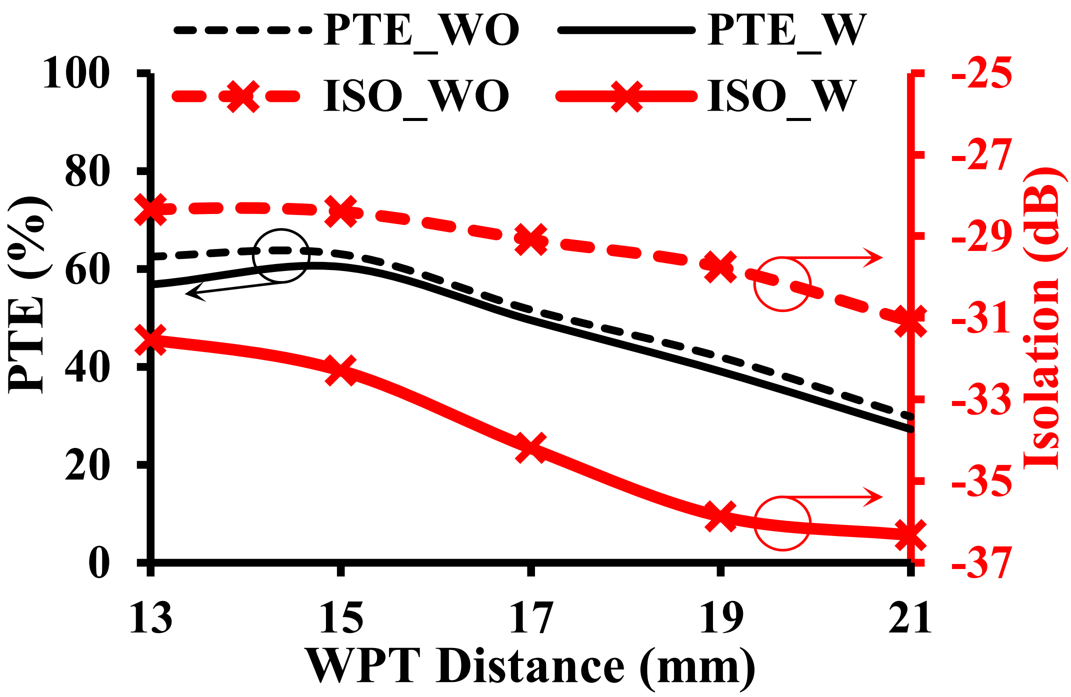

Fig. 45 Measured PTE (left) and Isolation (Right) performance varies with the WPT distance of the system without metamaterial (PTE_WO and ISO_WO, respectively) and with metamaterial (ISO _WO and ISO_WI, respectively), respectively. |S(1,4)| of the signal band is used for the isolation performance.

2) Isolation Performance:

The left side of Fig. 45 illustrates the measured power transfer efficiency of the system without and with the metamaterial. Due to the compact size of the SRRs (5 mm × 5 mm), large capacitors are used, which results in a low Q factor of the SRRs. Consequently, the power transfer efficiency decreases by approximately 2% compared to the system without the metamaterial. However, this decrease is considered acceptable given the benefits provided by the metamaterial in terms of isolation and overall system performance.

6.6.4 Experiment Setup: Phase Noise

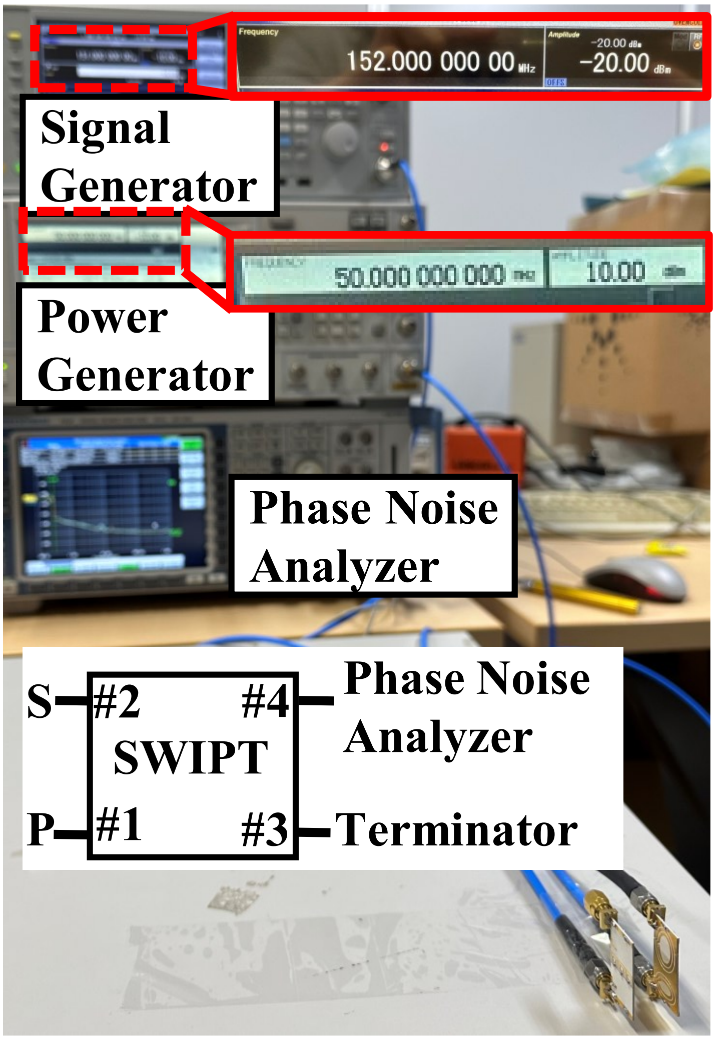

Fig. 46 Experiment setup and configuration for phase noise measurement in the WPT distance of 17 mm.

In the experiment, the phase noise of the received signal was measured. Fig. 46 illustrates the experimental setup and configuration. In the transmitter (Tx), two signal generators are connected to the signal and power bands of the system, respectively. In the receiver (Rx), a signal analyzer is connected to the signal band, while a 50Ω terminator is connected to the power band to improve impedance matching.

6.6.5 Result: Phase Noise

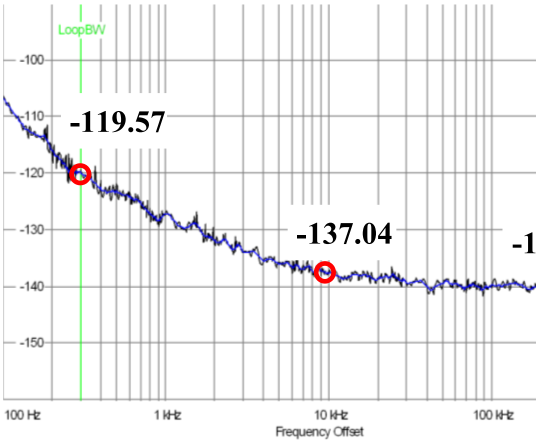

(a)

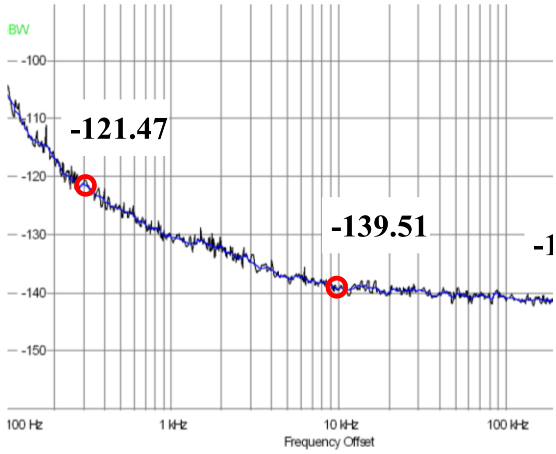

(b)

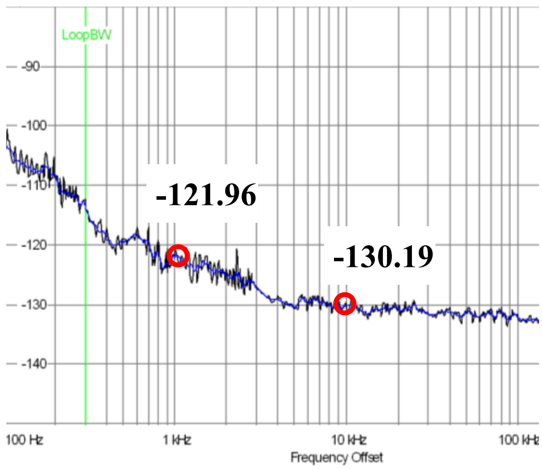

(c)

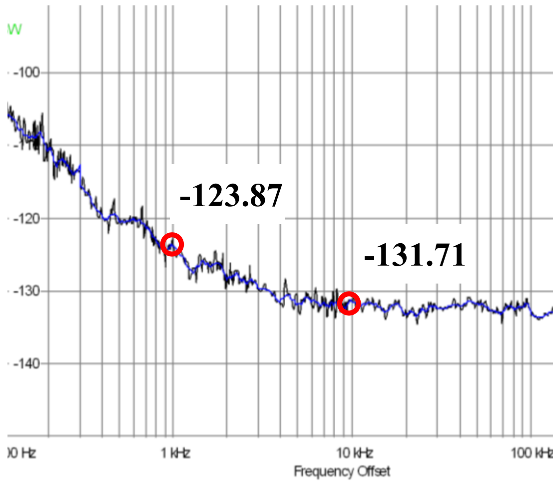

(d)

Fig. 47. Phase noise of the system in cases of (a), (c) without and (b), (d) with absorber when input power is (a)-(b) 10 dBm and -17 dBm, (c)-(d) 10 dBm and -19 dBm, in the power and signal port, respectively.

Fig. 47 (a)-(d) display the phase noise results obtained with different signal power inputs into the signal band, while keeping the input power in the power band constant at 10 dBm. The wireless power transfer (WPT) distance is 17 mm, allowing for more noticeable observations. The phase noise measurements were conducted until the input signal power reached -19 dBm, limited by the capacity of the signal analyzer.

With the presence of the absorber, the phase noise begins to decrease, particularly in the circled frequency offset, as the signal power weakens to -17 dBm and -19 dBm. As a result, a maximum degradation of 2.5 dBc/Hz and an average degradation of 2 dBc/Hz can be observed.

6.6.6 Experiment Setup: Data Rate in the Phantom Surroundings

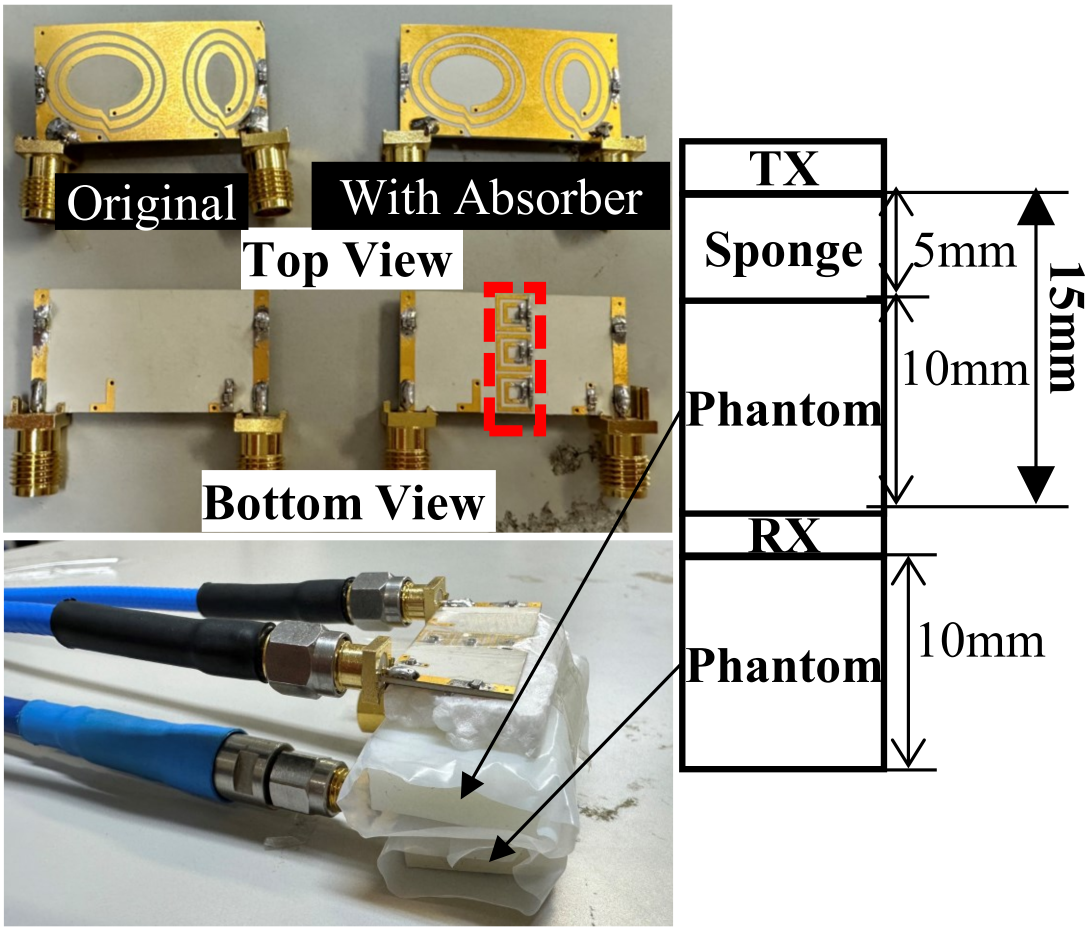

Fig. 48. Fabricated system and system setup using phantom for the experiment.

Illustrated in Figure 6, the initial systems (without an absorber) and the suggested systems (with an absorber) are constructed. Additionally, the Rx is inserted into two blocks of human body equivalent phantoms, each 10 mm thick (series number: X220171K01). To mitigate the over-coupling effect, an additional 5 mm thick sponge is positioned on top of the phantom, ensuring that the subsequent experiment is conducted at a WPT distance of 15 mm.

6.6.7 In Phantom: S-parameter

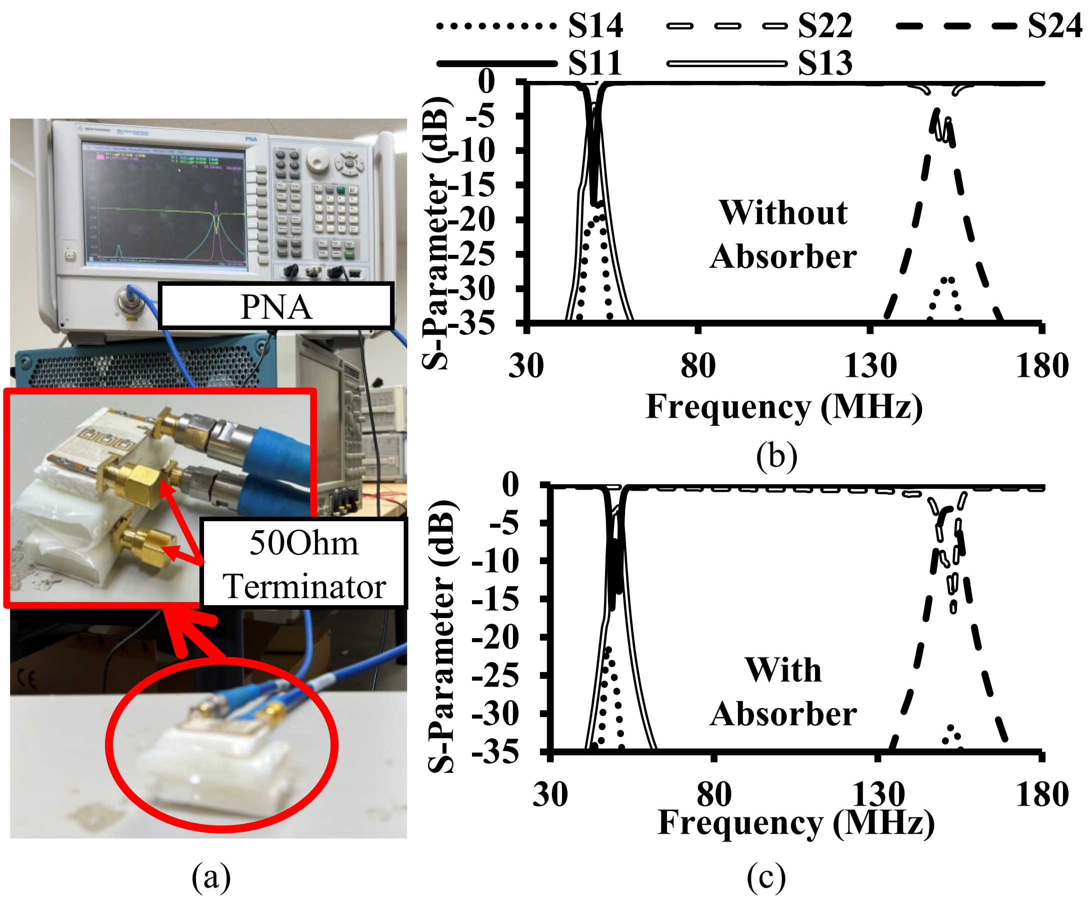

Fig. 49. (a) S-parameter measurement Setup. S-parameter results of (b) without absorber and (c) with absorber.

In Fig. 49, the S-parameters of the systems without an absorber and those with an absorber are illustrated, respectively. At a Wireless Power Transfer (WPT) distance of 15 mm, the proposed absorbers contribute to an improvement of approximately 3 dB in isolation performance, effectively reducing interference from P1. Meanwhile, the Power Transfer Efficiency (PTE) values for the original system (without absorber) and the proposed system (with absorber) are as follows: Original system—45.7% in the lower band (49.50 MHz) and 43.5% in the higher band (150.75 MHz); Proposed system—49.0% in the lower band (51 MHz) and 47.8% in the higher band (152.25 MHz), respectively.

6.6.8 Measurement: BER, Data Rate, and Signal Power

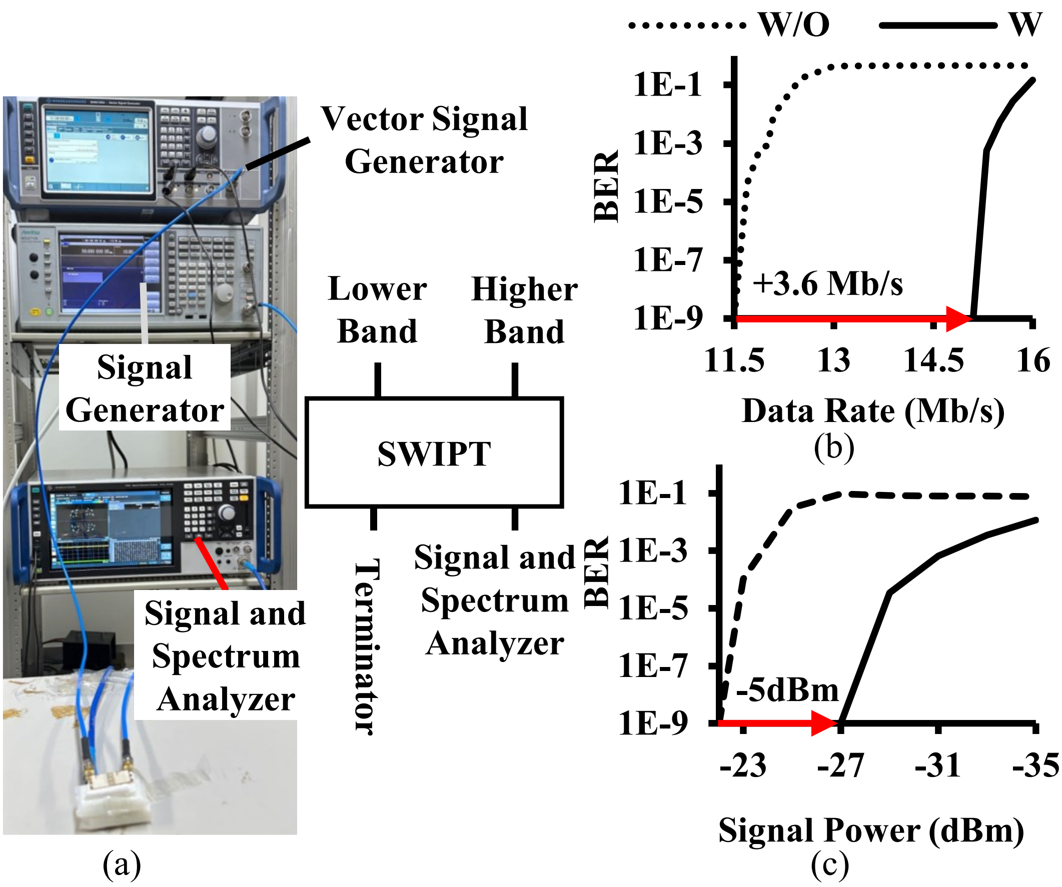

Fig. 50. (a) Experiment setup for BER measurement and comparison of BER with (b) data rate. (c) power of input signal. BER=10-9 with a confidence level of 99% when zero BER is observed.

In Fig. 50(a), the experimental setup for Bit Error Rate (BER) measurement is depicted. Two signal generators are utilized for the input of power and signal bands, respectively. The Tx's signal port generates and transmits a pseudorandom bitstream of PRBS-9 with minimum-shift keying (MSK) modulation. On the Rx side, the power transfer port is connected to a 50-ohm terminator, following the procedure from the previous experiment. Simultaneously, the signal port is linked to a signal and spectrum analyzer (series number: R&S FSVA3000). In Fig. 50(b), the outcomes of data rate and the measured BER on the Rx side are displayed. The proposed absorber significantly enhances the data rate by 3.6 Mb/s (from 11.5 Mb/s to 15.1 Mb/s).

Furthermore, Fig. 50 (c) demonstrates the BER variation concerning the input signal power from the Tx side. As a result, the proposed system enables stable communication with a weaker signal power (-5 dBm from -22 dBm to -27 dBm) compared to the original system.

TABLE 6 provides a comparison of performance with recently proposed works utilized for biomedical implants. Our proposed system exhibits significantly improved data rate performance in comparison to the systems presented in [6], [7].

TABLE 6. Performance comparison with recent proposed works.

Work	**Surroudings**	**Number of Ports**	**Frequency (MHz)**	**Size (mm^2)**	**WPT Distance (mm)**	**PTE (%)**	**Modulation**	**Data Rate (Mb/s)**
[6]	Air	2	30	30×30	42	80.1	L-RSK	5
[7]	Air	2	35	30×30	45	63-66	LSK	Up: 4/Dn:2
[38]*	Chicken	2	49	Tx: 20×20 Rx: 10×10	10	57	-	-
This work*	Phantom	4	50/152	15×30	15	49	MSK	Without Absorber: 11.5 With Absorber: 15.1

* WPT Only.

6.7 Conclusion

In conclusion, this Chapter presents a comprehensive study on the design and implementation of a novel nonreciprocal metamaterial-based absorber for compact near-field SWIPT systems. Through the utilization of CRLH TL theory, HFSS simulations, and EM analysis, the proposed absorber is carefully analyzed to achieve optimal isolation performance and minimal degradation in power transfer efficiency.

The theoretical analysis is validated through extensive EM simulations, which demonstrate good agreement with the theoretical predictions. Building upon these theoretical foundations, the absorber is fabricated and experimental measurements are conducted to evaluate its performance. The measured S-parameters and phase noise results confirm the effectiveness of the proposed absorber in achieving maximum isolation of -6 dB with less than 2% degradation in power transfer efficiency in the signal band. Furthermore, the phase noise measurements reveal a significant reduction of up to 2.5 dBc/Hz, particularly at low signal power levels in the signal band.

The contributions of this Chapter lie in the development of a nonreciprocal metamaterial-based absorber specifically tailored for compact SWIPT systems. The proposed absorber demonstrates excellent performance in terms of isolation and power transfer efficiency, while also addressing the important aspect of phase noise reduction. Moreover, this work contributes to the field by presenting the first reported phase noise measurements for near-field SWIPT systems.

The findings of this study pave the way for future advancements in the design of SWIPT systems, particularly in the near-field regime. The proposed absorber offers promising potential for enhancing the performance and reliability of compact SWIPT systems, making it a valuable contribution to the field of wireless power transfer. Further research can be conducted to explore additional optimizations and applications of the proposed absorber, opening up new avenues for the development of efficient and robust SWIPT systems.

7 Machine Learning-based Automatically Design System

7.1 Inverse Modeling for a DGS-Based WPT Design

WPT systems require high power transfer efficiency (PTE) to ensure optimal performance. Traditionally, additional matching circuits are proposed to achieve high PTE [60]. However, a promising alternative to this approach is the use of a defected ground structure (DGS), which eliminates the need for additional matching circuits [10], [20]. Despite the considerable PTE performance [8], optimizing PTE using DGS for various applications can be time-consuming and challenging. However, even the optimized lumped components (i.e., the value of the inductors and capacitors of the DGS-based equivalent circuits.) Regarding a higher frequency, because of the potential parasite capacitance and inductance, converting lumped components to the DGS and metamaterial's layouts still requires extensive simulation and dimension adjustment, which can be time-consuming and cumbersome [10], as shown in Fig. 60. Therefore, researchers and designers working on DGS-based WPT systems need a more efficient and convenient approach.

On the other hand, the simultaneous wireless information and power transfer (SWIPT) area has seen few attempts at optimizing the intrinsic PTE of coils [6], [61]. For example, while [6] proposed a novel system using capacitive switching for backscattering, their focus on over-coupling phenomenon analysis did not sufficiently address PTE optimization techniques for the coils, particularly in the case of over-coupling, which presents an unexplored opportunity for PTE improvement. Additionally, extra matching circuits implanted inside the human body can increase the size of the layout, making the DGS-based WPT a better option for miniaturization. As a result, the interdisciplinary obstacles that hinder the fusion of these techniques create a need for a simpler and more compressed model or method for non-DGS experts.

For this purpose, inverse modeling methods for planar microwave components, particularly those based on artificial neural networks (ANNs), are increasingly being developed [62]–[65]. However, to the best of the author's knowledge, very few studies have focused on predicting the geometrical layout of WPT systems [66], especially in their entirety.

Therefore, in the future, we will utilize machine learning to automatically optimize the layout of the metamaterial and DGS-based system.

7.2 Coupling Performance Analysis

Starting from a simple DGS-based WPT system shown in Fig. 4, since the dimensions of Tx and Rx are the same, what happens if the impedance matching of the entire WPT system is not properly optimized? This question must be addressed using Monte Carlo-based inverse optimization methods [67]. Since even if the WPT is symmetric, the parameters generated by a random generator may not exhibit perfect impedance matching, it is important to understand the consequences of suboptimal impedance matching in the WPT system.

7.2.1 Nyquist Plot Analysis

Starting from the J-inverter in (2.13) and (2.14), we could view the input admittance as a transfer function of the entire proposed WPT system, which 'controls' the input power voltage. The Nyquist plots of the input admittance as it varies with the frequency are shown in Fig. 51, demonstrating the WPT system's performance under different Y_3 admittances. Simulation results are obtained using an advanced design system (ADS).

In Fig. 51(a), it can be observed that when the input admittance is smaller than the load admittance ($Y_3 < R_s^{-1}$), three frequencies $\omega_{0,1,2}$ exist where the phase of the admittance is zero. However, because the real part of the admittance in ω_0 is smaller than that in $\omega_{1,2}$, the frequency point of ω_0 becomes unstable. Consequently, in the steady state, the resonant frequencies of the entire system would be located at two frequencies $\omega_{1,2}$ where the system 'admits' more power to be efficiently transferred.

On the other hand, as the input admittance becomes bigger, as shown in Fig. 51 (b), the PTE is optimized when $Y_3 = R_s^{-1}$. However, as $Y_3 > R_s^{-1}$, the admittance of the frequency point ω_0' , becomes bigger, 'admitting' more power to be transferred at ω_0', other than in the frequency point where admittance is R_s^{-1}. As a result, the PTE becomes smaller than with only one resonant frequency.

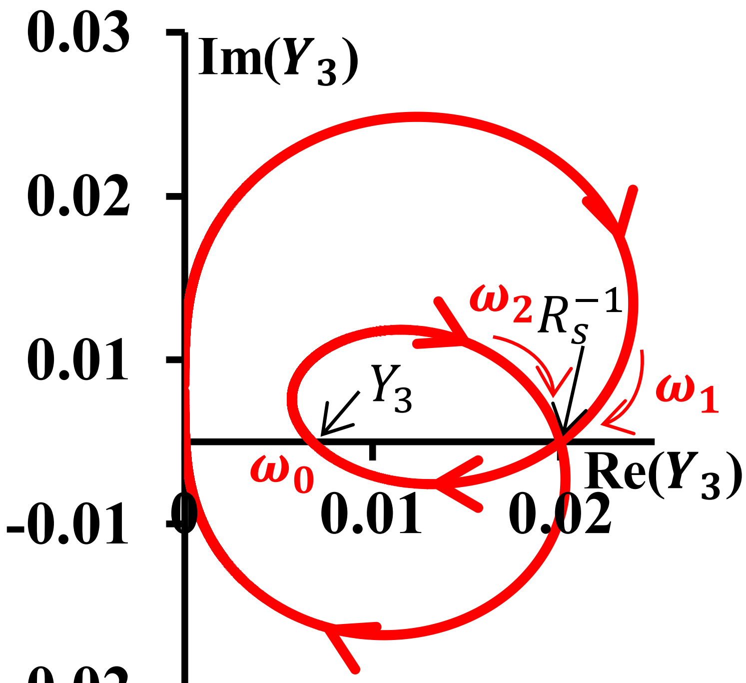

(a)

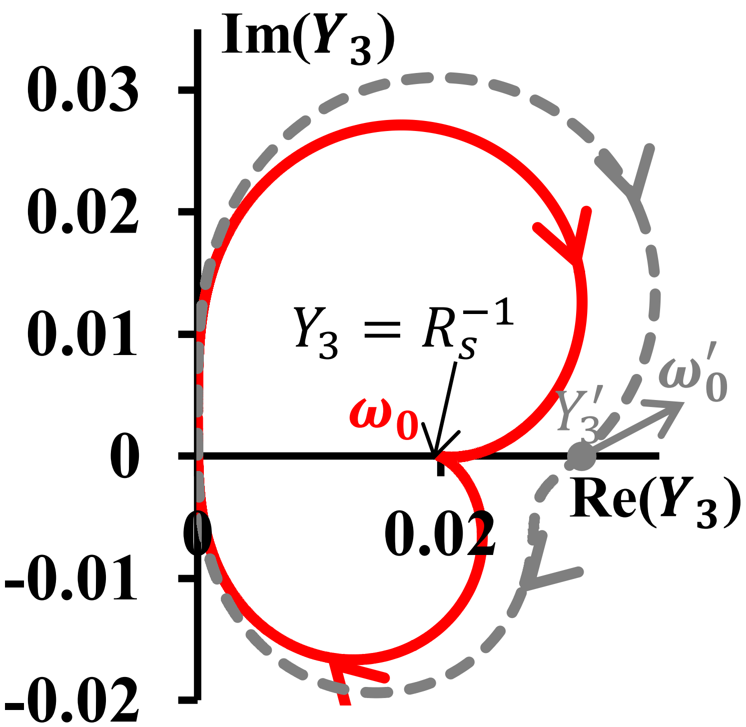

(b)

Fig. 51 Simulated Nyquist plots for the input admittance in the cases of (a) $Y_3<R_s^{-1}$, (b) $Y_3=R_s^{-1}$ (solid line), and $Y_3'>R_s^{-1}$ (dash line). $\omega_{0,1,2}$ stand for the frequency where the phase of the admittance is zero.

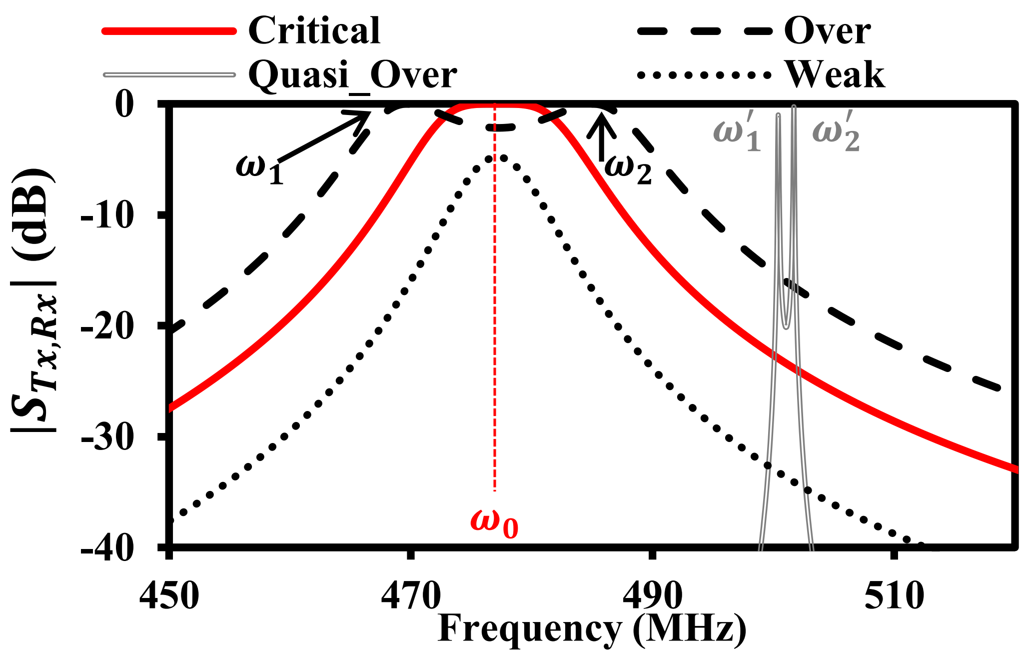

Fig. 52 Simulated S-parameter ($|S_{Tx,Rx}|$) in 4 cases: critical coupling (Critical), over coupling (Over), quasi-over coupling (Quasi_Over), and weak coupling (Weak).

7.2.2 Four Cases' Summary

1) Case I: Critical Coupling ($Y_3^*=R_s^{-1}$):

Based on the dimensions of the proposed system, the S-Parameter can be estimated as shown in Fig. 52. Assuming that the optimized input admittance Y_3^* is:

$$Y_3^* = \frac{J_1^{*2} J_2^{*2} R_s}{J_m^{*2}} = R_s^{-1} \tag{7.1}$$

Where $J_{1,2,m}^*$ are the optimized values of J-inverters for the proposed WPT. In this case, the PTE is maximized.

When $Y_3<R_s^{-1}$, two cases are supposed to be taken into consideration: $J_m>J_m^*$, $J_1<J_1^*$. Additionally, the mutual inductance (M) and series capacitor (C_s) can be calculated [20].

$$M(d^{-1}) = \frac{\omega_0 L_p'^2 J_m}{1-\omega_0^2 L_p'^2 J_m^2} \tag{7.2}$$

$$C_s = \frac{J_1}{\omega_0\sqrt{1-(J_1 R_s)^2}} \tag{7.3}$$

2) Case II: Over Coupling ($J_m > J_m^*$):

Going back to the layout to be optimized, according to (7.1), when the WPT distance (d) becomes too small, the mutual inductance (M) becomes bigger, resulting in $J_m > J_m^*$ and $Y_3 < R_s^{-1}$. Consequently, according to Fig. 51 (b). the WPT system exhibits over-coupling phenomena, and two resonant frequencies commonly emerge [6].

3) Case III: Quasi-Over Coupling ($J_1 < J_1^*$):

However, even if the Rx is far away from the Tx if the series capacitor becomes smaller due to (7.2), $J_1 < J_1^*$ and $Y_3 < R_s^{-1}$. So, the S-parameter, as shown in Fig. 51 (b), still shows two resonant frequencies identical to the last case. Whereas because the curve in Fig. (b) is not through the point of Y_3 ($\boldsymbol{Y_3' \neq Y_3}$), the WPT performance (PTE) would be far worse than the over-coupling case (Case II). Therefore, the predictor should be precise enough to predict Case III (rather than wrongly identified as weak coupling or over coupling), so the optimizer could more likely find the best solution.

4) Case IV: Weak Coupling ($J_m < J_m^*$):

In this case, the mutual inductance (M) between the Tx and Rx is smaller than the optimized value, so the power transfer between the coils is weak. Again, as shown in Fig. 51 (b), due to (7.1), $J_m < J_m^*$ and $Y_3 > R_s^{-1}$, the WPT performance falls under the weak coupling regime.

5) Abnormal Case:

Additionally, we must notice that there are also some hybrid and abnormal cases of the WPT. For example, Fig. 53 illustrates the quasi-over coupling in the worst matching case with weak coupling and when the resonant frequency (the frequency of the peaks) is beyond the range of 100 MHz to 1 GHz and combined with the weak coupling cases, respectively. These cases may confuse the AI and make the prediction performance worse. Although these abnormal cases can be deleted, it would make the data harder to collect.

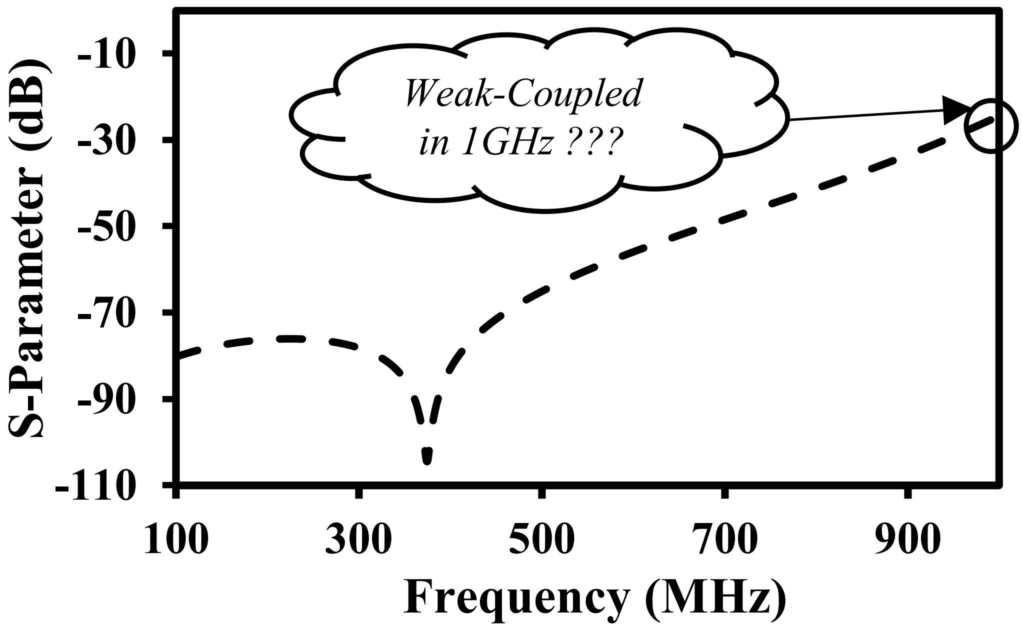

Fig. 53 When the resonant frequency is beyond 100 MHz to 1 GHz.

7.3 Simulated S-Parameter

The simulation results in Fig. 52 demonstrate that the proposed WPT system's S-parameters exhibit good agreement with the theoretical analysis for all four coupling cases.

Noticing that, in the quasi-over coupling case, a huge frequency derivation occurs. In addition to (1), the shunt capacitor of the converted circuit (C_p') is derived from:

$$C_p' = C_p - \frac{C_s}{1 + (\omega_0 C_{s2} R)^2} \tag{7.4}$$

Therefore, C_p' would vary dramatically with the derivation of C_s, resulting in the WPT's resonant frequency shifting.

In addition to analyzing the resonant frequency, the proposed WPT system's PTE can be calculated using (7.5) based on the S-parameter [68]:

$$\eta = |S_{Tx.Rx}|^2 \tag{7.5}$$

However, calculating and simulating the WPT system within the desired frequency band can be time-consuming, particularly for designers unfamiliar with DGS.

7.4 Predicting S-parameter: LSTM-based Neural Network

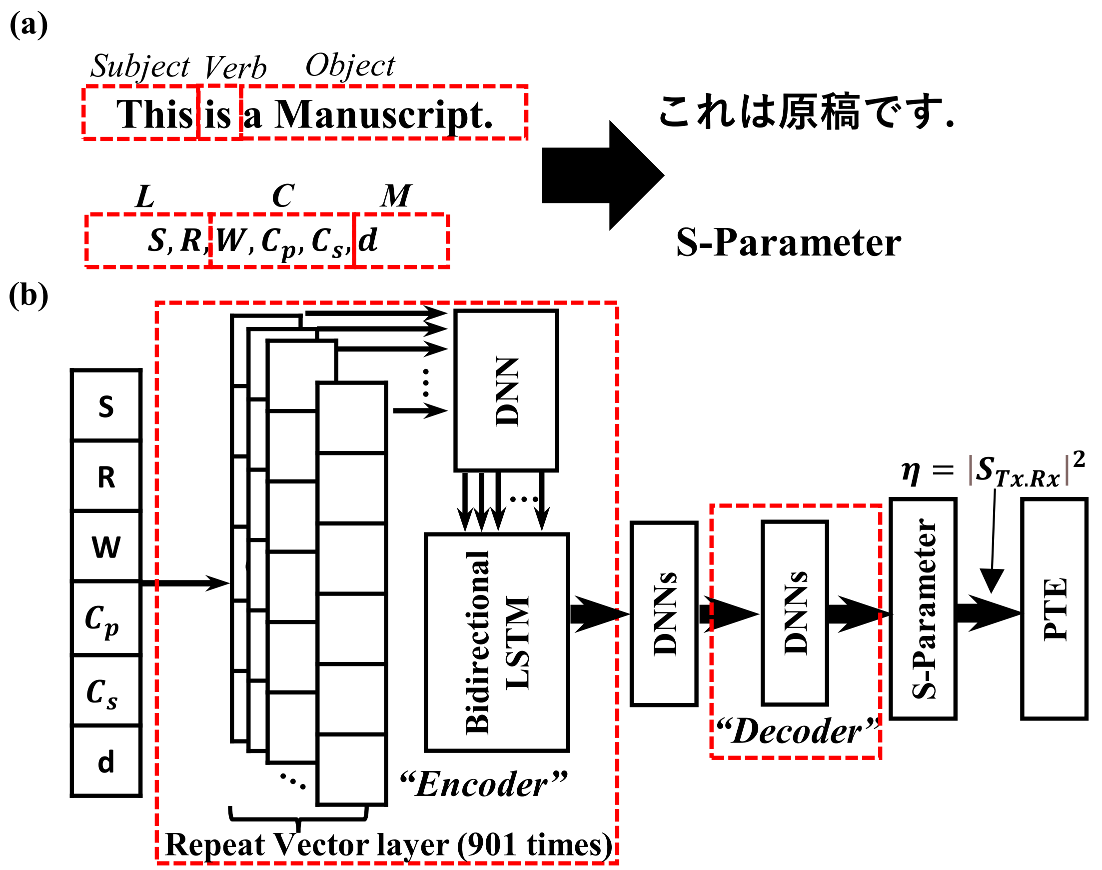

Fig. 54 (a) Analogous of a translator for subject-verb-object structure sentences and L (Inductance) C (Capacitance) M (Mutual Inductance) structure parameters in set χ. (b) A simple encoder-decoder structure to "translate" dimensions to the S-parameter. Then the PTE can be figured out by (10).

Compared to the ANN with a fully-connected dense layer, a long short-term memory (LSTM) method is better suited for predicting sequence data [69]–[71]. Fig. 54 (a) indicates an analogous to identifying descriptive text using a specific set of rules (i.e., grammar). Similarly, the dimensions of the Tx (Rx) (shown in Table I) can be viewed as a 'sentence' that represents a consequence of the S-parameter within different frequency domains (like the same sentence in a different context in linguistically speaking).

So that the parameters in Table I can be summarized as follows:

$$\chi = [S, R, W, C_p, C_s, d] \tag{7.6}$$

7.4.1 Identifying 4 Cases: A Simple Encoder-Decoder Structure:

Fig. 54 (b) illustrates a simple encoder-decoder structure. Bi-directional LSTM is used for the Encoder part. Meanwhile, instead of another LSTM for the decoder, a couple of simple dense layers (DNNs) are used to reduce the complexity of the proposed neural network so that we do not need much GPU memory to train the neural network. 3000 training datasets (2900 for the training) are automatically collected from the HFSS using PyAEDT. The volume of the whole dataset is 50.1 MB, which is significantly reduced compared to [69]. A GeForce RTX 3060Ti (GPU Memory: 16 GB) trains the network.

7.4.2 A Repeat Vector Layer:

Meanwhile, before the LSTM, we add a repeat vector layer repeating the input 901 times (the shape is 901 × 6) better to map the S-parameters (901 × 1). In fact, the repeat vector layer we used is inspired by the embedding layer in the text processing and fuzzy interference system. Using the repeat vector layer, we could give the AI more space to justify which cases it should be based on the rule they learned from the training dataset.

7.4.3 Randomly Sampled Dataset

TABLE 7 Range of the WPT's Dimensions for Dataset

C_p	C_s	d	R	S	W
1 pF-50 pF	0.1 pF-$C_p'/4$	$S' \times 0.8$ - $S' \times 1.5$	$S'/5$-$S'/2$	3 mm-30 mm	0.5 mm-5 mm

1) Sampled Rules:

TABLE 7 indicates the range of each dimension of the training dataset. We consider the geometric constraint so that $\boldsymbol{R}$ (radius of the inner circle) can not be over half of the sampled $\boldsymbol{S}$ (width (length) of the Tx(Rx)). What is more, we also control the $\boldsymbol{d}$ and shunt capacitor $\boldsymbol{C_s}$ within a reasonable range (based on our design experience) when the $\boldsymbol{S}$ and shunt capacitor $\boldsymbol{C_p}$ are first sampled (the sampled $\boldsymbol{S}$ and $\boldsymbol{C_p}$ are denoted by $\boldsymbol{S'}$ and $\boldsymbol{C'_p}$, respectively). As the frequency range is 100 MHz to 1 GHz with an interval of 1 MHz, 901 S-parameters are supposed to be collected.

2) Distributions of WPT Frequency:

Fig. 55 illustrates the distribution of operating frequencies in the dataset based on the range of dimensions. It is worth noting that an abnormal number is observed at the fringe of the sampled frequency (i.e., 900 MHz). This abnormality is attributed to the definition of the frequency with the best power transfer efficiency. As a result, the dataset includes a concentration of data points around the optimal frequency, leading to a noticeable deviation from the overall frequency distribution.

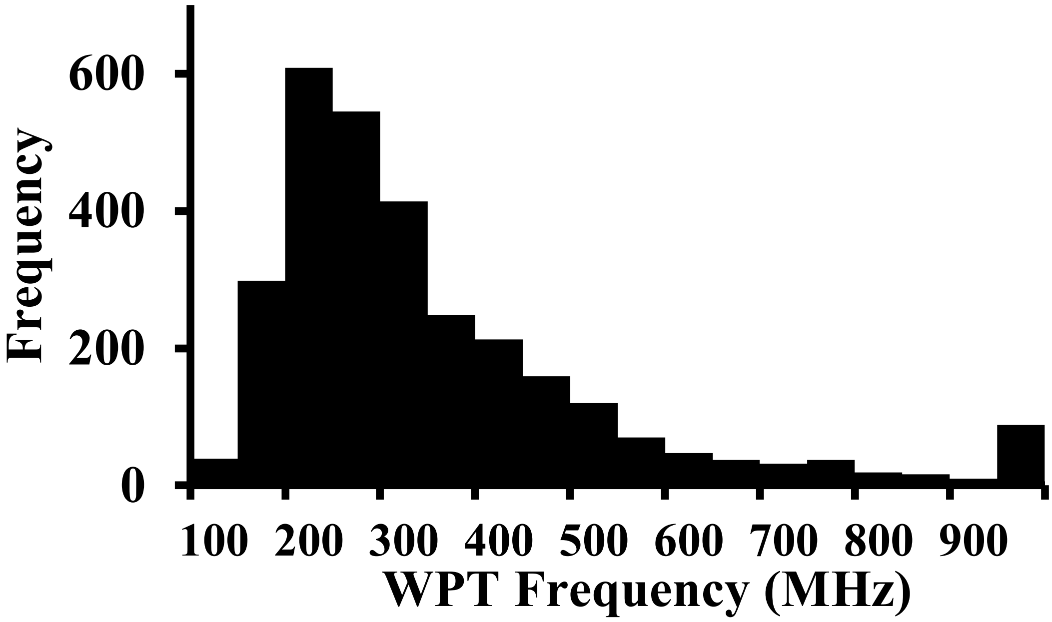

Fig. 55 Histogram for the WPT frequency distribution of the dataset. The WPT frequency is the frequency where the PTE is maximized.

2) Loss Function:

In the critical coupling case, more accuracy should be expected in the lower part so that if the data is only composed of the critical coupling, the Mean Absolute Percentage Error (MAPE) function might be more suitable than the commonly-used Mean-square Error (MSE) function. On the other hand, if the MAPE function were used, less care would be considered in the weak coupling and quasi-coupling cases.

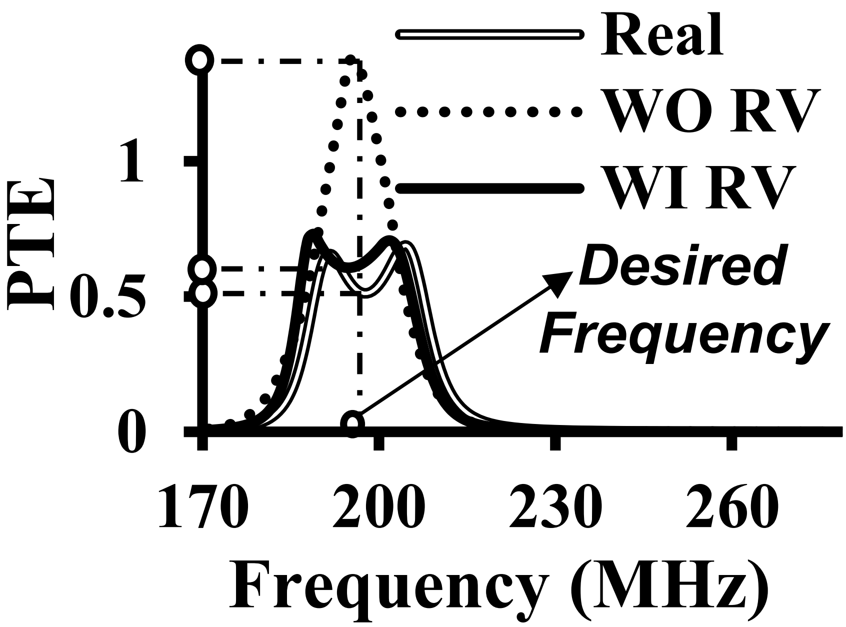

(a)

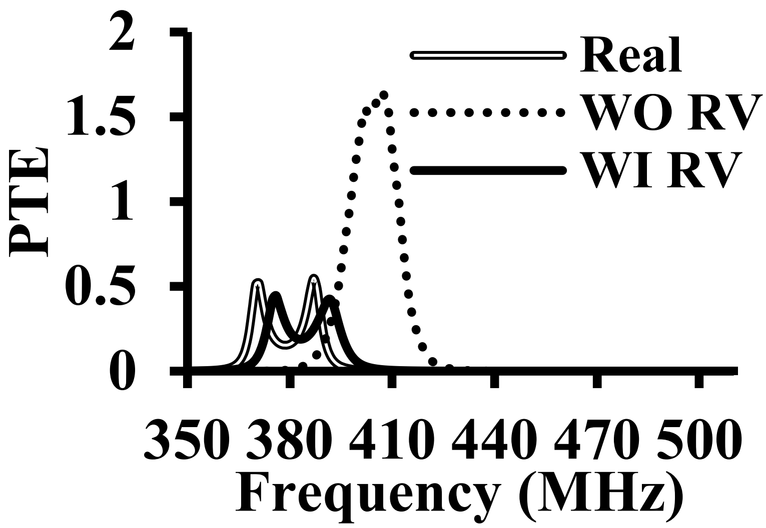

(b)

Fig. 56 Performance of PTEs predicted without the repeat vector layer (WO RV) and with the repeat vector layer (WI RV) compared with the real PTE (Real) in two cases: (a) Over Coupling case and (b) Quasi-over coupling case.

Hence, consequently, we decided to use the MSE as the loss function, which is:

$$MSE = \frac{\sum_{i=1}^{n}(X_i - x_i)^2}{N} \tag{7.7}$$

Where N stands for the points of the S-parameters. X_i, x_i stand for the real and predicted S-parameters, respectively.

As shown in Fig. 56, Cases II and III can be identified with the help of the repeat vector layer, respectively. If the over-coupling case is not correctly identified, the PTE in the desired frequency may be above 100%. Especially if the quasi-over coupling case can not be correctly predicted, the predicted frequency might be shifted, not only the PTE. Each result would give wrong hints to the optimizers, resulting in more time or even wrong optimization results.

7.5 Finding Optimized Layout: Dual Annealing

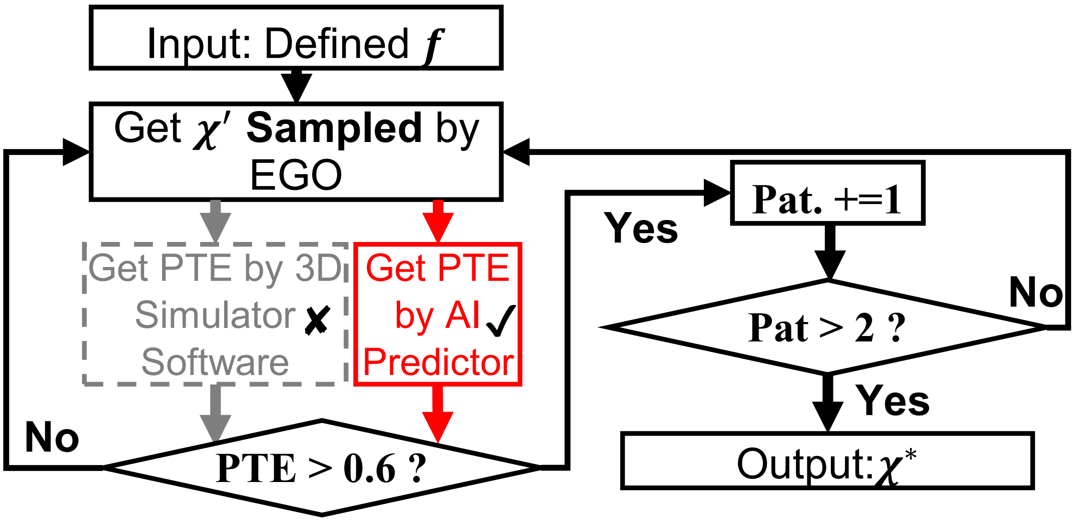

Fig. 57 Flowchart of the proposed inverse modeling method. f is the desired frequency band of the WPT system. χ, χ^* are the matrix of the sampled and optimized dimensions, respectively. An efficient global optimization (EGO) algorithm finds one of the best solutions.

Based on the predictor, we propose an inverse model, and its flow chart is depicted Fig. 57. The proposed predictor aids in significantly speeding up the process of obtaining power transfer efficiency (PTE) results compared to using HFSS alone. Using the efficient global optimization (EGO) technique, the inverse model leverages the predictor to guide the sampling of matrices that are believed to be closer to the best solution. This approach allows for more efficient exploration of the solution space and facilitates quicker convergence towards optimal PTE results.

7.6 Results

In Fig. 58, we present a comparison between the desired frequency and the working frequency simulated by HFSS. The operating frequency is chosen as the point of best performance. It can be observed that the predicted layout closely matches the desired frequency with a small error tolerance, indicating that the predicted layout meets the requirements for the working frequency.

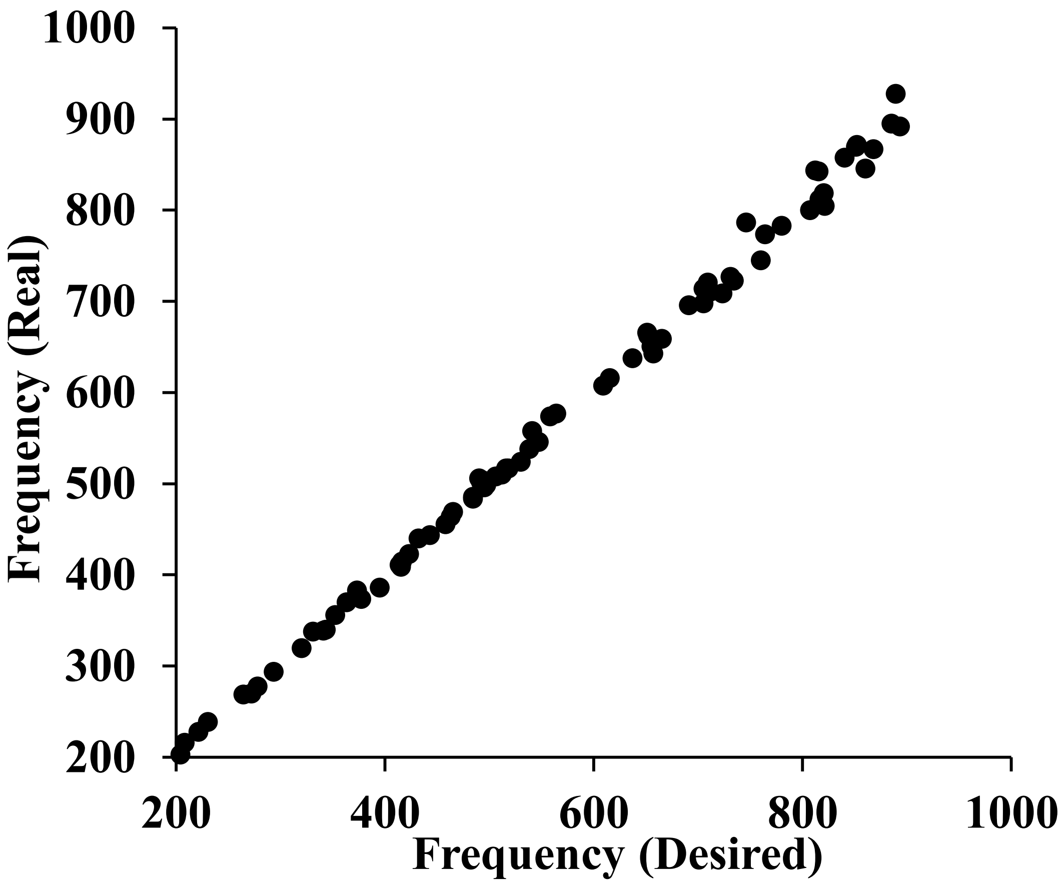

Fig. 58 Comparison of the WPT frequency of the design predicted by the inverse model and real(desired) frequency. The dots are supposed to be closed to the y=x if the WPT frequencies of the predicted designs are the same as the real(desired) frequencies.

Furthermore, Fig. 59 illustrates the efficiency of the predicted layouts. Most of the predicted layouts exhibit efficiencies above 60%. However, for desired frequencies exceeding 500 MHz, the lack of samples in the corresponding frequency range (samples above 500 MHz) leads to prediction errors. This suggests that the prediction accuracy decreases in those specific frequency ranges due to insufficient data points. Therefore, the strategy of dataset sampling is supposed to be optimized in the future work.

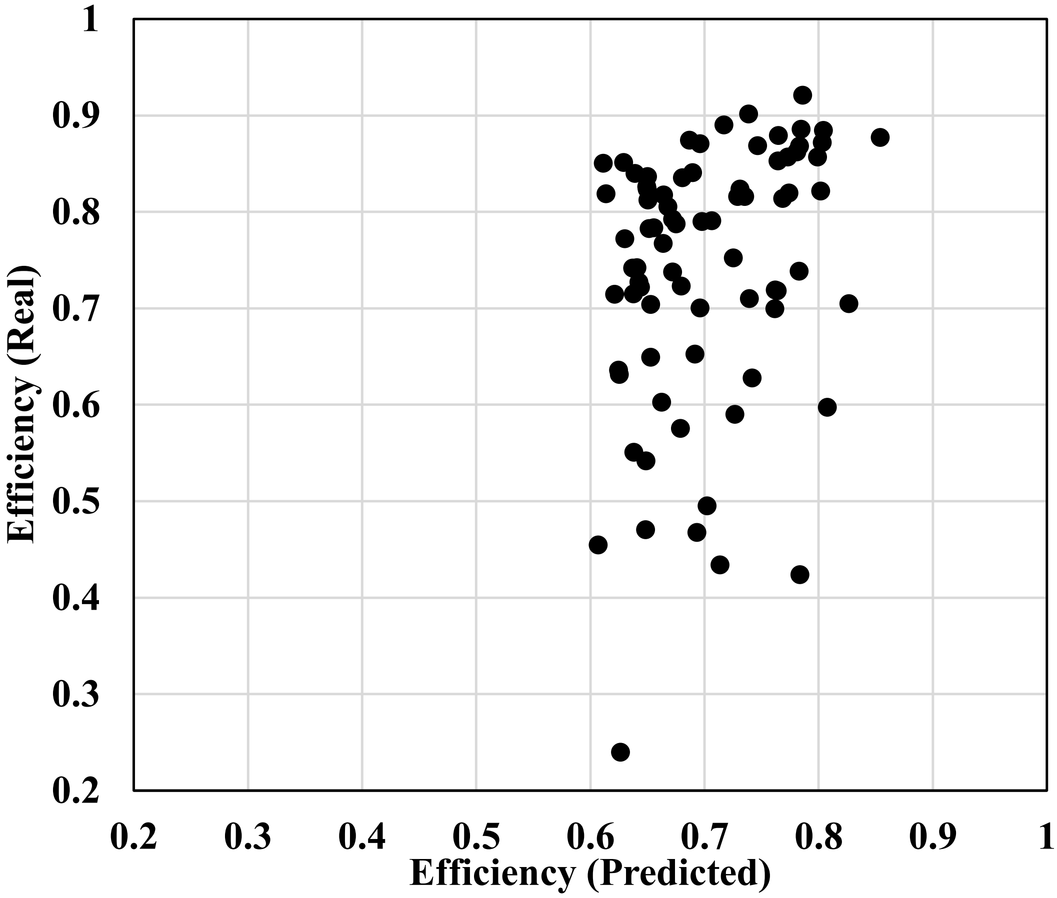

Fig. 59 Comparison of the efficiency predicted by the AI-predictor (Efficiency (Predicted)) and the efficiency estimated by HFSS (Efficiency (Real)).

7.7 Conclusion

In this chapter, a compressed inverse model for a DGS-based wireless power transfer (WPT) system is proposed. The chapter begins by introducing the admittance (J-) inverter technique, which is used to identify the four basic coupling types in WPT: critical coupling, over-coupling, weak coupling, and other abnormal cases.

The next section presents a simple translator-inspired encoder-decoder neural network that serves as a classifier for these four coupling types. The entire dimension of the system is used as inputs to the neural network.

By predicting the scattering (S-) parameter, the power transfer efficiency (PTE) can be determined at the desired frequency. To address the non-uniqueness problem commonly encountered in inverse model establishment, a dual annealing algorithm is proposed.

The chapter concludes by integrating the proposed AI-based predictor into the inverse model, resulting in a complete framework for the compressed inverse model of the DGS-based WPT system.

8 Conclusion

In conclusion, this work presents a comprehensive investigation into the application of metamaterials for enhancing the performance of dual-band wireless power transfer (WPT) systems. Three types of metamaterials are proposed and studied to address specific challenges and improve key aspects of WPT.

Chapter 2 provides a thorough background and highlights the challenges associated with metamaterials in dual-band WPT. It identifies limitations and issues with previously proposed metamaterials, emphasizing the need for innovative solutions.

Chapter 3 introduces a multi-mode stacked metamaterial, designed to optimize power transfer efficiency for each band of the dual-band WPT system. While the experiment demonstrates significant improvements in wireless power transfer efficiency, the expected enhancement in lateral misalignment tolerance is not achieved due to the topology.

To address the misalignment issue, Chapter 4 presents a novel hybrid split ring resonator (SRR)-based metamaterial. This metamaterial exhibits two near-zero permeability points that can be optimized within the desired frequency range, thereby mitigating the misalignment challenges.

Chapter 5 focuses on a nonreciprocal metamaterial designed as an absorber for a dual-band simultaneous information and power transfer (SWIPT) system. This absorber effectively reduces interference between the signal and power bands when signals are input into the signal port, enhancing the signal quality.

Overall, this research contributes valuable insights and solutions for dual-band WPT systems through the innovative application of metamaterials. The proposed metamaterials address key performance aspects such as power transfer efficiency, misalignment tolerance, and interference reduction, laying the foundation for future advancements in the field.

8.1 Future Work

Fig. 61(a) illustrates the efficiency degradation at the central frequency when the transmitter (Tx) and receiver (Rx) are positioned too closely, resulting in an overcoupling effect. To overcome this challenge and achieve positional independence in wireless power transfer (WPT), we propose the application of the metamaterial's self-resonant theory:

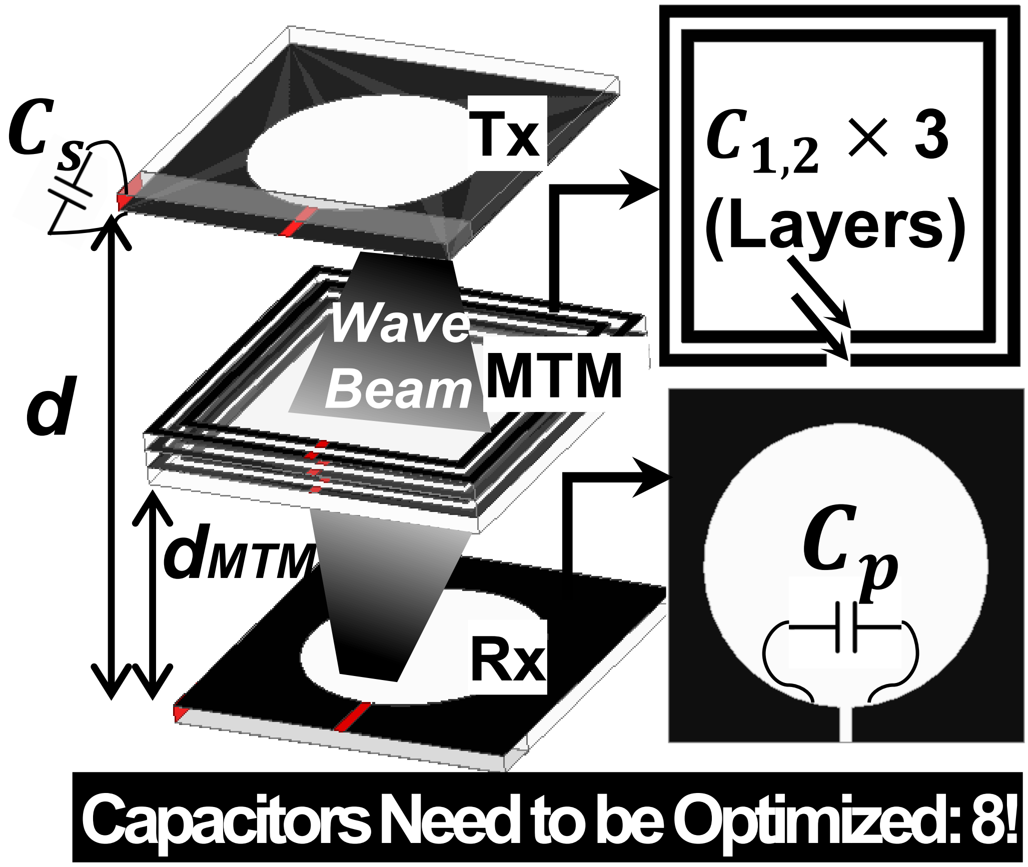

Fig. 60 Model of WPT system of 'DGS+MTM'. C_s are etched between top and bottom's coppers

According to the coupled-mode theory [72], the proposed WPT using stacked metamaterial can be described as:

$$\frac{d}{dt}\begin{bmatrix} v_1 \\ v_2 \\ v_3 \end{bmatrix} = \begin{bmatrix} i\omega_1 - \beta_1 & k_{12} & k_{13} \\ k_{21} & i\omega_2 - \beta_2 & k_{23} \\ k_{31} & k_{32} & i\omega_3 - \beta_3 \end{bmatrix} \begin{bmatrix} v_1 \\ v_2 \\ v_3 \end{bmatrix} \tag{8.1}$$

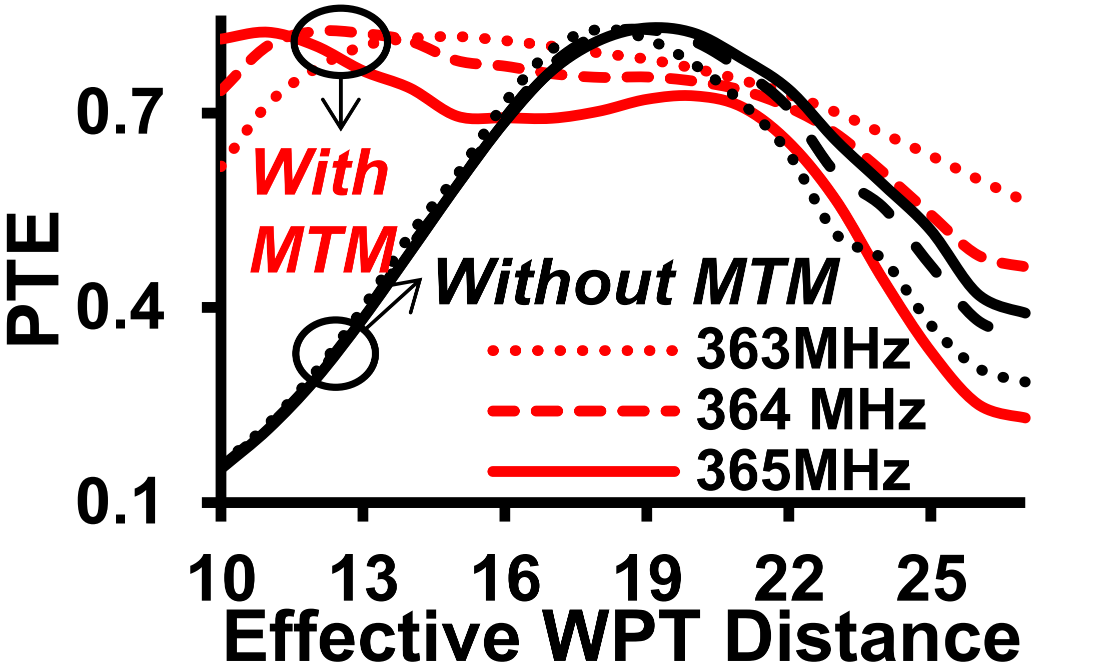

(a)

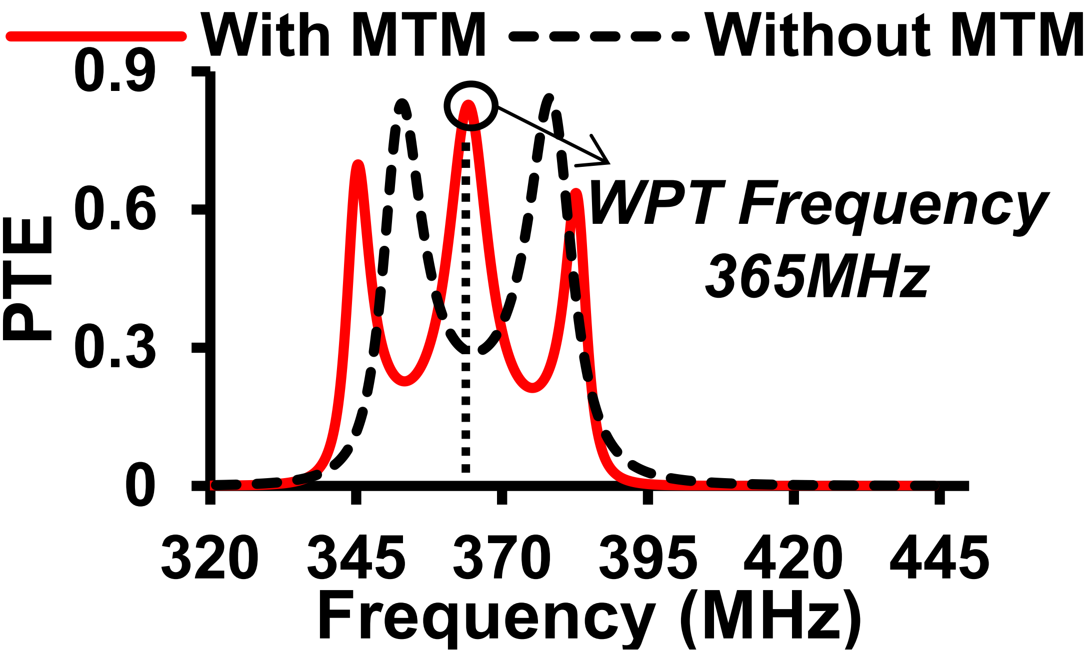

(b)

Fig. 61 . Simulated results of (a) PTE when the system without (Effective WPT distance = d mm) and with MTM (Effective WPT distance = d_{MTM} mm). (b) Efficiency (PTE) in the overcoupling region with and without the proposed metamaterial (MTM).

In this context, the indices represent the transmitter (Tx), metamaterial, and receiver (Rx) respectively. The variable v represents the amplitudes of the magnetic field, while k denotes the coupling strength between each element. Additionally, β signifies the intrinsic loss associated with each element. Since the Tx, Rx, and metamaterial share the same substrate and size, we can assume that β_1, β_2, β_3 are approximately equal to a common value β. It is important to note that the metamaterial is positioned in the middle, resulting in k_{12}, k_{21}, k_{23}, and k_{32} being equal to a coupling constant denoted as k'. Furthermore, it is evident that k_{13} and k_{31} are both equal to k. Assuming a relationship of $v \propto \exp(j\omega t)$, we can determine the characteristic equation.

$$\prod_{n=1}^{3}[i(\omega_n-\omega)-\beta_n]+k^2 \\ -\left[\sum_{m=1}^{3}\beta_m+i(\omega_1+\omega_3-2\omega)\right]k'^2=0 \tag{8.2}$$

When the self-resonance frequency ω_2 is not equal to ω_1 or ω_3, and ω_0 represents the characteristic frequency, the eigenmode frequencies can be determined by solving the real part of (9.2). It is worth noting that the roots of real numbers can only be derived from the imaginary part.

$$\omega^3-3\omega_0\omega^2-(3\beta^2+2k'^2+3\omega_0^2)\omega \\ +3\beta^2\omega_0-2k'^2\omega_0-\omega_0^3=0 \tag{8.3}$$

And the roots are:

$$\begin{cases} \omega_0 \\ \omega_0-(3\beta^2-k^2-2k'^2)^{\frac{1}{2}} \\ \omega_0+\left(3\beta^2-k^2-2k'^2\right)^{\frac{1}{2}} \end{cases} \tag{8.4}$$

Therefore, if the coupling between metamaterial to the Tx (Rx) (k') is strong enough, three resonant frequencies occur so that the energy is dissipated into three resonant frequencies, resulting in a PTE loss.

Through the implementation of the self-resonant theory, we can achieve a positional-independent WPT system where the efficiency remains high even when the Tx and Rx are in close proximity. This advancement in WPT technology enables more flexibility and convenience in the charging process, as the user is no longer constrained by strict positioning requirements for optimal power transfer efficiency.

By leveraging the benefits of the metamaterial's self-resonant theory, we can effectively address the efficiency degradation caused by the overcoupling effect and pave the way for enhanced positional independence in WPT applications. Also the capacitors shown in Fig. 60 is supposed to be optimized by the AI fast and automatically in the future work.

Reference

[1] P. Gutruf *et al.*, “Wireless, battery-free, fully implantable multimodal and multisite pacemakers for applications in small animal models,” *Nat. Commun.*, vol. 10, no. 1, p. 5742, Dec. 2019.

[2] P. Chen, H. Yang, R. Luo, and B. Zhao, “A tissue-channel transcutaneous power transfer technique for implantable devices,” *IEEE Trans. Power Electron.*, vol. 33, no. 11, pp. 9753–9761, Nov. 2018.

[3] C. Liu, C. Jiang, J. Song, and K. T. Chau, “An effective sandwiched wireless power transfer system for charging implantable cardiac pacemaker,” *IEEE Trans. Ind. Electron.*, vol. 66, no. 5, pp. 4108–4117, May 2019.

[4] M. Zada, I. A. Shah, A. Basir, and H. Yoo, “Simultaneous Wireless Power Transfer and Data Telemetry Using Dual-Band Smart Contact Lens,” *IEEE Trans. Antennas Propag.*, vol. 70, no. 4, pp. 2990–3001, Apr. 2022.

[5] J. Jang, J. Lee, H. Cho, J. Lee, and H.-J. Yoo, “Wireless Body-Area-Network Transceiver and Low-Power Receiver With High Application Expandability,” *IEEE J. Solid-State Circuits*, vol. 55, no. 10, pp. 2781–2789, Oct. 2020.

[6] J. Pan, A. A. Abidi, W. Jiang, and D. Markovic, “Simultaneous Transmission of Up To 94-mW Self-Regulated Wireless Power and Up To 5-Mb/s Reverse Data Over a Single Pair of Coils,” *IEEE J. Solid-State Circuits*, vol. 54, no. 4, pp. 1003–1016, Apr. 2019.

[7] A. Yousefi, A. A. Abidi, and D. Markovic, "Analysis and design of a robust, low-power, inductively coupled LSK data link," *IEEE J. Solid-State Circuits*, vol. 55, no. 9, pp. 2583–2596, Sep. 2020.

[8] F. Tahar, R. Saad, A. Barakat, and R. K. Pokharel, "1.06 FoM and Compact Wireless Power Transfer System Using Rectangular Defected Ground Structure Resonators," *IEEE Microw. Wireless Compon. Lett.*, vol. 27, no. 11, pp. 1025–1027, Nov. 2017.

[9] S. Hekal, A. B. Abdel-Rahman, H. Jia, A. Allam, A. Barakat, and R. K. Pokharel, "A novel technique for compact size wireless power transfer applications using defected ground structures," *IEEE Trans. Microw. Theory Techn.*, vol. 65, no. 2, pp. 591–599, Feb. 2017.

[10] A. Barakat, K. Yoshitomi, and R. K. Pokharel, "Design Approach for Efficient Wireless Power Transfer Systems During Lateral Misalignment," *IEEE Trans. Microw. Theory Techn.*, vol. 66, no. 9, pp. 4170–4177, Sep. 2018.

[11] A. Barakat, S. Alshhawy, K. Yoshitomi, and R. K. Pokharel, "Simultaneous Wireless Power and Information Transfer Using Coupled Co-Existing Defected Ground Structure Resonators," *IEEE Trans. Circuits Syst. II, Exp. Briefs*, vol. 68, no. 2, pp. 632–636, Feb. 2021.

[12] A. Barakat, S. Alshhawy, K. Yoshitomi, and R. K. Pokharel, "Triple-Band Near-Field Wireless Power Transfer System Using Coupled Defected Ground Structure Band Stop Filters," in *Dig. of 2019 IEEE MTT-S Int. Microw. Symp.*, Boston, MA,

USA, Jun. 2019, pp. 1411–1414.

[13] X. Jiang, F. Tahar, T. Miyamoto, A. Barakat, K. Yoshitomi, and R. K. Pokharel, "Efficient and compact dual-band wireless power transfer system through biological tissues using dual-reference DGS resonators," in *Dig. of 2021 IEEE MTT-S Int. Microw. Symp.*, Atlanta, GA, USA, Oct. 2021, pp. 54–57.

[14] Y. Cho *et al.*, "Thin hybrid metamaterial slab with negative and zero permeability for high efficiency and low electromagnetic field in wireless power transfer systems," *IEEE Trans. Electromagn. Compat.*, vol. 60, no. 4, pp. 1001–1009, Aug. 2018.

[15] Y. Cho *et al.*, "Thin PCB-type metamaterials for improved efficiency and reduced EMF leakage in wireless power transfer systems," *IEEE Trans. Microw. Theory Techn.*, pp. 1–12, 2016.

[16] Y. Urzhumov and D. R. Smith, "Metamaterial-enhanced coupling between magnetic dipoles for efficient wireless power transfer," *Phys. Rev. B*, vol. 83, no. 20, p. 205114, May 2011.

[17] C. Lu, X. Huang, C. Rong, X. Tao, Y. Zeng, and M. Liu, "A dual-band negative permeability and near-zero permeability metamaterials for wireless power transfer system," *IEEE Trans. Ind. Electron.*, pp. 1–1, 2020.

[18] A. Barakat, R. K. Pokharel, S. Alshhawy, K. Yoshitomi, and S. Kawasaki, "High Isolation Simultaneous Wireless Power and Information Transfer System Using Coexisting DGS resonators and Figure-8 Inductors," in *Dig. of 2020 IEEE MTT-*

S Int. Microw. Symp., Los Angeles, CA, USA, Aug. 2020, pp. 1172–1175.

[19] R. K. Pokharel, A. Barakat, S. Alshhawy, K. Yoshitomi, and C. Sarris, "Wireless power transfer system rigid to tissue characteristics using metamaterial inspired geometry for biomedical implant applications," *Sci. Rep.*, vol. 11, no. 1, p. 5868, Mar. 2021.

[20] J. Lee, Y.-S. Lim, W.-J. Yang, and S.-O. Lim, "Wireless power transfer system adaptive to change in coil separation," *IEEE Trans. Antennas Propag.*, vol. 62, no. 2, pp. 889–897, Feb. 2014.

[21] H. Yang, Y. Ye, X. Chu, and M. Dong, "Resource and Power Allocation in SWIPT-Enabled Device-to-Device Communications Based on a Nonlinear Energy Harvesting Model," *IEEE Internet Things J.*, vol. 7, no. 11, pp. 10813–10825, Jan. 2020.

[22] Y. Xu, H. Xie, C. Liang, and F. R. Yu, "Robust Secure Energy-Efficiency Optimization in SWIPT-Aided Heterogeneous Networks With a Nonlinear Energy-Harvesting Model," *IEEE Internet Things J.*, vol. 8, no. 19, pp. 14908–14919, Oct. 2021.

[23] K. W. Choi *et al.*, "Simultaneous Wireless Information and Power Transfer (SWIPT) for Internet of Things: Novel Receiver Design and Experimental Validation," *IEEE Internet Things J.*, vol. 7, no. 4, pp. 2996–3012, Apr. 2020.

[24] X. Zhao, Y. Zhang, S. Geng, F. Du, Z. Zhou, and L. Yang, "Hybrid Precoding for an Adaptive Interference Decoding SWIPT System With Full-Duplex IoT

Devices," *IEEE Internet Things J.*, vol. 7, no. 2, pp. 1164–1177, Feb. 2020.

[25] J. J. Park, J. H. Moon, K.-Y. Lee, and D. I. Kim, "Transmitter-Oriented Dual-Mode SWIPT With Deep-Learning-Based Adaptive Mode Switching for IoT Sensor Networks," *IEEE Internet Things J.*, vol. 7, no. 9, pp. 8979–8992, Sep. 2020.

[26] M. Wagih, G. S. Hilton, A. S. Weddell, and S. Beeby, "Dual-Polarized Wearable Antenna/Rectenna for Full-Duplex and MIMO Simultaneous Wireless Information and Power Transfer (SWIPT)," *IEEE Antennas Propag. Mag.*, vol. 2, pp. 844–857, 2021.

[27] W. Lu *et al.*, "Energy Efficiency Optimization in SWIPT Enabled WSNs for Smart Agriculture," *IEEE Trans. Ind. Informat.*, vol. 17, no. 6, pp. 4335–4344, Jun. 2021.

[28] F. L. Cabrera and F. R. de Sousa, "Achieving Optimal Efficiency in Energy Transfer to a CMOS Fully Integrated Wireless Power Receiver," *IEEE Trans. Microw. Theory Techn.*, vol. 64, no. 11, pp. 3703–3713, Nov. 2016.

[29] C. Psomas, M. You, K. Liang, G. Zheng, and I. Krikidis, "Design and Analysis of SWIPT With Safety Constraints," *Proc. IEEE*, vol. 110, no. 1, pp. 107–126, Jan. 2022.

[30] A. Rajagopalan, A. K. RamRakhyani, D. Schurig, and G. Lazzi, "Improving power transfer efficiency of a short-range telemetry system using compact metamaterials," *IEEE Trans. Microw. Theory Techn.*, vol. 62, no. 4, pp. 947–955,

Apr. 2014.

[31] H.-D. Lang and C. D. Sarris, “Optimization of wireless power transfer systems enhanced by passive elements and metasurfaces,” *IEEE Trans. Antennas Propag.*, vol. 65, no. 10, p. 13, 2017.

[32] S. Tian, X. Zhang, X. Wang, J. Han, and L. Li, “Recent advances in metamaterials for simultaneous wireless information and power transmission,” *Nanophotonics*, vol. 11, no. 9, pp. 1697–1723, May 2022.

[33] H. Younesiraad and M. Bemani, “Analysis of coupling between magnetic dipoles enhanced by metasurfaces for wireless power transfer efficiency improvement,” *Sci. Rep.*, vol. 8, no. 1, p. 14865, Dec. 2018.

[34] L. Li, H. Liu, H. Zhang, and W. Xue, “Efficient wireless power transfer system integrating with metasurface for biological applications,” *IEEE Trans. Ind. Electron.*, vol. 65, no. 4, pp. 3230–3239, Apr. 2018.

[35] J. B. Pendry, A. J. Holden, D. J. Robbins, and W. J. Stewart, “Magnetism from conductors and enhanced nonlinear phenomena,” *IEEE Trans. Microw. Theory Techn.*, vol. 47, no. 11, pp. 2075–2084, Nov. 1999.

[36] D. R. Smith, D. C. Vier, and N. Kroll, “Direct calculation of permeability and permittivity for a left-handed metamaterial,” *Appl. Phys. Lett.*, p. 4.

[37] M. Aboualalaa, I. Mansour, and R. K. Pokharel, “Experimental Study of Effectiveness of Metasurface for Efficiency and Misalignment Enhancement of Near-Field WPT System,” *Antennas Wirel. Propag. Lett.*, vol. 21, no. 10, pp.

2010–2014, Jul. 2022.

[38] S. Alshhawy, A. Barakat, K. Yoshitomi, and R. K. Pokharel, “Compact and Efficient WPT System to Embedded Receiver in Biological Tissues Using Cooperative DGS Resonators,” *IEEE Trans. Circuits Syst. II, Exp. Briefs*, vol. 69, no. 3, pp. 869–873, Mar. 2022.

[39] C. Saha and J. Y. Siddiqui, “Estimation of the resonance frequency of conventional and rotational circular split ring resonators,” in *Proc. of 2009 IEEE Applied Electromagnetics Conference (AEMC)*, Dec. 2009, pp. 1–3.

[40] D. Pozar, *Microwave Engineering*, 4th Edition. Wiley, 2011.

[41] M. I. Khan, Q. Fraz, and F. A. Tahir, “Ultra-wideband cross polarization conversion metasurface insensitive to incidence angle,” *J. Appl. Phys.*, vol. 121, no. 4, p. 045103, Jan. 2017.

[42] C. Huang, X. Ma, M. Pu, G. Yi, Y. Wang, and X. Luo, “Dual-band 90° polarization rotator using twisted split ring resonators array,” *Opt. Commun.*, vol. 291, pp. 345–348, Mar. 2013.

[43] S. Assawaworrarit, X. Yu, and S. Fan, “Robust wireless power transfer using a nonlinear parity–time-symmetric circuit,” *Nature*, vol. 546, no. 7658, Art. no. 7658, Jun. 2017.

[44] X. Jiang, R. K. Pokharel, A. Barakat, and K. Yoshitomi, “A multimode metamaterial for a compact and robust dualband wireless power transfer system,” *Sci. Rep.*, vol. 11, no. 1, p. 22125, Dec. 2021.

[45] Y. Ikeda, X. Jiang, M. Aboualalaa, A. Barakat, K. Yoshitomi, and R. K. Pokharel, "Stacked Metasurfaces for Misalignment Improvement of WPT System Using Spiral Resonators," in *Proc. of 2021 51st European Microwave Conference (EuMC)*, Apr. 2022, pp. 257–260.

[46] X. Jiang, R. K. Pokharel, A. Barakat, and K. Yoshitomi, "Wideband Stacked Metamaterial for a Compact and Efficient Dual-band Wireless Power Transfer," in *Dig. of 2022 IEEE MTT-S Int. Microw. Symp.*, Denver, CO, USA, Jun. 2022, pp. 198–201.

[47] C. Saha, Jawad. Y. Siddiqui, D. Guha, and Y. M. M. Antar, "Square Split Ring Resonators: Modelling of resonant frequency and polarizability," in *Proc. of 2007 IEEE Applied Electromagnetics Conference (AEMC)*, Kolkata, India, Dec. 2007, pp. 1–3.

[48] R. Marques, F. Mesa, J. Martel, and F. Medina, "Comparative analysis of edge- and broadside-coupled split ring resonators for metamaterial design - Theory and experiments," *IEEE Trans. Antennas Propag.*, vol. 51, no. 10, pp. 2572–2581, Oct. 2003.

[49] A. L. A. K. Ranaweera, T. P. Duong, and J.-W. Lee, "Experimental investigation of compact metamaterial for high efficiency mid-range wireless power transfer applications," *J. Appl. Phys.*, vol. 116, no. 4, p. 043914, Jul. 2014.

[50] C. Lu *et al.*, "Design and Analysis of an Omnidirectional Dual-Band Wireless Power Transfer System," *IEEE Trans. Antennas Propag.*, vol. 69, no. 6, pp. 3493–

3502, Jun. 2021.

[51] Q. Wang, W. Che, M. Mongiardo, and G. Monti, “Wireless Power Transfer System With High Misalignment Tolerance for Bio-Medical Implants,” *IEEE Trans. Circuits Syst. II, Exp. Briefs*, vol. 67, no. 12, pp. 3023–3027, Dec. 2020.

[52] C.-C. Hsu, K.-H. Lin, and H.-L. Su, “Implementation of Broadband Isolator Using Metamaterial-Inspired Resonators and a T-Shaped Branch for MIMO Antennas,” *IEEE Trans. Antennas Propag.*, vol. 59, no. 10, pp. 3936–3939, Oct. 2011.

[53] S. Wang, H.-X. Xu, M. Wang, C. Wang, Y. Wang, and X. Ling, “A Low-RCS and High-Gain Planar Circularly Polarized Cassegrain Meta-Antenna,” *IEEE Trans. Antennas Propag.*, vol. 70, no. 7, pp. 5278–5287, Jul. 2022.

[54] H. Zhu *et al.*, “A High Q -factor Metamaterial Absorber and Its Refractive Index Sensing Characteristics,” *IEEE Trans. Microw. Theory Techn.*, vol. 70, no. 12, pp. 5383–5391, Dec. 2022.

[55] T. Ueda, M. Kamino, T. Kondo, and T. Itoh, “Two-Degree-of-Freedom Control of Field Distribution on Nonreciprocal Metamaterial-Line Resonators and Its Applications to Polarization-Plane-Rotation and Beam- Scanning Leaky-Wave Antennas,” *IEEE Trans. Microw. Theory Techn.*, vol. 70, no. 1, pp. 50–61, Jan. 2022.

[56] C. Caloz and T. Itoh, *Electromagnetic Metamaterials: Transmission Line Theory and Microwave Applications*. Wiley, 2005.

[57] G. V. Eleftheriades, A. K. Iyer, and P. C. Kremer, "Planar negative refractive index media using periodically L-C loaded transmission lines," *IEEE Trans. Microw. Theory Techn.*, vol. 50, no. 12, pp. 2702–2712, Dec. 2002.

[58] F. Tahar, A. Barakat, R. Saad, K. Yoshitomi, and R. K. Pokharel, "Dual-band defected ground structures wireless power transfer system with independent external and inter-resonator coupling," *IEEE Trans. Circuits Syst. II, Exp. Briefs*, vol. 64, no. 12, pp. 1372–1376, Dec. 2017.

[59] A. Barakat, K. Yoshitomi, and R. K. Pokharel, "Design and implementation of dual-mode inductors for dual-band wireless power transfer systems," *IEEE Trans. Circuits Syst. II, Exp. Briefs*, vol. 66, no. 8, pp. 1287–1291, Aug. 2019.

[60] Y. Li, W. Dong, Q. Yang, S. Jiang, X. Ni, and J. Liu, "Automatic Impedance Matching Method With Adaptive Network Based Fuzzy Inference System for WPT," *IEEE Trans. Ind. Informat.*, vol. 16, no. 2, pp. 1076–1085, Feb. 2020.

[61] S. M. Won, L. Cai, P. Gutruf, and J. A. Rogers, "Wireless and battery-free technologies for neuroengineering," *Nat. Biomed. Eng.*, Mar. 2021.

[62] F. Feng, W. Na, J. Jin, J. Zhang, W. Zhang, and Q.-J. Zhang, "Artificial Neural Networks for Microwave Computer-Aided Design: The State of the Art," *IEEE Trans. Microw. Theory Techn.*, vol. 70, no. 11, pp. 4597–4619, Nov. 2022.

[63] M. Sedaghat, R. Trinchero, Z. H. Firouzeh, and F. G. Canavero, "Compressed Machine Learning-Based Inverse Model for Design Optimization of Microwave Components," *IEEE Trans. Microw. Theory Techn.*, vol. 70, no. 7, pp. 3415–3427,

Jul. 2022.

[64] Y. Wu, G. Pan, D. Lu, and M. Yu, "Artificial Neural Network for Dimensionality Reduction and Its Application to Microwave Filters Inverse Modeling," *IEEE Trans. Microw. Theory Techn.*, vol. 70, no. 11, pp. 4683–4693, Jan. 2022.

[65] L.-Y. Xiao, W. Shao, F.-L. Jin, B.-Z. Wang, and Q. H. Liu, "Inverse Artificial Neural Network for Multiobjective Antenna Design," *IEEE Trans. Antennas Propag.*, vol. 69, no. 10, pp. 6651–6659, Oct. 2021.

[66] M. Larbi, R. Trinchero, F. G. Canavero, P. Besnier, and M. Swaminathan, "Analysis of Parameter Variability in an Integrated Wireless Power Transfer System via Partial Least-Squares Regression," *IEEE Trans. Compon., Packag. Manufact. Technol.*, vol. 10, no. 11, pp. 1795–1802, Nov. 2020.

[67] A. Tarantola, *Inverse Problem Theory*. Society for Industrial and Applied Mathematics, 2005.

[68] A. Bodrov, S.-K. Sul, A. Bodrov, and S.-K. Sul, *Analysis of Wireless Power Transfer by Coupled Mode Theory (CMT) and Practical Considerations to Increase Power Transfer Efficiency*. IntechOpen, 2012.

[69] S. Qi and C. Sarris, "Deep Neural Networks for Rapid Simulation of Planar Microwave Circuits Based on their Layouts," *IEEE Trans. Microw. Theory Techn.*, vol. 70, no. 11, pp. 4805–4815, Nov. 2022.

[70] S. Wei, Q. Qu, X. Zeng, J. Liang, J. Shi, and X. Zhang, "Self-Attention Bi-LSTM Networks for Radar Signal Modulation Recognition," *IEEE Trans. Microwave*

Theory Techn., vol. 69, no. 11, pp. 5160–5172, Nov. 2021.

[71] M. Moradi A., S. A. Sadrossadat, and V. Derhami, “Long Short-Term Memory Neural Networks for Modeling Nonlinear Electronic Components,” *IEEE Trans. Compon., Packag. Manufact. Technol.*, vol. 11, no. 5, pp. 840–847, May 2021.

[72] H. A. Haus, *Waves and Fields in Optoelectronics*. Prentice-Hall, 1984.